

---

# The role of the physical microenvironment in cell migration and cytoskeletal force generation

Johannes Flommersfeld

---



Munich 2024



---

# The role of the physical microenvironment in cell migration and cytoskeletal force generation

Johannes Flommersfeld

---

Dissertation  
an der Fakultät für Physik  
der Ludwig-Maximilians-Universität  
München

vorgelegt von  
Johannes Flommersfeld  
aus Erlangen

München, den 20.03.2024

Erstgutachter: Prof. Dr. Chase Broedersz  
Zweitgutachter: Prof. Dr. Joachim Rädler  
Tag der mündlichen Prüfung: 03.06.2024

---

## Zusammenfassung

Zelluläre Krafterzeugung und Migration sind essentiell für Embryogenese, das Immunsystem, Wundheilung und Krebs. In all diesen Fällen interagieren Zellen mit einer komplexen Umgebung, welche ihr Verhalten beeinflusst. Um das Verhalten von Zellen im physiologischen Kontext zu verstehen ist es dementsprechend notwendig die physikalische Umgebung in experimentellen und theoretischen Ansätzen zu berücksichtigen. Obwohl die molekularen Komponenten der zellulären Krafterzeugung und Migration gut charakterisiert sind, fehlt nach wie vor ein theoretischer Ansatz der die Brücke zwischen molekularen Komponenten und emergenten zellulären Verhalten schlagen kann. Dies gilt insbesondere für Migration in komplexen, einengenden Umgebungen.

In früheren Arbeiten wurden effektive Modelle für Zellmigration auf zweidimensionalen Substraten sowie Kontinuumsmodelle für biologische Kontraktilität etabliert. In dieser Arbeit, verbinden wir solche effektiven Modelle mit den molekularen Eigenschaften der zugrundeliegenden Komponenten. Dafür analysieren wir biologische Krafterzeugung und Migration in experimentellen Systemen mit besonderem Fokus auf der Rolle der physikalischen Umgebung. In Kapitel 2 analysieren wir die dynamische Krafterzeugung von rekonstituierten Biopolymernetzwerken, welche aus Komponenten des zellulären Krafterzeugungsapparates bestehen. Hierbei untersuchen wir, wie solche Netzwerke elastische Strukturen mit unterschiedlichen mechanischen Eigenschaften verformen, um den Zusammenhang zwischen Kontraktionsverhalten und den Eigenschaften des Substrates zu verstehen. Darauf aufbauend entwickeln wir in Kapitel 3 ein allgemeines Modell für Zellmigration auf strukturierten und beschränkenden zweidimensionalen Oberflächen, welches wir systematisch vereinfachen um es mit früher entwickelten, effektiven Modellen für die Migration auf solchen Substraten zu verknüpfen. Dadurch erhalten wir ein tieferes Verständnis für die dem beobachteten Migrationsverhalten zugrundeliegenden Mechanismen. Zuletzt wenden wir dieses Vorgehen in Kapitel 4 auf Migration in dreidimensionalen Umgebungen an. Hierbei spielt die komplexe Interaktion zwischen den Verformungen des Zellkerns und dem zellulären Migrationsapparat eine entscheidende Rolle für das emergente Migrationsverhalten.

Zusammenfassend verdeutlicht unsere Arbeit das Potential der Kombination von mikroskopischen und effektiven, makroskopischen Beschreibungen für die Untersuchung emergenten Verhaltens komplexer biologischer Systeme.



---

## Summary

Cellular force generation and motility are key to embryonic development, the immune system, wound healing, and cancer. In all these examples, cells migrate and generate forces within a complex mechanical microenvironment, with which they interact and which shapes their behavior. Thus, in order to understand cellular behavior in physiological conditions, it is key to incorporate the physical environment into experimental studies and theoretical models. While the molecular components driving cellular force generation and migration are well characterized, a theoretical approach that is able to bridge the gap between molecular components and the emergent cellular behavior is still lacking. This applies in particular to migration in complex, confining physical environments.

Previous work established effective models for migration of cells on two-dimensional (confining) substrates as well as continuum models for biological contractility. In this thesis, we take a step towards connecting these effective models to the molecular properties of the underlying components. For this, we study biological force generation and cell migration in experimental systems which emphasize the role of the physical environment. In Chapter 2, we analyze the dynamic force generation of reconstituted biopolymer networks that consist of molecular components of the cellular force generation machinery. Here, we study how such networks deform compliant structures with different mechanical properties to understand the interplay between contraction behavior and the properties of the deformed substrate. We then build up on our understanding of the molecular components of the cellular cytoskeleton in Chapter 3 by developing a general model for migration on structured and confining two-dimensional surfaces that we systematically coarse-grain to connect it to previously found effective models for the migration behavior on such substrates. This yields new insights into the mechanistic origin of the observed migration behavior and results in efficient theoretical description that can be easily generalized to new migration scenarios. Finally, we apply this approach to the case of migration in three-dimensional confinement in Chapter 4, where we find that complex interplay between nuclear deformations and the cellular migration machinery are key to understand the emergent migration behavior.

Overall, our work highlights the power of combining microscopic models with effective, coarse-grained models to understand the emergent behavior of complex biological systems.



---

## Contents

<b>Zusammenfassung</b>	<b>v</b>
<b>Summary</b>	<b>vii</b>
<b>List of publications</b>	<b>xi</b>
<b>1 Preface</b>	<b>1</b>
<b>2 Actomyosin force generation in compliant environments</b>	<b>5</b>
2.1 The biophysics of contractile actomyosin networks . . . . .	6
2.2 Experimental studies of reconstituted actomyosin networks . .	16
2.3 Contraction dynamics and force generation of anchored actomyosin networks . . . . .	17
2.4 A minimal model for anchored actomyosin contractility . . . .	22
2.5 Discussion and outlook . . . . .	28
<b>3 The cytoskeleton in confined and directed cell migration</b>	<b>31</b>
3.1 Phenomenological and data-driven models for cell migration on structured surfaces . . . . .	32
3.2 The biophysics of cell migration: The four step process . . . . .	36
3.3 A general, bottom-up model for confined cell migration . . . . .	45
3.4 Migration and decision making in lateral confinement . . . . .	52
3.5 Biased migration on anisotropic substrates . . . . .	62
3.6 Discussion and Outlook: Towards shape and collective migration	71
3.7 Appendix: Simulation details on compliant substrates . . . . .	76
<b>4 The nucleus in 3D confined cell migration</b>	<b>77</b>
4.1 The complex role of the nucleus in confinement: From physical barrier to adaptive ruler . . . . .	79
4.2 Inferring a data-driven model for cell migration in physical confinement . . . . .	81
4.3 Cellular force generation and the nucleus: Is it pulled or is it pushed? . . . . .	88
4.4 Constraining a predictive, mechanistic model for cell migration in 3D confinement . . . . .	96

4.5 Discussion and Outlook . . . . .	105
<b>5 Conclusion and outlook</b>	<b>107</b>
<b>Bibliography</b>	<b>109</b>
<b>Acknowledgements</b>	<b>125</b>

---

## List of publications

### Publications directly relevant for this thesis

1. Haiyang Jia, Johannes Flommersfeld, Michael Heymann<sup>+</sup>, Sven K. Vogel<sup>+</sup>, Henri G. Franquelim, David B. Brückner, Hiromune Eto, Chase P. Broedersz<sup>\*</sup>, Petra Schwille<sup>\*</sup> (2022). *3D Printed Protein-Based Robotic Structures Actuated by Molecular Motor Assemblies*. **Nature Materials** 21.6, 703–709. DOI: 10.1038/s41563-022-01258-6.
2. Johannes Flommersfeld, Stefan Stöberl, Omar Shah, Joachim O. Rädler, Chase P. Broedersz<sup>\*</sup> (2024). *Geometry-Sensitive Protrusion Growth Directs Confined Cell Migration*. **Physical Review Letters** 132.9, 098401. DOI: 10.1103/PhysRevLett.132.098401.
3. Stefan Stöberl<sup>+</sup>, Johannes Flommersfeld<sup>+</sup>, Maximilian M. Kreft, Martin Benoit, Chase P. Broedersz<sup>\*</sup>, Joachim O. Rädler<sup>\*</sup> (2024) *Nuclear deformation and dynamics of migrating cells in 3D confinement reveal adaptation of pulling and pushing forces*. In preparation.

### Other publications

4. David B Brückner, Matthew Schmitt, Alexandra Fink, Georg Ladurner, Johannes Flommersfeld, Nicolas Arlt, Edouard Hannezo, Joachim O. Rädler<sup>\*</sup>, Chase P. Broedersz<sup>\*</sup> (2022). *Geometry adaptation of protrusion and polarity dynamics in confined cell migration*. **Physical Review X** 12.3, 031041. DOI: 10.1103/PhysRevX.12.031041.



## Preface

The cellular cytoskeleton, a complex network of polymer filaments and regulatory proteins, is an integral part of all life forms as it gives cells their shape and mechanical stability (Fletcher *et al.*, 2010). Apart from being a passive support structure, the cytoskeleton is also involved in a number of important active processes, in particular in eukaryotic cells. A special focus lies here on its force generation abilities, which allows cells to exert forces onto its microenvironment. This is essential for a number of biological processes: Stem cells probe the mechanical properties of their environment through traction forces, which ultimately controls their lineage specification (Engler, Sen, *et al.*, 2006). In tissue, contraction forces allow for a communication between cells (Charas and Yap, 2018). Finally, expansion and contraction of the cell body allow for eukaryotic cell migration (Danuser *et al.*, 2013). In this context, cellular force generation is mainly driven by filamentous actin, which is part of the cytoskeletal network together with microtubuli and intermediate filaments (Wen *et al.*, 2011). Both contractile and expansive force generation relies on the consumption of chemical energy in the form of ATP: Contractile forces are generated by bipolar molecular motors, which convert chemical energy into movement along filaments and thus induce relative sliding motion between filaments when bound to two different actin polymers (M. Murrell *et al.*, 2015). Expansive forces are driven by actin polymerization, which also relies on a conversion of ATP to ADP (Mogilner, 2006). This energy consumption drives the cellular cytoskeleton out of equilibrium, which results in rich and sometimes counter-intuitive behavior that cannot be understood in terms of classical, equilibrium physics (Banerjee *et al.*, 2020). This makes the cellular cytoskeleton in general and the force generating actin cytoskeleton in particular a fascinating material to study.

Besides the interest in the actin cytoskeleton from a physical or material scientific perspective, it also is a key component in many, previously mentioned biological processes. Here, cell migration stands out due to its wide range of applications. Cell migration is essential for embryonic development, where cells need to actively migrate to the correct region in the embryo to allow for the formation of specialized organs and body parts (Franz *et al.*, 2002). Further, even in adult organisms, active cell migration is essential for wound healing (Falanga, 2005) and the immune system, where immune cells

need to migrate fast over large distances in the body to allow for an adequate immune response (Luster *et al.*, 2005). Cell migration can however also be deadly for an organism when cancer cells transition to a migratory phenotype and invade the surrounding tissue (Clark *et al.*, 2015). This leads to the formation of cancer metastasis, which is responsible for 90% of all cancer related deaths (Chaffer *et al.*, 2011). Thus understanding and predicting cellular migration behavior could be key to develop better treatment strategies. Here, it is especially important to acknowledge the complex environment through which cells migrate in the body that involves chemical and mechanical gradients in a complex network of narrow confinements through which cells have to navigate. In biology, traditionally a large focus was put on chemical cues that direct cell migration either in the form of chemoattractants or chemorepellents, which play a role in the immune system or cancer (Petri *et al.*, 2018; Roussos *et al.*, 2011). More recently however, also the role of the physical environment was acknowledged. In particular due to the coupling between the cytoskeleton and the environment, which gives rise to interesting, stiffness-dependent cellular force generation (Trichet *et al.*, 2012) and directed migration behavior on substrates of differential stiffness (DuChez *et al.*, 2019; C.-M. Lo *et al.*, 2000). Apart from the mechanical properties of the environment, also its geometry can have a strong impact on the observed migration behavior: Cells were found to have a tendency to move and accelerate in narrow confinements in 2D and 3D (Brückner, Fink, Schreiber, *et al.*, 2019; Pathak *et al.*, 2012) and directed confining geometries can give rise to directed migration (Caballero, Comelles, *et al.*, 2015). This is particularly relevant in the physiological context, where cells are usually strongly confined. In such 3D environments, an additional component comes into play: the cellular nucleus, which, by itself, is a complex active material with interesting mechanical properties. To successfully migrate through 3D tissue, cells need to translocate and deform the nucleus with their cytoskeleton (Friedl, Wolf, *et al.*, 2011). Nuclear deformations can strongly influence cellular behavior through changes in gene transcription (Hsia *et al.*, 2022), DNA damage (Irianto *et al.*, 2017; Raab, Gentili, *et al.*, 2016), or Calcium signaling (Lomakin *et al.*, 2020; Venturini *et al.*, 2020). This gives rise to an interesting feedback between the cellular environment, the cytoskeleton and the nucleus that ultimately determines cellular migration behavior.

Due to the active nature of cytoskeletal force generation and cell migration, equilibrium physical theories cannot be applied to analyze these processes. This raises the question how two approach such systems from a theoretical point of view. There, two distinct schools of thought developed over time (Brückner and Broedersz, 2023): One tries to model the biological system by building a model for the underlying molecular components and their interactions from the bottom-up to then simulate these models and study their behavior. The other approach is more agnostic and tries to capture the emergent behavior on a more mesoscopic or macroscopic scale through an effective description. Which approach is more suited often depends on the system of interest. If a lot is known about the underlying molecular components and their interactions, bottom-up models can be well suited and allow for a detailed understanding of the system (Danuser *et al.*, 2013). In contrast, if less is known about the underlying processes, more agnostic, top-down approaches can prove valuable. To constrain those, it is however often beneficial to have large amounts of experimental data, which can be used to systematically infer an effective physical

description (Brückner, Ronceray, *et al.*, 2020; Selmeczi, Li, *et al.*, 2008). This is in a sense analogous to the use of thermodynamics and statistical physics in equilibrium physics, where statistical physics can give valuable insights into complex systems, where the underlying physical laws are well understood, while thermodynamics proves useful to explore systems for which such an underlying physical theory is lacking, such as in the case of black holes (Carlip, 2014). In the context of biological physics, both approaches face additional difficulties (Brückner and Broedersz, 2023): The underlying molecular processes are often times so complex that deciding on the right level of complexity and what aspects of the system to include into the theoretical description can present a major challenge and models quickly become so complex that they are hard to constrain from experimental data. Data-driven approaches on the other hand are bound to the experimental system for which they were constrained and cannot be easily generalized to other scenarios due to the lack of understanding of the underlying mechanisms (Brückner, Fink, Schreiber, *et al.*, 2019). This is in particular a problem in the context of a reductionist approach often taken by physicists: By decomposing a complex system into simpler subsystems, one tries to first understand the behavior of these subsystems before combining them again to explain the emergent behavior of the total system. If the physical description of a process is however only inferred for a specific subsystem, it is not straightforward to systematically increase the complexity of the system again without having to constrain a completely new model again. A promising avenue to overcome these limitations might however be to combine these two approaches in a way that data-driven models allow for a characterization the emergent behavior of the system and can act as a well-defined targets for simplifying and coarse-graining bottom-up models without relying on uncontrolled approximations and assumptions. Exploring the potential of this combined approach will be one of the main themes of this thesis.

We approach to combine bottom-up and top-down approaches in this thesis by starting out in Chapter 2 with a relatively simple and well understood experimental system: reconstituted actomyosin networks. There we study contractile actomyosin gels that are coupled to a mechanical environment to explore the mechanosensitivity of actomyosin force generation. Interestingly, even though some sensitivity of the contraction dynamics on the substrate stiffness can be observed, the observed mechanosensitivity is clearly distinct from the mechanosensitive force generation of cells, which involve additional components such as focal adhesions (C.-M. Lo *et al.*, 2000). Then we build up on our mechanistic understanding of the actin cytoskeleton that we developed in Chapter 2 to derive a general mechanistic model for cell migration on structured 2D surfaces in Chapter 3. We show that this model can be connected to previously constrained data-driven models from which we obtain valuable insights into the molecular processes underlying the emergent migration behavior. Beyond that we demonstrate that our model can easily be generalized to different experimental systems, that it can be used to characterize differences between cell lines, and that it can quantitatively predict the effect of changes in the experimental conditions, such as the surface coating. Finally, in Chapter 4 we apply this combined approach to a new experimental system, where neither bottom-up nor top-down models have been developed so far: mesenchymal migration through narrow 3D confinement. There, we infer an effective description of the cellular migration behavior, which shows features that are clearly distinct

to migration on 2D confining surfaces. In particular, through analysis of the nuclear deformations, we find that cells transition from a pushing dominated to a pulling dominated migration mode as confinement increases. We propose a mechanistic model that can explain these differences between 2D and 3D migration by accounting for the effect of physical confinement and in particular nuclear deformations on the cytoskeletal force generation.

## Actomyosin force generation in compliant environments

Actin-myosin networks play a crucial role in eukaryotic cell migration and cellular force generation (Bausch *et al.*, 2006; Kasza *et al.*, 2007). Within cells, actomyosin interacts with a number of other cellular components, including the nucleus, the cell membrane, polarity cues, focal adhesions, and other polymeric networks that are part of the cellular cytoskeleton (Fletcher *et al.*, 2010; Iden *et al.*, 2008). As such, it is often difficult to contribute cellular behavior to the biophysical properties of specific cellular components, such as the actomyosin system, making it challenging to obtain a mechanistic understanding of the cellular force production and migration machinery from observing the emergent cellular behavior. To address this, a reductionist approach is commonly adopted by studying individual cellular components in isolation to learn about their biophysical properties (Bausch *et al.*, 2006). From this, one then tries to gradually build-up towards cellular complexity by combining different components and studying their interactions in order to arrive at a mechanistic understanding of the emergent cellular behavior.

Following this approach, a number of experimental assays were developed to study the contraction behavior of isolated and reconstituted actomyosin networks with varying levels of complexity (see Section 2.2). These assays commonly ignore however a key aspect of actomyosin-driven force generation in the context of cell migration: the coupling to a compliant environment. This is particularly important, since it is well documented that the mechanical properties of the substrate crucially affect cellular force generation (Engler, Carag-Krieger, *et al.*, 2008; Ghibaudo *et al.*, 2008; Tan *et al.*, 2003; Trichet *et al.*, 2012), spreading and migration behavior (Han *et al.*, 2012; C.-M. Lo *et al.*, 2000), and even stem cell differentiation (Engler, Sen, *et al.*, 2006). In particular, cells were found to generate stiffness-dependent traction forces with higher forces being generated on stiffer substrates, which resulted in robust, stiffness-independent substrate deformations (Trichet *et al.*, 2012). Based on this observation it was proposed that the mechanosensitive force generation could give rise to the previously observed tendency of cells to migrate towards stiffer substrates (C.-M. Lo *et al.*, 2000).

Different models were proposed to explain this stiffness-dependent force generation. While some of these models rely on complex feedback mechanisms

between adhesion formation and substrate stiffness (Elosegui-Artola, Trepap, *et al.*, 2018; Trichet *et al.*, 2012), others simply describe cellular force generation in terms of a contractile, visco-elastic unit (Marcq *et al.*, 2011). This raises the question to what extent this remarkable feature of mechanosensitive force generation is an emergent property of the cellular force generation machinery or if it is simply an inherent property of contractile actomyosin networks.

We address this question in this chapter by analyzing the contraction behavior of reconstituted actomyosin networks that are coupled to soft, deformable structures with well-defined mechanical properties that can be used as force and velocity sensors. Interestingly, we find that the contractile force is stiffness-independent, while the contraction velocity strongly depends on the stiffness of the surrounding structure. From this data, we constrain an active fluid model for contractile actomyosin networks that are coupled to elastic substrates. We find that in order to explain both the observed contraction dynamics as well as the resulting steady state force, the catch-slip behavior of myosin motors is key. These results suggest that while actomyosin contractility displays some degree of intrinsic mechanosensitivity, the observed stiffness-dependent force generation in cells cannot be explained in terms of actomyosin contractility alone and likely requires the interaction with additional cellular components, such as mechanosensitive focal adhesions.

## 2.1 The biophysics of contractile actomyosin networks

We start by reviewing the biophysics of the individual components of actomyosin networks and discuss how the interactions between them give rise to a global contractile behavior of the network. Actin networks within cells contain a myriad of additional proteins that structure the network, such as crosslinkers or capping and branching proteins (Chugh and Paluch, 2018). In contrast, basic reconstituted contractile actomyosin networks only require two components: the biopolymer actin and the molecular motor myosin (Alvarado *et al.*, 2015; Thoresen *et al.*, 2011). Apart from those two components, other proteins such as actin crosslinker can be added to stabilize the actin network and to closer resemble the networks found within cells.

### Actin filaments and the semi-flexible wormlike chain

Actin filaments are a key component of the cellular cytoskeleton and as such are crucial for cellular force generation and migration (Danuser *et al.*, 2013). Thus, their structure, dynamics, and mechanical properties are not only relevant for this chapter, but play a central role throughout the entirety of this thesis. Filamentous actin forms through polymerization of monomeric actin into a helix like structure (Dominguez *et al.*, 2011) (Fig. 2.1). Notably, actin monomers are asymmetric and within a filament all monomers are oriented in the same direction. The resulting directionality of actin filaments allows us to distinguish between the two ends of an actin filament, which are denoted as barbed (+) and pointed (−) ends. During filament growth, monomers are predominantly included at the barbed end, while disassembly of actin monomers happens predominantly at the pointed end (Neuhaus *et al.*, 1983). Apart from this, the directionality of actin plays a crucial role when it comes to the inter-

action with motor proteins as we will discuss later in the context of actomyosin contractility.

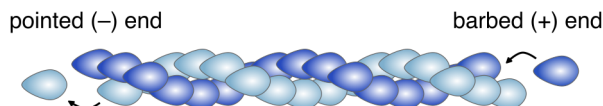


Figure 2.1: **Schematic illustration of the directed helix structure of actin filaments.** New monomers predominantly assemble at the barbed and disassemble at the pointed end.

The key to understanding the ubiquitous involvement of actin in biological force generation, ranging from cellular traction forces to muscle contractions, are the mechanical properties of actin filaments: Compared to other polymers, filamentous actin (F-actin) is of intermediate stiffness (Wen *et al.*, 2011). It is significantly stiffer than soft polymers such as DNA or synthetic polymers like polystyrene but still soft enough to be subject to thermal fluctuations on the length scale of a cell. This makes it softer than e.g. microtubuli, which are so stiff that they appear as straight filaments on cellular scales. The behavior of such *semiflexible* filaments subject to external forces can be understood in terms of the *Wormlike Chain* (WLC) Model, which we briefly summarize in the following.

In the WLC model, a polymer of contour length  $\ell$  is characterized by its bending energy  $\mathcal{H}_b$  (Broedersz and MacKintosh, 2014). In 2D, this bending energy can be simply written as

$$\mathcal{H}_b = \frac{\kappa}{2} \int_0^{\ell - \Delta\ell} dx \left( \frac{\partial^2 u}{\partial x^2} \right)^2, \quad (2.1)$$

where  $\kappa$  is the bending modulus of the filament,  $\ell - \Delta\ell$  is the projected length of the polymer, and  $u(x)$  denotes the deviation from a perfectly straight polymer ( $x$  denotes the position along a straight polymer of length  $\ell$ ). Note that the expression in Eq. (2.1) depends on the assumption that there are no overhangs in the contour of the filament and thus that the deviations from a perfectly straight polymer are relatively small. This assumption restricts the application of Eq. (2.1) to the case of stiff and semiflexible polymers. To derive a force extension relation, we consider an axial force  $F$  that is applied at the end of the filament. In that case, the total Hamiltonian reads (Broedersz and MacKintosh, 2014)

$$\mathcal{H} = \mathcal{H}_b + F\Delta\ell \approx \int_0^\ell ds \left[ \frac{\kappa}{2} \left( \frac{\partial^2 u}{\partial x^2} \right)^2 + \frac{F}{2} \left( \frac{\partial u}{\partial x} \right)^2 \right]. \quad (2.2)$$

In Fourier space ( $u(x) = \sum_q u_q \sin(qx)$ ), Eq. (2.2) can then be written as

$$\mathcal{H} = \frac{\ell}{4} \sum_q (\kappa q^4 + Fq^2) u_q^2. \quad (2.3)$$

At thermal equilibrium, we get from the equipartition theorem that (Broedersz and MacKintosh, 2014)

$$\langle |u_q|^2 \rangle_f = \frac{2k_B T}{\ell(\kappa q^4 + Fq^2)} \quad (2.4)$$

and thus the average value of  $\Delta\ell$  in the presence of an axial force  $F$  is given by

$$\langle \Delta L \rangle_F = k_B T \sum_q \frac{1}{\kappa q^2 + F}, \quad (2.5)$$

where the additional factor of 2 accounts for the fact that there are two identical, but independent transverse degrees of freedom in 3D. The average extension  $\delta\ell$  of a WLC subject to thermal fluctuations due to the application of an axial force  $F$  is then to leading order given by (Broedersz and MacKintosh, 2014)

$$\delta\ell = \langle \Delta\ell \rangle_0 - \langle \Delta\ell \rangle_F \approx \frac{k_B T \ell^4}{90\kappa^2} F. \quad (2.6)$$

We thus find to leading order a linear relation between the applied force  $F$  and the extension of the polymer  $\delta\ell$ . Solving Eq. (2.6) for the force  $F$  then gives us an expression for the effective spring constant  $k$  of a semiflexible polymer as  $k = 90\kappa^2/(k_B T \ell^4)$ .

However, if the axial force  $F$  is large enough, higher-order terms in Eq. (2.5) will contribute, leading to a non-linear force-extension relation. This is particularly relevant in the case of compression due the buckling instability of compressed rods (Landau *et al.*, 1986a). This instability arises from the structure of the Hamiltonian (Eq. (2.3)): For positive values of  $F$  (extensile forces),  $\kappa q^4 + Fq^2$  is strictly positive, such that  $\mathcal{H}$  is always minimized by a perfectly straight polymer ( $u_q = 0$  for all  $q$ ). Under compressive loads however,  $\kappa q^4 + Fq^2$  can take negative values, resulting in an instability with respect to transverse deflections (buckling). This is the case if the compressive force exceeds the threshold  $-F > \kappa q^2$ . Together with the smallest possible value of  $q = \pi/\ell$ , this gives us the buckling force (Broedersz and MacKintosh, 2014)

$$F_b = \kappa \left( \frac{\pi}{\ell} \right)^2. \quad (2.7)$$

Actin filaments that are exposed to compressive loads beyond this critical force, will buckle and to good approximation not withstand any further compression ( $k \approx 0$  for  $F > F_b$ ).

So far we have only considered the response to static external forces. However, to understand the physical properties of bulk actin networks, it is key to also consider the dynamic properties of single actin filaments. For that we consider the dynamics of  $u(x, t)$  that are given by the Langevin equation (Broedersz and MacKintosh, 2014; Gittes *et al.*, 1998)

$$\zeta \frac{\partial u(x, t)}{\partial t} = -\frac{\delta \mathcal{H}}{\delta u} + \xi(t) = -\kappa \frac{\partial^4 u(x, t)}{\partial x^4} + \xi(t), \quad (2.8)$$

where  $\xi(t)$  denotes Brownian white noise. In the absence of external forces ( $F = 0$ ), Eqs. (2.8) and (2.4) give us

$$\langle u_q(t) \rangle = \sqrt{\frac{2k_B T}{\ell \kappa q^4}} e^{-\omega(q)t}, \quad (2.9)$$

with  $\omega(q) = \kappa q^4 / \zeta$  and  $t > 0$  and thus (Gittes *et al.*, 1998)

$$\langle u_q(t)u_q(0) \rangle = \frac{2k_B T}{\ell \kappa q^4} e^{-\omega(q)|t|}. \quad (2.10)$$

Physically, the expression in Eq. (2.9) implies that bending modes dissipate on a wavelength dependent timescale. As a consequence, when probed at high frequencies, the filament appears stiffer. Indeed, Eq. (2.10) can be used to derive an expression for the frequency dependent (complex) spring constant of a semiflexible polymer, which asymptotically approaches the value of  $k$  for static forces obtained from Eq. (2.6) at low frequencies (Gittes *et al.*, 1998; Granek, 1997).

### Viscoelastic properties of actin networks

At high enough concentrations in solution, actin filaments interact with each other to form connected networks either through entanglement or through the addition of specific, crosslinking proteins (Broedersz and MacKintosh, 2014). The cellular cortex, which is essential for the cellular mechanical stability and contractility consists of exactly such a disordered actin network that is located underneath the cell membrane in metazoan cells (Chugh and Paluch, 2018). To motivate our model for such actin networks, we briefly discuss how the mechanical properties of individual filaments result in the emergent bulk rheological properties of entangled and crosslinked actin networks.

For that, we start by considering the minimal case of an entangled actin network that is immersed in a liquid solvent forming an actin gel. In that case, there will be two contributions to the bulk rheological properties: the actin filaments and the solvent. This can be summarized in the mathematical expression for the emergent complex modulus of the gel (Gittes *et al.*, 1998)

$$G^*(\omega) = \frac{\rho l_e}{\alpha_\omega} - i\omega\eta, \quad (2.11)$$

where  $\rho$  denotes the average actin density in the gel,  $l_e$  is the average free filament length between two points of entanglement,  $\eta$  is the viscosity of the solvent,  $\omega$  is the frequency at which the gel is getting sheared, and  $\alpha_\omega^{-1}$  denotes the frequency dependent stiffness of an individual actin filament discussed above.

At low frequencies, the complex single filament spring constant approaches a real value (Eq. (2.6)). Thus, the only viscous contribution to the complex modulus is from the solvent (Gittes *et al.*, 1998). Depending on the degree of crosslinking, the contribution of the network to the complex modulus is then expected to be either that of an elastic solid or, below a critical connectivity threshold, vanish completely due to a lack of mechanical stability (Broedersz, Mao, *et al.*, 2011). At higher frequencies, the imaginary part of  $\alpha_\omega$  becomes relevant, resulting in a viscoelastic behavior of the network itself in addition to the viscous contribution of the solvent (Gittes *et al.*, 1998). Indeed, the predicted scaling of both the real and imaginary part of the complex modulus with frequency agree well with experimental data (Koenderink, Atakhorrami, *et al.*, 2006). Thus, overall actin gels display a complex, frequency-dependent viscoelastic behavior. On long timescales however, they will either resemble an elastic solid or a viscous fluid, depending on the degree of crosslinking (Koenderink, Atakhorrami, *et al.*, 2006). These emergent viscoelastic properties of

actin networks inspired a number of coarse-grained continuum models for the behavior of actin gels, ranging from elastic (Ronceray and Lenz, 2015) and viscoelastic solids (Kruse *et al.*, 2005) to viscous fluids (Joanny and Prost, 2009).

### Myosin motors and the parallel cluster model

Apart from the mechanical properties of actin filaments and networks, their interactions with members of the motor protein family of myosins make them a key component of the cellular cytoskeleton (Sellers, 2000). In particular myosin II plays an important role for cell migration and contractile force generation (Aguilar-Cuenca *et al.*, 2014). The collectively generated forces can range from single cell traction forces on the scale of Nanonewtons (Trichet *et al.*, 2012) up to skeletal muscle contractions on the scale of Kilonewtons. In the context of this chapter we focus exclusively on myosin II and use the general term myosin interchangeably with myosin II.

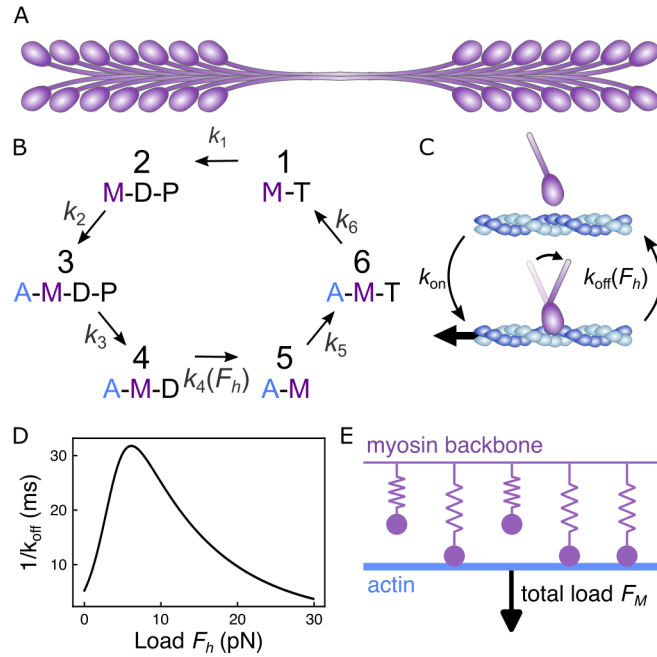


Figure 2.2: **Schematic illustration of myosin filaments and their interactions with actin.** **A.** Individual myosin proteins assemble into large, bipolar clusters to form myosin filaments. **B.** Myosin heads interact with actin filaments according to the six-step myosin cycle. A = actin, M = myosin, D = ADP, T = ATP and P = phosphate. **C.** This complex cycle can be simplified to two states (bound and unbound) with a constant on-rate  $k_{\text{on}}$  and a load-dependent off-rate  $k_{\text{off}}(F_h)$ , where  $F_h$  denotes the force per myosin head. **D.** Catch-slip behavior of the actin-myosin bond. The bond lifetime initially increases with load (catch) before it decreases at high loads (slip). **E.** Distribution of the total load over bound myosin heads in the parallel cluster model. All bound heads are assumed to share the total load  $F_M$  equally.

This astonishing ability arises from a combination of the structure of myosin filaments and the force-sensitive binding and unbinding kinetics of individual myosin heads. Individual myosin II proteins consist of a head domain which can bind to actin filaments and a tail domain that can bind to other myosin tails forming a characteristic bipolar filament structure (Fig. 2.2A) (Sellers, 2000). For skeletal muscle myosin II, these filaments can consist of hundreds of individual proteins, while non-muscle myosin II filaments typically consist of about 20 heads per side (Skubiszak *et al.*, 2002; Thoresen *et al.*, 2013; Tyska *et al.*, 1999). In the presence of ATP, the interaction between myosin heads and actin filaments follow a six-step cycle (Fig. 2.2B) (Howard, 2005a). This involves ATP-dependent binding, a conformational change upon ATP hydrolysis, as well as unbinding upon ADP release. The conformational change adapts the angle between the head and tail domain (Fig. 2.2C) resulting in a so-called *working stroke* that dislocates the backbone (tail regions) of the myosin cluster towards the barbed end of the actin filament (Howard, 2005a). If only one side of a bipolar myosin filament (Fig. 2.2A) interacts with an actin filament or if both sides interact with parallel actin filaments, the large number of heads contained in a myosin filament allows them to move processively towards the barbed ends of the actin filaments even though individual myosin molecules are not processive (Howard, 2005c). If the two sides of the myosin filament interact however with two anti-parallel actin filaments, the interaction between actin and myosin results in relative motion of the two actin filaments.

The velocity with which myosin moves along or displaces actin filaments and the rate of myosin detachment from actin depend on the load that is exerted onto the myosin filament (Debold *et al.*, 2005). This is due to the load dependent unbinding kinetics of individual myosin heads (Fig. 2.2B and C). In particular, myosin heads forms so-called catch-slip-bonds with actin (Guo *et al.*, 2006). This means that the bond lifetime initially increases with load before it decreases at higher loads. We model this by simplifying the complex myosin binding and unbinding cycle (Fig. 2.2B) to a simple binding and unbinding cycle (Fig. 2.2C) with a load-independent binding rate and a load-dependent unbinding rate (Fig. 2.2D). For the load-dependent unbinding rate, we use a phenomenological expression as a function of the load per head  $F_h$  (Guo *et al.*, 2006)

$$k_{\text{off}}^{\text{head}}(F_h) = k_{\text{off}}^{\text{catch}}(0)e^{-\frac{F_h x_{\text{catch}}}{k_B T}} + k_{\text{off}}^{\text{slip}}(0)e^{\frac{F_h x_{\text{slip}}}{k_B T}}, \quad (2.12)$$

where  $k_{\text{off}}^{\text{catch}}(0)$  and  $k_{\text{off}}^{\text{slip}}(0)$  weigh the contributions due to the catch and slip behavior of the actomyosin bond, and  $x_{\text{catch}}/k_B T$  and  $x_{\text{slip}}/k_B T$  are characteristic force scales for the catch and slip behavior, respectively. To understand how the load-sensitivity of individual heads determines the velocity and attachment time of myosin clusters, we consider a microscopic model of myosin filaments, the *parallel cluster model* (Erdmann and Schwarz, 2012).

**The parallel cluster model.** For that, myosin filaments are modeled as a cluster of parallel, elastic springs that can bind to actin filaments. These springs represent individual myosin heads and the total load experienced by the myosin filament is thus equally shared over all springs that are currently bound to an actin filament (Fig. 2.2E) (Erdmann, Albert, *et al.*, 2013). The lifetime of individual bonds is assumed to be independent of the state of neighboring heads. The dynamics of the number of bound heads is then equivalent to

a biased, one-dimensional random walk with forward rate  $k_{\text{on}}^{\text{head}}$  and a load-dependent backward rate  $k_{\text{off}}^{\text{head}}(F_h)$ . A motor filament unbinds in this model when the number of bound heads is zero. This allows us to derive the average unbinding time of a motor filament with initially  $m$  bound heads as the mean first passage time  $\tau_{m,0}$  of a random walker starting at site  $m$  to reach site 0. The average unbinding time of a motor with  $m$  bound heads is thus given by (Erdmann, Albert, *et al.*, 2013)

$$\tau_{m,0}(F_M) = \sum_{n=1}^m \sum_{i=n}^{N_h} \frac{1}{i k_{\text{off}}^{\text{head}}(F_M/i)} \prod_{j=n}^{i-1} \frac{(N_h - j) k_{\text{on}}^{\text{head}}}{j k_{\text{off}}^{\text{head}}(F_M/j)}. \quad (2.13)$$

Here,  $F_M$  denotes the load that a myosin filament experiences in total and  $N_h$  denotes the total number of heads per myosin filament that interact with an actin filament.

Since we assume that every motor filament experiences the same average load, we can average over all initial conditions to obtain the average unbinding time at every point in time. To do so, we use the steady-state probability distribution  $p_i^s(F_M)$ , which denotes the probability for a myosin filament under load  $F_M$  to be bound with  $i$  heads to an actin filament. Since the myosin heads are stiff compared to the rest of the system (motor elasticity of about  $2.5 \cdot 10^3$  pN/ $\mu\text{m}$  (Koenderink, Dogic, *et al.*, 2009) compared to the effective actin spring constant of about 0.2 pN/ $\mu\text{m}$  (Mogilner and Oster, 1996)), this steady state should be reached fast compared to the other timescales in the system and this approximation should be justified for our purposes. This steady-state probability distribution is given by (Erdmann, Albert, *et al.*, 2013)

$$p_i^s(F_M) = \frac{\prod_{n=0}^{i-1} \frac{(N_h - n) k_{\text{on}}^{\text{head}}}{(n+1) k_{\text{off}}^{\text{head}}(F_M/(n+1))}}{1 + \sum_{k=1}^{N_h} \prod_{j=0}^{k-1} \frac{(N_h - j) k_{\text{on}}^{\text{head}}}{(j+1) k_{\text{off}}^{\text{head}}(F_M/(j+1))}}. \quad (2.14)$$

We can use Eqs. (2.13) and (2.14) to calculate the load-dependent myosin filament unbinding rate as

$$k_{\text{off}}(F_M) = \left( \sum_{m=1}^{N_h} p_m^s(F_M) \tau_{m,0}(F_M) \right)^{-1}. \quad (2.15)$$

From Eqs. (2.13) to (2.15) it becomes apparent that longer lifetimes of the individual heads under load also translates to longer lifetimes of the motor filament as a whole, such that myosin filaments also effectively behave as catch-slip-bonds.

### The origin of contractility in actomyosin networks

When myosin motors are added to actin networks, this results in a global contraction of the network (M. Murrell *et al.*, 2015). This is curious because of the disordered nature of actin networks. While within skeletal muscle, actin filaments are arranged in a highly ordered structure that only allows for contractile force generation (Craig *et al.*, 2004), there is no reason *a priori* why contraction should be favored over expansion in disordered actomyosin networks (M. Murrell *et al.*, 2015). However, the specific mechanical properties

of actin as a semi-flexible filament and the binding and unbinding dynamics of myosin give rise to a number of mechanisms that can break this symmetry and explain the observed dominance of contractility in actomyosin systems.

**Polarity Sorting.** The first mechanism we want to discuss is connected to the unbinding of myosin motors. Myosin II traverses actin filaments towards their barbed ends. Once it reaches the barbed end it might either fall off immediately or dwell at the barbed end for an extended period of time. If the motor dwells at the barbed end, this gives rise to a *polarity sorting* mechanism that leads to a self-organization of the network that favors contractile configurations (Lenz, 2014; Liverpool *et al.*, 2005; Surrey *et al.*, 2001): If a myosin motor binds to an actin filament it walks towards its barbed end. While walking along the filament it can bind to a second filament with its other head region. Once it reaches the end of one filament it remains there for some finite time (end dwelling). Note that the motor will still walk along the other filament. In that way, myosin motors cluster the barbed ends of actin filaments together. This eventually results in the formation of actin asters where the pointed ends are oriented away from the center of the cluster (Fig. 2.3). The asters themselves are not particularly contractile, since dwelling myosin does not apply an active force onto the actin filaments anymore. However, if two asters overlap and a myosin motor binds filaments associated with both asters, this results in a contractile configuration, which can drive global network contractions.

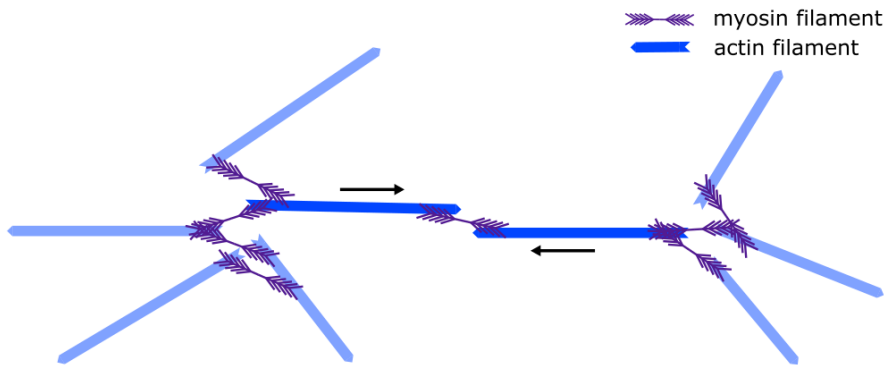


Figure 2.3: **Polarity sorting due to myosin dwelling at the barbed end.** If myosin motors stay bound at the barbed end of an actin filament, this leads to the formation of polarity sorted actin asters. Overlapping asters result in a contractile configuration.

It was long unclear if myosin actually dwells near actin barbed ends and if such a polarity sorting mechanism actually plays a role in actomyosin contractility (Lenz, 2014). In particular in the context of highly crosslinked networks such as the cellular cortex, it is also unclear if the described aster formation can actually take place due to the strong constraints imposed by the crosslinks. Nonetheless, recent work was able to experimentally confirm myosin end dwelling and subsequent aster formation in random actomyosin networks (Wollrab *et al.*, 2018), making this a relevant mechanism at least in the context for reconstituted actomyosin networks.

**Filament bundling.** A second mechanism that favors contraction over expansion occurs when a myosin motor links two intersecting filaments (Fig. 2.4). For a myosin motor to be able to crosslink the two filaments it has to bind near the intersection. Since myosin traverses towards the barbed end of the filaments, it is more likely to find myosin filaments on one side of the intersection than the other (Lenz, 2014). As a consequence, as the motor migrates further towards the barbed ends of the filaments, it applies a lateral contractile force onto the filament, which leads to an increased alignment and bundling of the filaments as the motor moves further away from the intersection. Other effects such as the elastic properties of the myosin motor further contribute to an overall contractile dipole. Such myosin induced bundling is indeed also observed experimentally in regions of high contractility in migrating cells (Svitkina *et al.*, 1997).

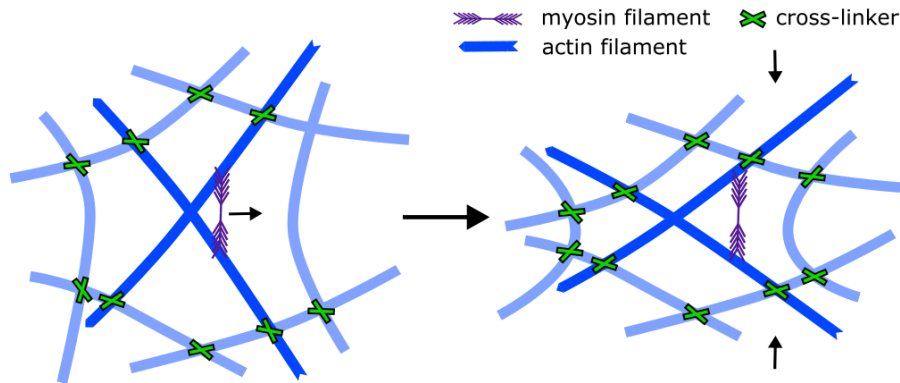


Figure 2.4: **Lateral contraction due to myosin induced filament bundling.** As myosin motors traverse along two overlapping filaments towards the barbed ends, they generate a lateral force that results in a lateral contraction of the network and the formation of actin bundles.

**Filament plucking.** So far, we have focused on geometric arguments and the myosin binding and traversing behavior. Those arguments are however quite general and not specific to actin networks. It is however likely that the dominance of contractility that is specific to actin networks arises at least partially from the mechanical properties of actin filaments. In particular its bending stiffness, which is low enough such that myosin motors are able to significantly bend actin filaments. One scenario in which this plays a role arises when a myosin motor connects two actin filaments that are approximately orthogonal to each other, such that the motor *plucks* one of the filaments (Lenz, 2014; Ronceray, Broedersz, *et al.*, 2019) (Fig. 2.5). In that case, as the myosin motor traverses towards the barbed end of the actin filaments, it will induce a strong bending of one of the actin filaments, resulting in an additional contractile contribution along the direction of that filament.

**Filament buckling.** The final mechanism that we want to discuss here is connected to the buckling instability under compressive loads discussed above:

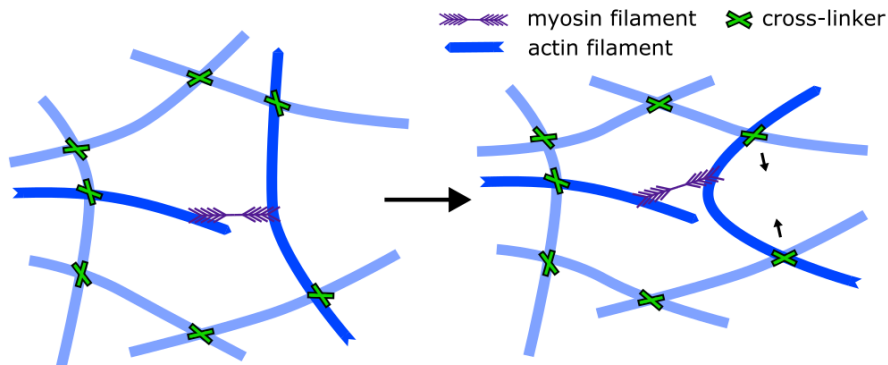


Figure 2.5: **Filament plucking favors contractility.** Since actin is a semiflexible filament, myosin motors can bend the filaments. On average, this leads to an overall contractile dipole.

Semiflexible filaments buckle under compressive loads that exceed a certain threshold (Broedersz and MacKintosh, 2014). This renders them incapable of transmitting compressive forces through the network that exceed this buckling threshold.

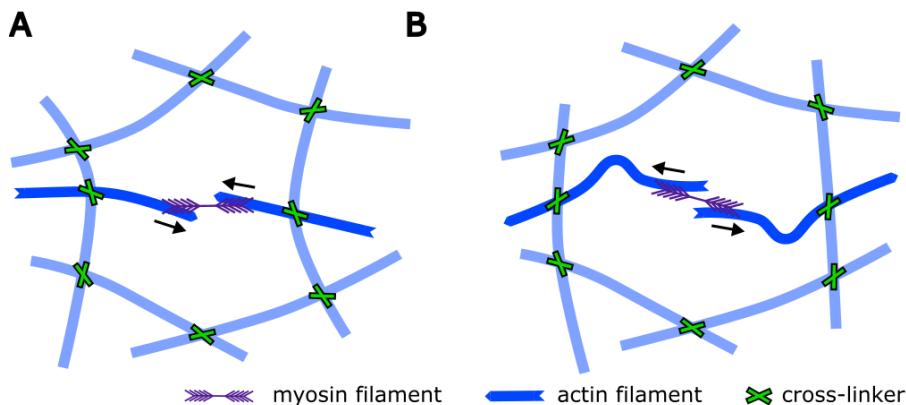


Figure 2.6: **Filament buckling suppresses extensile forces.** **A.** Large contractile stresses can propagate through the network over long length scales. **B.** In contrast the propagation of large extensile stresses is suppressed due to filament buckling. This leads to an overall dominance of contractile stresses.

Thus, local contractile force dipoles induced by myosin filaments (Fig. 2.6A) are expected to result in a global contraction of the network (Ronceray, Broedersz, *et al.*, 2016). Strikingly, also local extensile force dipoles (Fig. 2.6A) are predicted to lead to a global contraction due to the force asymmetric transmission in the network. This mechanism is supported by direct experimental observations of actin buckling *in vitro* (M. P. Murrell *et al.*, 2012). Note however that also this mechanism has limitations in heavily crosslinked networks. If the network is strongly crosslinked, the buckling threshold increases due to

the short free filament lengths and the forces generated by the myosin motors might not be large enough to buckle actin filaments.

## 2.2 Experimental studies of reconstituted actomyosin networks

To give some context to our work, we review a number of existing experimental assays used to study actomyosin contractility *in vitro* together with the key insights obtained with these assays. The simplest reconstituted system that emulates the contraction behavior of the cellular cortex, simply consists of actin filaments and myosin motors (see e.g. Schuppler *et al.*, 2016). As discussed in the previous section, in the presence of ATP, myosin motors induce a global, isotropic contraction. Interestingly, when myosin motors are only activated locally, the contraction behavior depends on the geometry of the contractile region (Schuppler *et al.*, 2016): Isotropic activation patterns, such as circles, result in isotropic contraction behavior, preserving the original shape of the pattern. Anisotropic geometries, such as squares, however, lead to non-affine deformations due to the force balance within the network. Also, the connectivity of the actin network needs to be high enough to allow for global, isotropic contractions. This can be controlled through the average actin filament length through the addition of capping protein (Schuppler *et al.*, 2016) or through actin crosslinking (Ennomani *et al.*, 2016). At low connectivities, the network fragments and self organizes into dense actin bundles without significant deformations of the outer boundaries of the contractile pattern. At high connectivities, the network is too stiff to contract, with a contractility optimum at intermediate connectivities. These observations yield important insights for the design of contractile actomyosin networks in elastic frames that we will discuss in the next section.

Instead of forming networks out of individual actin filaments, it is also possible to assemble actin bundles into a two-dimensional network through the use of bundling proteins such as Fascin (Ideses *et al.*, 2018). Despite the increased stiffness of bundles compared to individual actin filaments, these networks still display an isotropic contraction behavior in two dimensions. Interestingly, the myosin induced contractility results in three-dimensional folding of the actin sheet. The contraction dynamics of these networks display an interesting acceleration behavior, which the authors connect to myosin catch-bond behavior. This interpretation is supported by the fact that a similar acceleration behavior can be observed in contractile microtubuli networks when the contractions are driven by the molecular motor dynein, which also displays catch-bond behavior (Foster, Fürthauer, *et al.*, 2015).

Another common experimental assay assembles the actin network close to a lipid bilayer, mimicking the biological configuration within cells, where the actin cortex is attached to the cell membrane (Linsmeier *et al.*, 2016; M. P. Murrell *et al.*, 2012; Vogel *et al.*, 2013). A careful analysis of the change of filament length during network contraction by M. P. Murrell *et al.*, 2012 revealed a striking correlation between filament strain and network strain during contraction for a range of different crosslinker concentrations. This suggests buckling to play a key role during network contraction in these experiments. Another study finds that myosin activity can even result in actin filament fragmentation

in such systems (Vogel *et al.*, 2013). This could have important implications for the connectivity and the mechanical properties of the actin network at different stages of the contraction. A detailed analysis of dependence of the contraction dynamics on the number and density of myosin motors, revealed that actomyosin contraction is highly *cooperative* and *telescopic* (Linsmeier *et al.*, 2016), meaning that strain rates increase with increasing myosin density and contraction velocity increases with the total number of active myosin motors at constant density. These experiments yield important insights into the underlying mechanisms of actomyosin contractility and how the network’s contraction behavior is shaped by the underlying molecular components.

So far, we have discussed the coupling of actomyosin networks to membranes simply as a tool to assemble effectively two-dimensional networks. In cells, the actin cortex can however actively deform the membrane. This can be mimicked by coupling contractile actomyosin to a deformable membrane by assembling an actomyosin gel inside of a lipid vesicles (Nishigami *et al.*, 2016). This results in repeated, non-periodic deformations of the vesicle due to actomyosin contractility together with an asterlike self-organization of the actin network. Unfortunately, this study does however not evaluate the mechanical properties of the membrane, such that it is not possible to relate the observed deformations to myosin generated forces. This makes a more quantitative analysis of these results difficult. Another approach to couple contractile actomyosin networks to a mechanical environment was established by Roos *et al.*, 2003. There, actin filaments were assembled into a regular network on top of microfabricated pillars. These pillars are however too stiff for the myosin motors to induce observable deformations. This makes it impossible to systematically study the interaction between a contractile actomyosin network and a compliant environment in this assay. An alternative approach that allows for a measurement of the force generation of actomyosin structures is based on linking actin to beads, which are in turn connected to an elastic substrate (Thoresen *et al.*, 2011). The deformations of the substrate can be used to compute the force velocity relation of actomyosin bundles, which connect two beads. While this is an elegant approach to measure actomyosin force generation in bundles, it yields limited information about the contraction behavior of disordered networks as found within cells.

Overall, previous studies with tethered and untethered contractile actomyosin structures have greatly advanced the understanding of the mechanisms underlying contractility of disordered actomyosin networks. Despite this, an approach that allows for a quantitative analysis of the effect of a compliant mechanical environment on the contraction behavior of actomyosin gels is still lacking. In this context it is particularly interesting to study how the contraction behavior depends on substrate stiffness and how this compares to the mechanosensitive force generation observed in cells.

### 2.3 Contraction dynamics and force generation of anchored actomyosin networks

To address this, we introduce an experimental approach that generalizes micropillar-based traction force microscopy assays to the case of reconstituted actomyosin networks (see Jia *et al.*, 2022 for experimental details). To do this, actomyosin

gels are mechanically connected to soft pillars of tunable stiffness (Fig. 2.7). The pillars are manufactured through a two-photon 3D-printing technique, where bovine serum albumin (BSA) in solution is locally photopolymerized. This results in soft hydrogel structures of well-defined geometries.

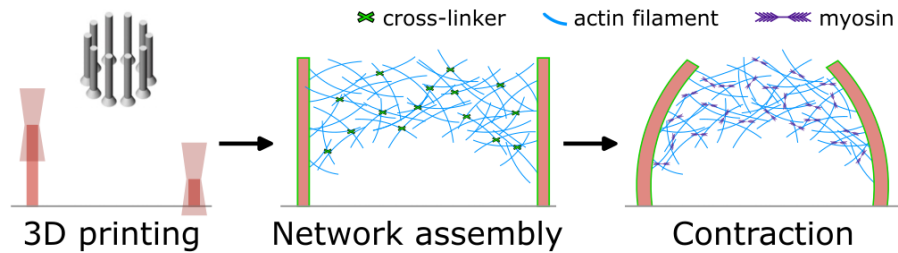


Figure 2.7: **Sketch of the experimental setup** (adapted from Jia *et al.*, 2022). A ring of compliant, biotinylated hydrogel pillars is printed through photopolymerization, to which a crosslinked actin network can bind. Upon myosin addition, the network contracts and deflects the pillars.

Here, we will discuss structures that consist of individual hydrogel pillars that are arranged in a circular geometry (Fig. 2.7, left). The mechanical properties of these hydrogel structures and in particular their Young's modulus depends on the degree of photo-induced polymerization, allowing for a tight control over the stiffness of the printed structures through the printing parameters, such as laser power and scan speed (Jia *et al.*, 2022). Note that this allows us to tune pillar stiffness without varying the pillar dimensions, which could result in unwanted side-effects due to the changed surface area. To cover a broad range of stiffnesses, the Young's modulus was varied between 10 kPa and 250 kPa. To be able to mechanically link actin filaments to the 3D printed hydrogel structures, a fraction of the BSA in solution is biotinylated such that biotin is present at the surface of the structures. Then, biotinylated actin filaments are added to the solution. Note that while within cells actin is constantly turned over through polymerization and depolymerization (Blanchoin *et al.*, 2014), here, actin filaments are stabilized. For actin filaments to be able to bind to the biotinylated BSA structures as well as being crosslinked to a connected network, an additional protein is necessary that can bind to biotin, serving as a linker between different actin filaments as well as between actin and BSA. For this, neutravidin is used. For simplicity, we just refer to biotin-neutravidin-biotin complexes as crosslinkers in the following. The addition of actin and the crosslinker, results in the formation of an actin network that is stably connected to the ring of hydrogel pillars (Fig. 2.7, middle). Fluorescent microscopy confirms that the resulting actin network spans the entire distance between pillars and is not only found between neighbouring pillars (Fig. 2.8A and B). Interestingly, these images also reveal that the network attaches mostly near the top of the pillars (Fig. 2.8A and B), which has important implications for the analysis of the contraction induced pillar deflections. To trigger contractility, myosin is added to the solution (Fig. 2.7, right), which results in a global contraction of the network. This can be quantified through the deflection of the surrounding pillars, which happens within minutes after the addition of myosin

(Fig. 2.8C and D). As we will discuss in more detail in the following sections, tracking the deformation of the fluorescently labeled micropillars allows us to quantify the myosin-induced contraction dynamics.

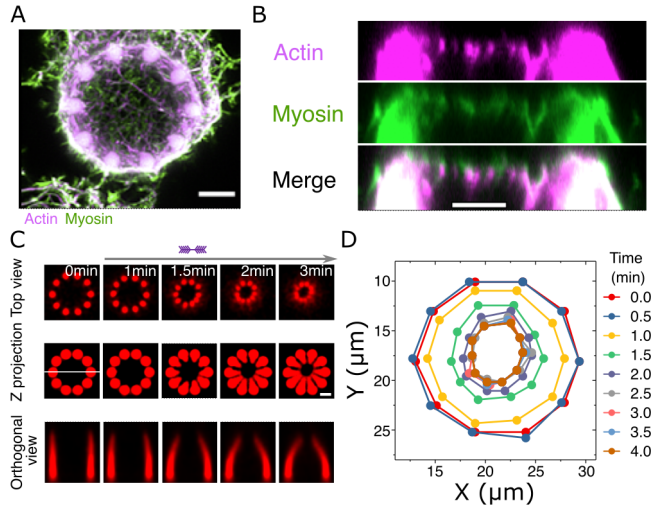


Figure 2.8: **Experimental confirmation of the setup** (adapted from Jia *et al.*, 2022). **A.** The z-projection of the actomyosin exoskeleton on a pillar ring shows a spanning network over the entire area of the ring. **B.** The side view of the pillar rings reveals that the spanning network is attached near the tip of the pillars. **C.** Contraction dynamics of the pillar ring in response to motor activation. Only the BSA hydrogel is imaged, actomyosin network not visible. The white line in the top left image indicates the position for generating orthogonal view. **D.** Dynamics of the pillar tips during the contraction. The global contraction of the actomyosin network results in an isotropic deflection of the pillars. Scale bars: 5  $\mu\text{m}$ .

### Quantification of the pillar deflections

Tracking the position of the tips of the pillars, we observe a distinct deformation behavior (Fig. 2.9A). Initially, deformation is slow before the contraction accelerates, reaching a maximum after around one minute. Then the tips approach their final, contracted position and the contraction slows down. Interestingly, the acceleration lasts much longer than the dynamics of single or spatiotemporally coordinated myosin motors in sarcomeres, which operate on the timescale of milliseconds (Caruel *et al.*, 2018). This acceleration behavior can be observed at all considered pillar stiffnesses. Note that this analysis reveals a first mechanosensitive property of actomyosin contraction behavior: The peak velocity observed during the contraction displayed a strong stiffness dependence, with soft pillar rings being contracted at much faster rates than stiff pillar rings (Fig. 2.9B).

Apart from the contraction dynamics, we are particularly interested in the force that is generated in the final contracted state, since this can be easily compared to the stiffness-dependent traction forces generated in cells (Trichet

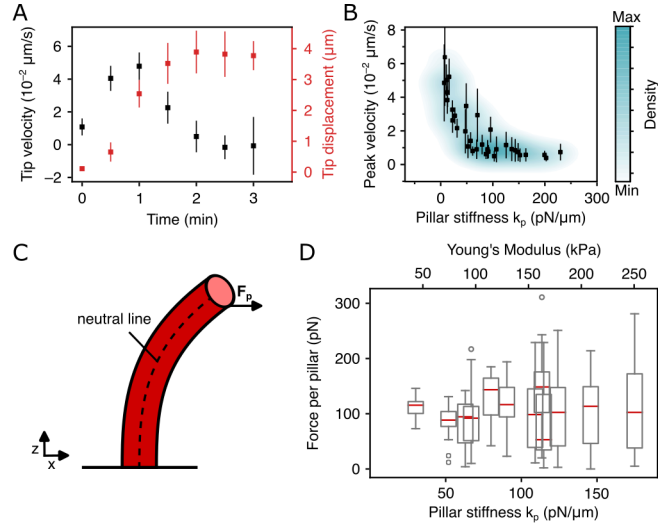


Figure 2.9: **Quantification of the contraction behavior at different pillar stiffnesses** (adapted from Jia *et al.*, 2022). **A.** The contraction dynamics of an exemplary pillar ring with an effective spring constant of  $k_p = 35$  pN/ $\mu$ m. Shown are the average displacement and velocity of the pillar tips over time. **B.** The peak contraction velocity at different pillar stiffnesses. The error bars in A and B indicate one standard deviation. **C.** Sketch of a deflected pillar that is subject to a point force at the tip. **D.** Active force per pillar exerted on pillar rings with different stiffnesses. The final contraction force displays a striking robustness over a broad range of pillar stiffnesses.

*et al.*, 2012). For that we need an expression for the bending profile of the pillars. In particular, we are interested in the shape of the neutral line of the deflected pillar (Fig. 2.9C). To derive an analytic expression for the expected pillar profile, we assume that (i) the pillar consists of a linear elastic material, characterized by its Young's modulus  $E$ , and (ii) the largest contribution to the torque on the pillar stems from forces acting on its tip. The second assumption is justified by observation that the spanning network is predominantly attached at the top of the pillar (Fig. 2.8B). We thus approximate the force applied by the actomyosin gel on the pillar by a point force  $F$  at the tip of the pillar. Since the pillar length (15  $\mu$ m) is much larger than the pillar width (2  $\mu$ m), we assume the pillar to be thin compared to its length and the deflection to be small enough such that we can neglect higher-order derivatives of the displacement (with respect to the height).

To find an expression for the deflected pillar profile, we consider the torque balance in the  $y$ -direction. The  $y$ -component torque induced by a point force in  $x$ -direction applied at the tip of the pillar (Fig. 2.9C) is given by (Landau *et al.*, 1986a)

$$M_y^{\text{Force}} = \int dA x \sigma_{zz} = \frac{E}{R} \frac{\pi}{4} r^4, \quad (2.16)$$

where  $E$  is the Young's modulus of the pillar material and  $R^{-1}$  denotes the local curvature of the pillar. Since the pillar is fixed at its base any torque

needs to be balanced in the final deflected state. The balancing torque due to the fixation at the base is given by (Johnston *et al.*, 2009)

$$\mathbf{M}^{\text{reaction}} = \mathbf{F} \times \mathbf{r} = F_p L \hat{\mathbf{e}}_y. \quad (2.17)$$

We can then calculate the internal torque at height  $z$  by virtually cutting the pillar at height  $z$ . Similar to Eq. (2.17), the  $y$ -component of the internal torque at this point is given by

$$M_y^{\text{reaction}}(z) = F_p(L - z). \quad (2.18)$$

Equating Eqs. (2.16) and (2.18) yields the equilibrium condition

$$\frac{E}{R} \frac{\pi}{4} r^4 = F_p(L - z). \quad (2.19)$$

To find the profile  $x(z)$  we express the curvature  $1/R$  in terms of  $x(z)$  and its derivatives as

$$\frac{1}{R} = \frac{x''(z)}{\sqrt{1 + x'(z)^2}}. \quad (2.20)$$

By combining Eqs. (2.19) and (2.20) we obtain a differential equation for the beam profile

$$\frac{x''(z)}{\sqrt{1 + x'(z)^2}} = \frac{F_p}{EI}(L - z). \quad (2.21)$$

Using the assumption, that the beam is weakly deflected, this simplifies to

$$x''(z) = \frac{F_p}{EI}(L - z). \quad (2.22)$$

With the corresponding boundary conditions  $x'(z = 0) = 0$  and  $x(z = 0) = 0$ , we get the beam profile (Landau *et al.*, 1986a)

$$x(z) = \frac{4F_p}{E\pi r^4} \left( \frac{L}{2} z^2 - \frac{z^3}{6} \right), \quad (2.23)$$

and the corresponding tip displacement

$$x(L) = \frac{4L^3}{3E\pi r^4} F_p, \quad (2.24)$$

which allows us to define an effective spring constant of the pillar

$$k_p = \frac{3E\pi r^4}{4L^3}. \quad (2.25)$$

Based on this analysis, we can extend the ideas of traction force microscopy to the case of reconstituted actomyosin gels by relating the observed pillar deflections to the total contraction force by fitting Eq. (2.23) to the experimentally observed shapes of the deflected pillars. Note that the only free parameter in Eq. (2.23) is the deflection force per pillar  $F_p$ . From this, we obtain an average forces per pillar of  $126 \pm 0.02$  pN, which is robust over a wide range of pillar stiffnesses (Fig. 2.9D). Individual myosin filaments under these conditions can generate forces close to 20 – 60 pN (Y.-S. Cheng *et al.*, 2020; Kalganov *et al.*, 2013; Vogel *et al.*, 2013), suggesting that only a small fraction of the myofilaments in the exoskeleton effectively contribute to the contraction (see Jia *et al.*, 2022 for a more detailed discussion).

## 2.4 A minimal model for anchored actomyosin contractility

To obtain a better understanding of how the motor-induced contractility of the network leads to the observed, stiffness-dependent acceleration effect during the contraction and stiffness-independent contraction forces, we derive a simple mechanical model for the mechanical properties of the actin network and the motor activity. We then gradually increase the complexity of this model until we are able to capture the observed experimental contraction behavior.

### Significance of the elastic response of the network

In general, actomyosin networks can be described as active viscoelastic gels (see Section 2.1) (Kruse *et al.*, 2005; Prost *et al.*, 2015), but the extent to which the elastic response of the network plays a role depends on the timescale on which the system is observed and experimental factors such as crosslinking. Since the actomyosin network is coupled to elastic frames in our experimental setup, the elastic response of the network will only significantly affect the contraction behavior if the effective spring constant of the network is similar in magnitude or larger than the stiffness of the pillars. To identify which aspects of the viscoelastic actomyosin gel need to be included in our theoretical description, we first consider the final contraction force as a function of the pillar stiffness (Fig. 2.9D). When analyzing the final contracted state, the viscous response of the network does not have to be accounted for. Hence, only the elastic response of the actomyosin gel contributes.

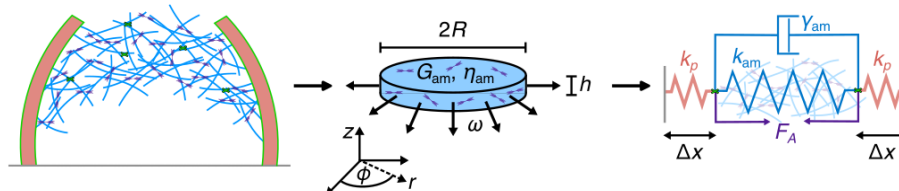


Figure 2.10: **Schematic illustration of the mechanical model** (taken from Jia *et al.*, 2022). The rheological properties of the network as well as its dimensions determines the effective network stiffness  $k_{am}$  and viscosity  $\gamma_{am}$ .

We characterize the elastic response of the network by an effective spring constant  $k_{am}$  (Fig. 2.10). Due to the symmetric configuration of our experimental setup, the system can be described by a 1D model with a spring, representing the elastic response of the actomyosin gel, which is attached to two springs of zero rest length, representing the pillars (Eq. (2.24)). Finally, the myosin activity induces an active stress in the system, which leads to a contractile active force  $F_A$  acting on each of the pillars. Thus, the gel's activity leads to a stretching of the two pillar springs by  $\Delta x$ . Note that, due to the symmetry of the system, this corresponds to a deformation of the actomyosin spring by  $2\Delta x$ . At mechanical equilibrium, this model yields the following force balance equation:

$$2k_p\Delta x = -2k_{am}\Delta x + 2F_A. \quad (2.26)$$

Solving this equation for  $\Delta x$  leads to

$$\Delta x = \frac{F_A}{k_p + k_{am}}. \quad (2.27)$$

which was found previously (Marcq *et al.*, 2011; Trichet *et al.*, 2012; Zemel *et al.*, 2010). Thus, if  $k_{am}$  is larger or of a similar order of magnitude as  $k_p$ , we would expect that the final contraction force  $F_p = k_p F_A / (k_p + k_{am})$  exerted on the pillars depends on the pillar stiffness  $k_p$  (Fig. 2.11A), as observed for living cells (Trichet *et al.*, 2012). Notably, we could not observe such a dependence in our experiments, but instead measured an approximately constant force (Fig. 2.9D). The robustness of the final contraction force in the pillar stiffness is captured by this simple model, if the effective spring constant of the network  $k_{am}$  is negligible compared to the spring constant of the pillars  $k_p$  over the entire experimentally considered range. In this 1D model, we expect  $k_{am} \propto G_{am} h / N$ , where  $N$  is the number of pillars and the numerical prefactor depends on the Poisson's ratio of the gel, which we do not know. In our case  $h$  is around  $4 - 5 \mu\text{m}$ ,  $N = 10$ , and we expect  $G_{am}$  to be of order a few Pascal on the timescale of the contraction (Mizuno *et al.*, 2007). Based on these numbers we do indeed expect  $k_{am} \ll k_p$ . Thus, we will proceed by modeling the actomyosin gel as a viscous fluid and neglects its elastic properties.

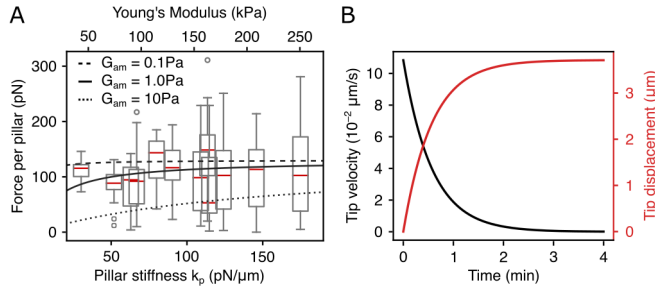


Figure 2.11: **Predictions of the one-dimensional contractility model with constant active force** (adapted from Jia *et al.*, 2022). **A.** The stiffness sensitivity of the final contraction force decreases with decreasing Young's modulus of the network. **B.** The contraction dynamics in response to a constant contractile force do not display the characteristic acceleration behavior observed experimentally.

### A dynamical model for contractile actomyosin in soft frames

Next, we go beyond the steady state force and construct a dynamic model for contractile actomyosin gels in soft frames. To do this, we have to account for viscous contributions. For this, we use the same geometry as before, but represent the viscous response of the actomyosin gel by a dashpot with an effective friction coefficient  $\gamma_{am}$  (Fig. 2.10).

The friction coefficient can be estimated from the 3D geometry of the contractile network, which allows us to relate the effective friction coefficient  $\gamma_{am}$  of the dashpot to the dimensions and the rheological properties of the actomyosin

network. Specifically, we approximate the actomyosin gel as a cylindrical linear elastic medium of radius  $R$  and height  $h$ . The height of the gel can be estimated from light microscopy images (Fig. 2.8B), which show that the gel attached approximately to the upper 30% of the pillars. Based on this geometry we then derive an expression for the effective friction coefficient  $\gamma_{\text{am}}$ . Based on the approximation of the actomyosin gel as a cylindrical linear continuous medium, we can derive a relation between the pillar force  $F_p$  and the velocity of the fluid's outer surface. For this, we first consider the viscous stress tensor (Landau *et al.*, 1987):

$$\sigma'_{\alpha\beta} = 2\eta \left( \dot{u}_{\alpha\beta} - \frac{1}{3} \delta_{\alpha\beta} \dot{u}_{\gamma\gamma} \right) + \zeta \delta_{\alpha\beta} \dot{u}_{\gamma\gamma}. \quad (2.28)$$

Here,  $\eta$  denotes the shear viscosity,  $\zeta$  is the volume viscosity, and the dots denote a temporal derivative. In the absence of external forces and neglecting inertial effects, we then obtain the following differential equation for the strain rate  $\dot{u}_{\alpha\beta}$  in an isotropic viscous fluid (Landau *et al.*, 1987):

$$0 = \left( \eta + \frac{1}{3} \zeta \right) \nabla (\nabla \cdot \dot{\mathbf{u}}) - \zeta \nabla \times (\nabla \times \dot{\mathbf{u}}). \quad (2.29)$$

Since the load  $\omega$  is applied radially,  $\dot{u}_\phi$  and all angular derivatives vanish. Additionally, we assume that the fluid remains in a perfectly cylindrical shape. Hence,  $\partial_z \dot{u}_r$  and  $\partial_r \dot{u}_z$  vanish. We can thus simplify this expression to

$$0 = \left( \eta + \frac{1}{3} \zeta \right) \nabla (\nabla \cdot \dot{\mathbf{u}}). \quad (2.30)$$

Writing Eq. (2.30) explicitly for the different non-zero components in cylindrical coordinates yields

$$0 = \partial_r \left[ \frac{1}{r} \frac{\partial(r\dot{u}_r)}{\partial r} \right], \quad (2.31)$$

$$0 = \partial_z^2 \dot{u}_z. \quad (2.32)$$

We place the center of the coordinate system in the center of the cylinder. Hence, we know that the velocity at the origin has to vanish due to symmetry, providing the following two boundary conditions:  $\dot{u}_r(r=0) = 0$  and  $\dot{u}_z(z=0) = 0$ . Integrating the two equations (Eq. (2.31) and (2.32)) with these boundary conditions gives the following velocity field:

$$\dot{u}_r(r) = a_r r, \quad (2.33)$$

$$\dot{u}_z(z) = a_z z. \quad (2.34)$$

To fix the remaining two integration constants  $a_r$  and  $a_z$ , we consider the stress in the system. We can relate the components of the velocity field to the viscous stress tensor via the constitutive relation

$$\sigma'_{\alpha\beta} = \eta \left( \partial_\alpha \dot{u}_\beta + \partial_\beta \dot{u}_\alpha - \frac{2}{3} \delta_{\alpha\beta} \partial_\gamma \dot{u}_\gamma \right) + \zeta \delta_{\alpha\beta} \partial_\gamma \dot{u}_\gamma. \quad (2.35)$$

Here,  $\delta_{\alpha\beta}$  denotes the Kronecker delta and repeated indices are summed over. The non-zero components are thus given by

$$\sigma'_{rr}(r) = 2 \left( \frac{\eta}{3} + \zeta \right) a_r + \left( \zeta - \frac{2}{3} \eta \right) a_z, \quad (2.36)$$

$$\sigma'_{\phi\phi}(r) = 2 \left( \frac{\eta}{3} + \zeta \right) a_r + \left( \zeta - \frac{2}{3}\eta \right) a_z, \quad (2.37)$$

$$\sigma'_{zz}(r) = 2 \left( \zeta - \frac{2}{3}\eta \right) a_r + \left( \zeta + \frac{4}{3}\eta \right) a_z. \quad (2.38)$$

To derive this, we used that  $\dot{u}_r(r=0) = 0$  and  $\dot{u}_z(z=0) = 0$  due to symmetry. We model the forces applied to the network by the pillars by a continuous load  $\omega = NF_p/A$  on the gel's outer surface  $A = 2\pi Rh$  (Fig. 2.10), where  $N$  denotes the number of pillars per ring. By using these boundary conditions ( $\sigma'_{rr}(r=R) = \omega = NF_p/A$  and  $\sigma'_{zz}(z = \pm h/2) = 0$ ), we can derive the expression for  $F_p(t)$

$$F_p(t) = \frac{A}{NR} \frac{6\eta}{1 + 4\eta/3\zeta} \dot{u}_r(r=R). \quad (2.39)$$

Note that this expression can be mapped onto the expression of an incompressible fluid with an effective viscosity  $\eta_{\text{am}}^{\text{eff}} = 6\eta/(1 + 4\eta/(3\zeta))$ . We can thus simplify this expression to

$$F_p(t) = \eta_{\text{am}}^{\text{eff}} \frac{6A}{NR} v_p(t). \quad (2.40)$$

Here,  $\eta_{\text{am}}$  denotes the viscosity of the actomyosin gel and  $v_p = d(\Delta x)/dt$  is the velocity of the tip of the pillars.

Eq. (2.40) is equivalent to the response of a simple one-dimensional dashpot with an effective friction coefficient of

$$\gamma_{\text{am}} = \eta_{\text{am}}^{\text{eff}} \frac{6A}{NR} = \frac{12}{N} \eta_{\text{am}}^{\text{eff}} \pi h, \quad (2.41)$$

where we used  $A = 2\pi Rh$ . Thus, the force balance describing the dynamics of our system reads

$$2k_p \Delta x = 2F_A - 2\gamma_{\text{am}} \frac{d\Delta x}{dt}. \quad (2.42)$$

Using  $F_p(t) = k_p \Delta x$  and  $\tau = \gamma_{\text{am}}/k_p$ , this can be rewritten in terms of a differential equation as

$$\frac{dF_p(t)}{dt} + \frac{F_p(t)}{\tau} = \frac{F_A}{\tau}, \quad (2.43)$$

which was found previously (Marcq *et al.*, 2011). For a constant value of  $F_A$  and an initial force  $F_p(t=0) = 0$ , the solution of Eq. (S23) is given by

$$F_p(t) = F_A \left( 1 - e^{-t/\tau} \right), \quad (2.44)$$

implying that

$$\Delta x(t) = \frac{F_A}{k_p} \left( 1 - e^{-t/\tau} \right), \quad (2.45)$$

and

$$v_p(t) = \frac{F_A}{k_p \tau} e^{-t/\tau}. \quad (2.46)$$

Importantly, however, these predictions quantitatively and qualitatively fail to capture the experimental data (Fig. 2.11B): Eq. (2.45) does not have an

inflection point and the velocity in Eq. (2.46) correspondingly exhibits no peak at  $t > 0$ . This implies that the active force  $F_A$  cannot be constant, but instead needs to increase over the course of the contraction. To account for this, we consider in the following two possible contributions: a density-dependence of the contractility, and the binding dynamics of the myosin motors.

### The density dependence of the active contractility

The first effect that could introduce a time dependence of the contractility of the network is the change in network density throughout the contraction process (Bendix *et al.*, 2008; Foster, Fürthauer, *et al.*, 2015; Joanny, Kruse, *et al.*, 2013). To generate a contractile force, a myosin filament has to connect two distinct actin filaments. The probability that a bound motor will indeed be in such a contractile configuration grows with increasing network density due to the increased number of possible binding sites within reach of the motor. Hence, for lower densities, we expect the active force generated by the actomyosin gel onto the pillars to scale linearly with the actin density and the number of bound myosin filaments. At high densities, steric interactions will counteract the contractile force, to leading order yielding a term that scales quadratically with the actin density. In total, this gives us the following expression for the active force as a function of the actin density (Chugh, Clark, *et al.*, 2017):

$$F_A(t) = \xi N_M \rho_a(t) (\rho_a^{\max} - \rho_a(t)). \quad (2.47)$$

Here,  $\xi$  is a phenomenological coupling parameter,  $N_M$  is the number of bound myosin filaments and  $\rho_a^{\max}$  is the maximal possible density that the gel can reach. While it is known that cortex thickness correlates with cortex contractility *in vivo* (Foster, Fürthauer, *et al.*, 2015), due to the large areal changes of the considered network in the  $x$ - $y$ -plane, for simplicity we considered only the increase in actin density from the in-plane contraction of the network. Furthermore, we neglect the effect of filament alignment. This is justified by the fact that we apply this model to crosslinked networks, in which the effects of motor induced fiber alignment are reduced in comparison to non-crosslinked networks (Koenderink, Dogic, *et al.*, 2009).

Inserting the density dependent active force (Eq. (2.47)) into Equation (2.43) yields

$$\frac{dF_p(t)}{dt} + \frac{F_p(t)}{\tau} = \frac{\xi}{\tau} N_M \rho_a(t) (\rho_a^{\max} - \rho_a(t)). \quad (2.48)$$

Solving Equation (2.48) can indeed reproduce the observed acceleration behavior (Fig. 2.12B, solid lines). However, this model lacks predictive power. We demonstrate this by fitting the model to the displacement curve at a single pillar stiffness ( $k_p = 35$  pN/ $\mu$ m) that is shown in Fig. 2.12B and then try to predict the final contraction force at different pillar stiffnesses. In contrast to the experimental data, this model predicts a strong stiffness dependence of the final force (Fig. 2.12A). Also, the acceleration can only be observed for a very limited range of pillar stiffnesses (below  $k_p = 60$  pN/ $\mu$ m). At higher stiffnesses we find a monotonic decrease in velocity (Fig. 2.12B, transparent lines) reminiscent of the model with a constant active force. We thus conclude that the density dependence of the active force alone is not sufficient to explain the observed contraction behavior.

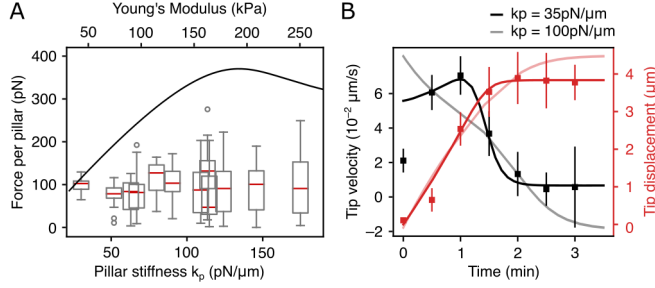


Figure 2.12: **Fits and predictions of the density dependent contractility model** (adapted from Jia *et al.*, 2022). **A.** The predicted final contraction force (solid line) shows a strong stiffness dependence, which is in contrast to the experimental data (box plot). **B.** While the experimental contraction dynamics can be fitted for soft pillars, the predicted dynamics at higher stiffnesses lack the characteristic acceleration of the contraction.

### The role of load-dependent myosin unbinding kinetics

From the previous sections, it becomes apparent that we are still missing a key ingredient in our model to explain the observed stiffness-dependent acceleration of the contraction dynamics as well as the robust, stiffness-independent steady-state force generation. One aspect that we did not consider so far, is the load-sensitivity of the myosin binding and unbinding kinetics (see Section 2.1). To explore this option, we need to connect the experienced by individual myosin filaments  $F_M$  to the force that is exerted onto the pillars. We do this by assuming that the force, generated by the deflected pillars is distributed over all myosin filaments and that the active force is proportional to the number of bound filaments. Thus, we take a mean-field approach and assume that every motor is subject to a load

$$F_M = aF_p, \quad (2.49)$$

where we introduce a phenomenological proportionality constant  $a$ . Our contractility model is then defined by the two coupled differential equations:

$$\frac{dF_p(t)}{dt} + \frac{F_p(t)}{\tau} = \frac{\xi}{\tau} N_M(t) \rho_a(t) (\rho_a^{\max} - \rho_a(t)), \quad (2.50)$$

$$\frac{dN_M(t)}{dt} = k_{\text{on}} [N_M^{\max} - N_M(t)] - k_{\text{off}}(aF_p(t)) N_M(t), \quad (2.51)$$

where  $k_{\text{on}}$  denotes the binding rate of myosin filaments and the filament unbinding rate  $k_{\text{off}}$  is defined by Eqs. (2.13) – (2.15).

Thus, filaments can constantly bind to and unbind from the network in a load sensitive manner, resulting in a feedback loop that can either be positive (in the catch regime) or negative (in the slip regime). In the beginning of the experiment, myosin filaments are in solution and first have to bind to the network to generate contractile forces. As the force builds up, the load-dependent myosin kinetics result in an increased number of motors being engaged in force generation. The inherent positive feedback between the slow build-up of viscoelastic network stresses and the active force generation by fast load-dependent myosin binding kinetics in our model gives rise to the intricate

contraction dynamics of the pillar ring, in quantitative agreement with our experiments (Fig. 2.13A, inset).

To test the predictive power of our model, we constrain the model parameters by fitting the model to a single contraction curve at one pillar stiffness (Fig. 2.13A, inset) and then compute the stiffness-dependence of the contraction of the pillar ring assay. Strikingly, this model accurately predicts the dynamics (Fig. 2.13A) and steady-state values (Fig. 2.13B) of the actively generated forces over a broad range of pillar stiffness. The stiffness insensitivity of the steady-state force can be explained by our contractility model, provided that the network’s elastic response is much softer than the pillar stiffness and can thus be neglected. Conceptually, the load sensitivity of the myosin binding kinetics results in active force generation, which is largely controlled by the internal stress of the actin network and is insensitive to the stiffness of the frame. This appears to be the crucial mechanism behind the observed contraction behavior as indicated by the failure of the purely actin density-dependent contractility model. However, while for the steady state, the density-dependent effects seem to only have a small impact, we find that the density dependence is essential to understand the stiffness dependence of the contraction velocity. This is the case since motor filament binding kinetics only couple to the pillar force but not to their displacement and thus not to the pillar stiffness. The density dependence of the contractility in contrast couples the contractility also to the pillar stiffness. We thus conclude that accounting for both the density dependence of the contractility and the (un-)binding dynamics of the myosin filaments is essential for the understanding of the contraction behavior of the fabricated structures.

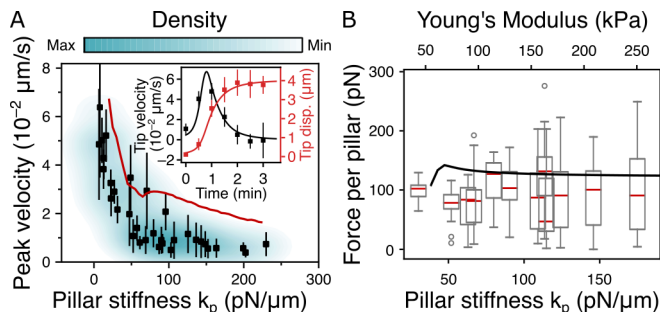


Figure 2.13: **Fits and predictions of the full model with load-sensitive myosin binding kinetics** (adapted from Jia *et al.*, 2022). **A.** The model successfully predicts the stiffness-dependence of the peak contraction velocities based on fitting it to the contraction dynamics for a single pillar stiffness (inset,  $k_p = 35 \text{ pN}/\mu\text{m}$ ). **B.** It also correctly predicts the relative stiffness independence of the final contraction force.

## 2.5 Discussion and outlook

Overall, while we found in this project that reconstituted actomyosin networks do display an inherent mechanosensitivity in their contraction dynamics due to the load-dependence of myosin binding and unbinding kinetics, we also

found that crosslinked actomyosin networks are not a minimal system to reproduce the mechanosensitive force generation observed in living cells (Trichet *et al.*, 2012). This is surprising, since some of the physical models for cellular force generation are purely based on geometric arguments and the mechanical properties of cells, which to a large part originate from internal actin structures (Marcq *et al.*, 2011). A possible reason for this difference between reconstituted networks and cells, could be the degree of crosslinking, which strongly affects the stiffness of the network. Thus, at higher degrees of crosslinking, one might still be able to reproduce the behavior observed in cells. Myosin induced actin fragmentation as observed experimentally (Vogel *et al.*, 2013) on the other hand could inherently decrease the network connectivity, potentially making the degree of crosslinking irrelevant. Here, it would be interesting to go beyond the case of skeletal muscle myosin II, which forms large myosin clusters and explore the contraction behavior of non-muscle myosin II. These tests could allow to further differentiate the contributions of adhesion molecules and the actomyosin network to the observed cellular mechanosensitivity.

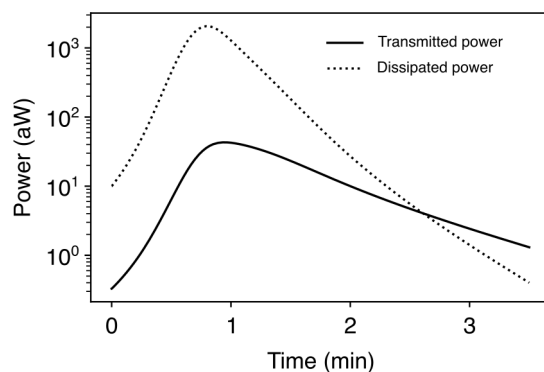


Figure 2.14: **Power generation in contractile actomyosin gels** (taken from Jia *et al.*, 2022). Estimate of the transmitted and dissipated power of the contraction shown in the inset of Fig. 2.13A ( $k_p = 35$  pN/ $\mu\text{m}$ ) based on our theoretical model.

Apart from serving as a potential model system to understand cellular rigidity sensing, our contractility model together with the experimental results could also yield insights into thermodynamic properties of the contraction process, which could be relevant for the engineering of active biomaterials (Foster, Bae, *et al.*, 2023). For example, the model can be used to estimate the generated mechanical power of the actomyosin network in the pillar ring assay. Part of the work performed goes into the elastic deformation of the pillar frames and part of the work is dissipated. The dissipated work  $W_{\text{dis}}$  in the model, however, only accounts for viscous dissipation and does not account for effects of the motors that cannot contribute to the overall contraction. It can thus only serve as a lower bound for the total amount of dissipated energy. If the pillars are deflected by  $\Delta x_f$  in the final contracted state, the total work is given by:

$$W_{\text{tot}} = W_{\text{trans}} + W_{\text{dis}} = N \int_0^{\Delta x_f} k_p \Delta x d\Delta x + N \int_0^{\Delta x_f} 2\gamma_{\text{am}} v_p d\Delta x. \quad (2.52)$$

Here, the number of pillars  $N$  accounts for the fact that our model is one dimensional. Note that the additional factor of two in the expression for  $W_{\text{dis}}$  is a consequence of the geometry, which implies that the contraction velocity of the gel is twice the deflection velocity of the pillars  $v_p$ . Rewriting the right-hand side of Eq. (2.52) as integrals over time yields the following expressions for the dissipative and transmitted components of the generated power:

$$P_{\text{dis}}(t) = 2N\gamma_{\text{am}}v_p(t), \quad (2.53)$$

$$P_{\text{trans}}(t) = 2Nk_p\Delta x(t)v_p(t). \quad (2.54)$$

As shown in Fig. 2.14, we observe a strongly peaked profile in both the dissipated and the transmitted power with a peak transmitted power of  $43 \cdot 10^{-18}$  W. This peaked profile is a consequence of the acceleration in the contraction process, demonstrating how load-sensitivity of the myosin binding and unbinding kinetics does shape the contraction dynamics but also has important implications for thermodynamic aspects of the system, such as power generation. Here, it would be interesting to test these predictions by applying direct and indirect experimental measurements of energy dissipation and propagation (Floyd *et al.*, 2019; Foster, Bae, *et al.*, 2023; Seara *et al.*, 2018) that were developed for freely contracting and non-contractile polymer gels to our system.s

## The cytoskeleton in confined and directed cell migration

In this chapter, we build on our understanding of subcellular components of cellular force generation machinery developed in the previous Chapter to analyze how cellular behavior and in particular mesenchymal migration patterns emerge from the interplay of the different underlying molecular components of the cytoskeleton. Due to the importance of cell migration in key physiological processes such as development (Franz *et al.*, 2002; Scarpa *et al.*, 2016; Weijer, 2009), wound healing (Fenteany *et al.*, 2000; Krawczyk, 1971; Poujade *et al.*, 2007; Vishwakarma *et al.*, 2020), the immune system (Friedl and Weigelin, 2008; Parkin *et al.*, 2001) and cancer metastasis (Clark *et al.*, 2015; Stuelten *et al.*, 2018; Yamaguchi *et al.*, 2005), great research efforts were put towards developing a better understanding of cell migration over the last decades. The observation that the underlying molecular processes are conserved across a wide range of eukaryotic migration modes and largely independent of the physiological context drove efforts to find an overarching conceptual framework describing eukaryotic cell migration (Abercrombie, 1980; Danuser *et al.*, 2013). This generality together with the abundance of experimental data makes the problem of eukaryotic cell migration particularly attractive for theoretical modeling, since an integrated, holistic model of migrating cells would have an unusually broad range of applications in different biological systems. Despite the detailed knowledge of both the underlying molecular processes as well as the phenomenological migration behavior of cells, there is a strong fragmentation of modeling approaches with detailed microscopic models that focus on subcellular processes on the one hand (Danuser *et al.*, 2013; Edelstein-Keshet *et al.*, 2013) and more phenomenological and data-driven approaches on the other hand (Brückner and Broedersz, 2023). Bridging the gap between these two approaches and relating the emergent migration behavior directly to underlying molecular processes would allow to better predict how changes in the cellular environment would change the migration behavior and would thus greatly increase the generality of coarse grained cell migration models.

To bridge this gap, we first review the phenomenological migration behavior of mesenchymal cells on structured two-dimensional substrates and discuss previous phenomenological and data driven modeling approaches describing the observed migration behavior. We then discuss key molecular processes and

their interaction underlying mesenchymal cell migration. Based on this, we then develop a mechanistic model that accounts for these molecular processes that we systematically coarse grain to obtain a simple model for the emergent migration behavior. To guide this coarse graining, we use a data-driven model that was previously constrained from experimental data (Brückner, Schmitt, *et al.*, 2022), which we ultimately rediscover from our bottom-up model. From this we obtain a mechanistic interpretation of a number of key aspects of this data-driven model and show that our model can be generalized to describe the migration behavior on various different substrates, allowing us to connect our model to other phenomenological models and yielding new insights into cellular migration behavior and decision making in complex environments.

### 3.1 Phenomenological and data-driven models for cell migration on structured surfaces

*In vivo*, migrating cells interact with a similarly complex extracellular environment (Charras and Sahai, 2014; Roussos *et al.*, 2011). This makes migration in physiological conditions not well suited to constrain simple, biophysical migration models. Following a more reductionist approach, cell migration was extensively studied on well defined, structured surfaces (Brückner, Fink, Schreiber, *et al.*, 2019; Caballero, Comelles, *et al.*, 2015; Maiuri *et al.*, 2015; Selmeçzi, Li, *et al.*, 2008; Trichet *et al.*, 2012). This led to the discovery of a number of key aspects in the phenomenology of migrating cells that were formalized in simple, top-down models that were constrained directly from data and that are largely agnostic to the underlying molecular processes (Brückner and Broedersz, 2023; Selmeçzi, Li, *et al.*, 2008). Here, we briefly summarize the observed phenomenology together with a number data-driven and phenomenological models that were developed for migration on different patterns.

Early studies of eukaryotic single-cellular organisms swimming in homogeneous environments found a simple diffusive behavior (Fürth, 1917; Przi Bram, 1913) (see Selmeçzi, Li, *et al.*, 2008 for an english review). A more detailed analysis of the mean square displacement of the cells on shorter time scales by (Fürth, 1920) revealed however deviations from a simple diffusive behavior that Fürth could explain in terms of an inherent persistence in the movement of the cells. He proposed to model cellular movement in terms of a persistent random walk, where the walker moves along a (one dimensional) lattice with lattice spacing  $\Delta x$  and a hopping time  $\Delta t$ . The persistence is introduced by determining the preferred direction of the next step based on the direction of the previous step, with  $\lambda\Delta t$  being the probability to switch direction from one step to the other. The probability  $p_{\pm}(x, t)$  that a walker (the cell) at position  $x$  and time  $t$  moves in the  $\pm$ -direction is then given by (Fürth, 1920; Kac, 1974)

$$p_{\pm}(x, t + \Delta t) = (1 - \lambda\Delta t)p_{\pm}(x \mp \Delta x, t) + \lambda\Delta t p_{\mp}(x \mp \Delta x, t). \quad (3.1)$$

In the continuous limit  $\Delta t \rightarrow 0$  and  $\Delta x \rightarrow 0$ , with  $\Delta x/\Delta t = v_0 = \text{finite}$ , Eq. (3.1) gives rise to the so-called *telegrapher's* equation for the total probability  $p = p_+ + p_-$  (Balakrishnan, 1993; Kac, 1974)

$$\partial_t^2 p + 2\lambda\partial_x p = v_0^2 \partial_x^2 p, \quad (3.2)$$

which is equivalent to the overdamped Langevin equation (Sandev *et al.*, 2022)

$$\dot{x} = v_0 \eta(t), \quad (3.3)$$

where  $\eta(t)$  denotes so-called *dichotomic* noise that switches between the values  $\pm 1$  at an average rate  $\lambda$  and  $\langle \zeta(t) \rangle = 0$ . The mean square displacement of a particle following Eq. (3.2) agrees well with the data in (Fürth, 1920). An alternative model for persistent random motion that gives rise to the same mean square displacement can be formulated in terms of the underdamped Langevin equation (Langevin, 1908; Lemons *et al.*, 1997)

$$\dot{v} = -\zeta v + \sigma \xi(t), \quad (3.4)$$

where  $v = \dot{x}$  is the velocity of the particle,  $\zeta$  denotes an effective friction coefficient,  $\sigma$  the noise amplitude, and  $\xi(t)$  represents Gaussian white noise with  $\langle \xi(t) \rangle = 0$  and  $\langle \xi(t)\xi(t') \rangle = \delta(t - t')$ , where the underdamped nature of the cellular dynamics do not arise from inertia, as cells are living at low Reynolds numbers (Needleman *et al.*, 2019), but should be interpreted as an emergent property of the cellular migration machinery. Eq. (3.4) indeed gives rise to the same expression for the mean square displacement as Eqs. (3.2) and (3.3) (Uhlenbeck *et al.*, 1930). Cell migration as persistent random motion as described by Eqs. (3.2) and (3.4) or modifications of those were later shown to be applicable far beyond the swimming motion of single-cellular organisms and in particular can also successfully describe mesenchymal cell migration on a number of different substrates (Fig. 3.1), some of which we will discuss in the following.

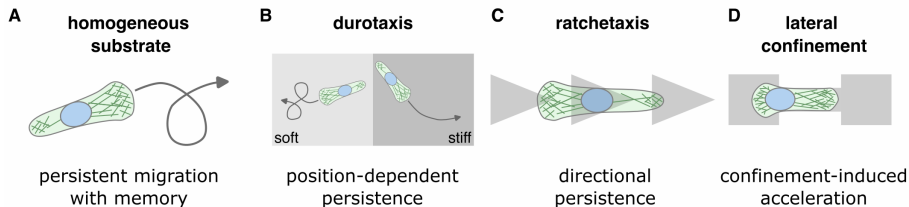


Figure 3.1: **Overview of phenomenological models for persistent random motion of cells on different substrates.** **A.** Cells on homogeneous substrates can be described by an underdamped Langevin equation with internal memory. **B.** Durotaxis can arise from a persistent random walk with a stiffness- and thus position-dependent persistence. **C.** Cellular Ratchetaxis can be described as a discrete persistent random walk with a different persistence depending on the direction of migration. **D.** The effect of confinement on the cell dynamics can be captured by an underdamped Langevin equation with a position and velocity dependent deterministic drift that accounts for the local pattern geometry and orientation.

While Eqs. (3.1)–(3.4) were obtained based on manual tracking of cellular trajectories, automated cell tracking allowed for much better statistics and consequently a more precise quantification of the cellular migration dynamics. This revealed on the one hand that cellular migration dynamics can in fact be more complex than a simple persistent random walk but also provided the

means to select and constrain more complex migration models (Selmeczi, Li, *et al.*, 2008). In particular, migration data of cells migrating on unstructured two dimensional surfaces (Fig. 3.1A) revealed that the autocorrelation of the cellular velocity decays as a double exponential, in contrast to the single exponential decay predicted by Eq. (3.4) (Selmeczi, Mosler, *et al.*, 2005), which can be explained in terms of an internal memory of cells that goes beyond the effective inertia term in Eq. (3.4). Capturing this behavior requires the introduction of a memory kernel, leading to (Selmeczi, Mosler, *et al.*, 2005)

$$\dot{v} = -\zeta_1 v(t) + \zeta_2 \int_{-\infty}^t dt' e^{-\gamma(t-t')} v(t') + \sigma(v(t))\xi(t), \quad (3.5)$$

where the model parameter  $\zeta_1$ ,  $\zeta_2$  and  $\gamma$  from fitting the experimental data. For a different cell line, Eq. (3.5) was found to require even further refinement by introducing a velocity dependence of  $\zeta_1(v)$ , resulting in a non-linear Langevin equation (Selmeczi, Mosler, *et al.*, 2005).

Other adaptations of the persistent random walk model were found to be necessary when applying it to migration on unisotropic substrates. For example, many cell lines have a tendency to migrate towards stiffer regions on a substrate, a behavior termed *durotaxis* (C.-M. Lo *et al.*, 2000; Sunyer and Trepats, 2020). Coincidentally, cells display an increased migratory persistence on stiffer substrates (House *et al.*, 2009; Raab, Swift, *et al.*, 2012) (Fig. 3.1B), which motivated the development of a persistent random walk model with a position (and thus stiffness) dependent persistence by adapting Eq. (3.2) (Novikova *et al.*, 2017)

$$\partial_t^2 p + 2\lambda(x)\partial_t p = v_0^2 \partial_x^2 p. \quad (3.6)$$

Eq. (3.6) is indeed sufficient to reproduce biased migration towards a stiffer region (Novikova *et al.*, 2017), a more detailed quantitative comparison with experimental statistics that would be required to identify if stiffness dependent migration persistence is indeed the dominant driver behind durotaxis is however lacking. A similar approach was used to explain biased migration induced by an anisotropy in the adhesive properties of the substrate, which was called *ratchetaxis* (Caballero, Comelles, *et al.*, 2015). There, cells migrate on periodic chains of asymmetric patterns that result in different adhesive properties on both sides of the cell (Fig. 3.1A). This process was successfully modeled in terms of discrete, persistent random walker (Eq. (3.1)), with asymmetric switching rates  $\lambda_{\pm}$ , such that  $\lambda_{\pm}\Delta t$  denotes the switching probability for a cell that stepped in the  $\pm$ -direction in the previous step ( $\lambda_+\Delta t$  and  $\lambda_-\Delta t$  correspond to  $\pi_{-+}$  and  $\pi_{+-}$  in (Caballero, Voituriez, *et al.*, 2014), respectively). This results in the modified version of Eq. (3.1) (Caballero, Voituriez, *et al.*, 2014)

$$p_{\pm}(x, t + \Delta t) = (1 - \lambda_{\pm}\Delta t)p_{\pm}(x \mp \Delta x, t) + \lambda_{\mp}\Delta t p_{\mp}(x \mp \Delta x, t). \quad (3.7)$$

Interestingly, a simple one step persistence was sufficient in this case in contrast to the additional memory kernel required to describe migration on homogeneous substrates (Selmeczi, Mosler, *et al.*, 2005).

Finally, we want to discuss the migration behavior of cells in geometric confinement on two-state micropatterns. In that case, the persistence of the cell will depend on the local geometry of the pattern, which can be captured in terms of a generalization of Eq. (3.4) (Brückner, Fink, Schreiber, *et al.*, 2019;

Brückner, Ronceray, *et al.*, 2020)

$$\dot{v}(x, v) = F(x, v) + \sigma(x, v)\xi(t), \quad (3.8)$$

where  $F(x, v)$  denotes the position- and velocity-dependent deterministic contribution (drift) to the nuclear dynamics and  $\sigma$  and  $\xi$  are defined analogously to Eq. (3.4) except that also the noise strength  $\sigma$  can in principle also vary with position and velocity. For the case of cells migrating on patterns that consist of two square-shaped islands that are connected by a narrow bridge (Fig. 3.1D), Brückner *et al.* were able to infer the values of  $F(x, v)$  and  $\sigma(x, v)$  from experimental data and show that Eq. (3.8) can accurately describe the observed migration dynamics (Brückner, Fink, Schreiber, *et al.*, 2019). Similar to the case of ratchetaxis, also on two-state patterns, no memory kernel was needed to explain the observed migration behavior, which could be due to a reset of the internal cellular organization on the islands. The inferred values of  $F(x, v)$  on such two-state patterns revealed an interesting acceleration behavior of the cells as they entered into the channel, which led to a deterministic cycling from one island to the other. To understand the mechanistic origin of this acceleration, in subsequent work they went beyond the description of the cell in terms of its overall location to a more detailed model that accounts for more degrees of freedom (Brückner, Schmitt, *et al.*, 2022). In particular, these included the nuclear position  $x_n$ , the position of an experimentally protrusion coordinate  $x_p$  and the cell polarity  $P$  (Fig. 3.2). By segmenting the full cellular morphology compared to only tracking the nucleus or centrosome, they were able to systematically constrain the structure of such a mechanistic model from experimental data, which led to the following set of equations:

$$\zeta_n(x_n)\dot{x}_n = k(x_p - x_n) \quad (3.9)$$

$$\zeta_p\dot{x}_p = -k(x_p - x_n) - \partial_{x_p}V(x_p) + P(t) \quad (3.10)$$

$$\dot{P} = -\alpha(x_p)P(t) - \beta P(t)^3 + \sigma\xi(t) \quad (3.11)$$

Here,  $\zeta_{n,p}$  denotes the friction experienced by the nucleus or the protrusion, the spring constant  $k$  characterizes the linear elastic coupling between nucleus and protrusion, the confining potential  $V(x_p)$  accounts for the boundaries of pattern, and the parameters  $\alpha$  and  $\beta$  determine the stochastic dynamics of the protrusion. On the islands,  $\alpha > 0$  and the polarization fluctuates around zero. In confinement however, the sign of  $\alpha$  can switch, resulting in a reinforcement of deviation of  $P$  away from zero and thus a finite average polarization, where  $\beta > 0$  ensures that the polarity remains bounded. In this model, the interplay between nucleus, protrusion and polarization give rise to effective underdamped dynamics of the nuclear coordinate, demonstrating how the effectively underdamped migration dynamics of cells can emerge from the interplay of different degrees of freedom whose individual dynamics are overdamped. Further, this model presents an explanation for the observed confinement-induced accelerations in Brückner, Fink, Schreiber, *et al.*, 2019 in terms of a coupling between cellular confinement and polarization.

The mechanistic model presented in Brückner, Schmitt, *et al.*, 2022 represents a first attempt to obtain more mechanistic insights from data-driven models. However, due to their phenomenological nature these models can only

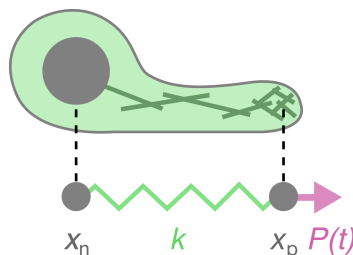


Figure 3.2: **Sketch of the data-driven mechanistic model derived in Brückner, Schmitt, *et al.*, 2022.** The cellular migration dynamics are captured by three coupled degrees of freedom: the nuclear position  $x_n$ , the protrusion coordinate  $x_p$ , and the cell polarity  $P$ .

give limited insights into the underlying molecular processes and cannot easily be generalized to other substrates since they have to be constrained from experimental data first. If they are systematically and thoroughly constrained from experimental data, their mathematical structure represents however a well-defined target for coarse-graining more detailed, bottom-up models to the mesoscopic level without relying on uncontrolled approximations. This applies in particular to models that can be formulated in terms of a Langevin equation with Gaussian white noise, which is the natural formalism to describe the molecular dynamics of subcellular components.

### 3.2 The biophysics of cell migration: The four step process

Connecting the emergent migration phenomenology to the underlying molecular processes requires a detailed knowledge of the cellular migration machinery. Even as late as 1970 however, Abercrombie stated that the "mechanism of locomotion of metazoan cells [...] can fairly be said to be wholly unknown" (Abercrombie *et al.*, 1970). The reason for this was that while the active locomotion of microbes was established early on and systematically studied as early as the 1830s (De Bruyn, 1947), the ability of active locomotion was not considered a common and fundamental feature in animal cells (Abercrombie, 1980). This changed however, by the time of Abercrombie's famous Croonian Lecture in 1978 (Abercrombie, 1980) where he united active migration phenomena in the previously independent fields of wound healing, development, and cancer invasion (Abercrombie, 1977) in terms of shared underlying molecular processes that he conceptualized in an overarching qualitative model of eukaryotic cell migration that stands correct as a conceptual framework until today (Abercrombie, 1980; Danuser *et al.*, 2013).

His model starts with a polarized cell (Fig. 3.3A) and divides the migration process into four distinct processes (Abercrombie, 1980; Danuser *et al.*, 2013):

1. Protrusion growth (Fig 3.3B)
2. Adhesion formation at the front (Fig 3.3B)
3. Adhesion disassembly at the rear (Fig 3.3C)

## 4. Contraction of the cytoplasm (Fig 3.3C)

While Abercrombie's original model was agnostic to whether those processes are sequential or are performed in parallel, it is now well understood that in most cells all four steps run in parallel (Danuser *et al.*, 2013). In the following we will dive deeper into the process of polarization and the individual steps of Abercrombie's model.

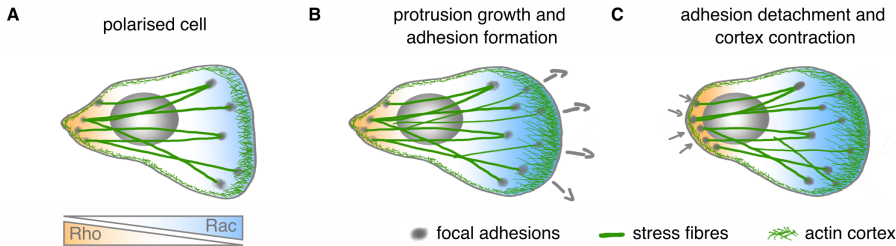


Figure 3.3: **The four step process of mesenchymal cell migration.** **A.** Migration is preempted by the polarization of the cell, with a number of molecular markers such as members of the Rho and Rac families being enriched towards the front and the rear of the cell. These polarity markers control molecular processes such as actin polymerization and cortex contractility. **B.** At the front of a migrating cell, protrusion growth is driven by actin polymerization against the membrane. The newly formed protrusion is stabilized through the formation of focal adhesions. **C.** At the rear of a migrating cell, focal adhesions disassemble and cortex contractions lead to a retraction of the rear.

### Cell polarization

While the process of polarization was not discussed in the Croonian lecture, it is an essential prerequisite to cell migration, since it establishes a front and a rear of the cell. Cell polarization in higher organisms involves a number of polarity protein complexes that are conserved throughout evolution. These include the PAR complex, the CRB complex and the SCRIB complex. Their downstream signaling induces cellular asymmetries and affects the cellular migration machinery. Of the three complexes, the SCRIB complex antagonizes the CRB and PAR complexes, while they act together in shared pathways (see Assémat *et al.*, 2008 for a comprehensive review). The polarity protein complexes interact with the Ras superfamily, which themselves play a crucial role in the establishment of cell polarization. Here, we only focus on the role of the three most commonly studied members of Ras superfamily: RhoA, Cdc42 and Rac1 (Iden *et al.*, 2008).

In the context of cell migration, the effect of RhoA on the Rho-associated protein kinase (ROCK) plays a central role (Fig. 3.4). ROCK increases myosin activity, resulting in a higher contractility as well as the formation of stress fibers and focal adhesions (Iden *et al.*, 2008; Leung *et al.*, 1996; Riento *et al.*, 2003). ROCK also indirectly inhibits actin depolymerization and thus stabilizes actin filaments. As a result less G-actin is available, which slows actin polymerization (Maekawa *et al.*, 1999; Riento *et al.*, 2003). Since actin

polymerization is essential for protrusion growth and myosin contractility drives the rear contraction of the cytoplasm, the RhoA concentration is increased in the rear of the cell (Fig. 3.3A and 3.4B).

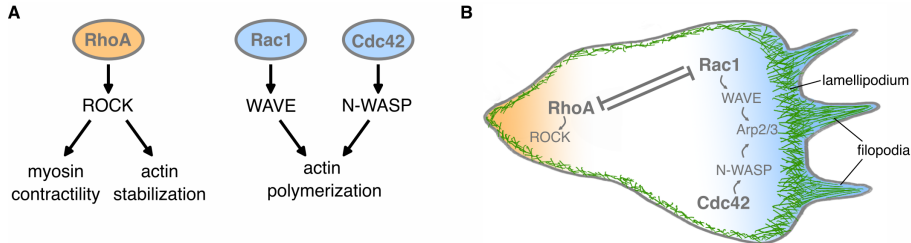


Figure 3.4: **The role of key members of the Ras superfamily.** **A.** Simplified scheme of the role of three key members of the Ras superfamily on important cellular processes for the four step process. **B.** Localization of and interaction between RhoA, Rac1 and Cdc42 within the cell.

Rac1 and Cdc42 both activate the Arp2/3 complex, which initiates the growth of new actin filaments and is thus essential for protrusion growth at the front of the cell (Jaffe *et al.*, 2005; Millard *et al.*, 2004) (see next paragraph for more detail). The activation of Arp2/3 happens however through two distinct pathways. Cdc42 binds to Neural Wiskott–Aldrich syndrome protein (N-WASP) to activate Arp2/3, while Rac1 affects Arp2/3 through another member of the Wiskott–Aldrich syndrome protein family, the WAVE (WASP family Verprolin homolog) regulatory complex (Iden *et al.*, 2008) (Fig. 3.4). As a consequence, during cell migration Rac1 and Cdc42 stimulate the growth of actin protrusions with different morphologies. Rac1 leads to the formation of flat, sheet like protrusions called lamellipodia, while Cdc42 triggers the growth of narrow, fingerlike protrusions called filopodia (Kozma *et al.*, 1996). Beyond that, there are also direct interactions between the different members of the Rac superfamily. In particular, Rac1 and Rho-ROCK inhibit each other, reinforcing the polarization of the cell (Iden *et al.*, 2008; Nakayama *et al.*, 2008) (Fig. 3.4B).

The complex interaction network involved in cell polarization poses a challenge to mathematical modeling approaches (Edelstein-Keshet *et al.*, 2013). Due to its regulatory role for other migration processes it is however a key component in many cell migration models (Danuser *et al.*, 2013).

### Actomyosin contractility

A key process that is controlled by the local distribution of polarity markers is actomyosin contractility (Iden *et al.*, 2008). During migration actomyosin contractility is essential for two distinct processes: translocation of the cell body including the nucleus and rear retraction. This can involve a number of structurally different actomyosin networks including the disordered actin cortex below the cell membrane (Martini *et al.*, 2010; Paluch *et al.*, 2013), highly structured stress fibers (Burrige and Guilly, 2016; Pellegrin *et al.*, 2007), and a contractile network in the crossover region between protrusion and cell body (Svitkina *et al.*, 1997). Cortex contractility is likely to play

a more prominent role in three dimensional environments, where it can lead to blebbing based migration (Lomakin *et al.*, 2020) or drive migration even in the absence of protrusion formation (R. Hawkins *et al.*, 2011) while stress fibre contractility is not essential for mesenchymal cell migration (Burrige and Guilly, 2016). Thus, even though cortex contraction and stress fibers support detachment of focal adhesions in the rear, we focus on the contractile network in the crossover region as the key contractile unit for mesenchymal cell migration on 2D substrates, while the role of rear contractility in 3D confined migration is explored in Chapter 2.

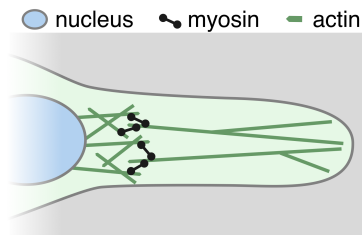


Figure 3.5: **Sketch of the overlapping actin networks that generate contractile forces in the cell.** A highly oriented protrusion-associated actin network overlaps with a disordered, nucleus-associated network. Myosin motors accumulate in this cross-over region and result in contractile force generation.

To generate a contractile force that pulls the nucleus towards the leading edge of the cell, myosin motors need to link filaments coming from the front of the protrusion to filaments associated with the nucleus (Fig. 3.2). Consistent with this, myosin was found to accumulate in migrating cells in the crossover region between the cell body and the protrusion (Svitkina *et al.*, 1997) where the protrusion-associated actin network overlaps with the nucleus-associated network. Actomyosin contractility can both be found in highly organized structures like stress fibers as well as in completely disordered actin networks (see Chapter 2). Nonetheless, the relative orientations of connected actin filaments controls the orientation and sign of the generated local force dipole (Lenz, 2014). Consequently, highly aligned actin structures such as sarcomeres or stress fibers, will generate contractile forces along a well defined axis, while myosin activity in disordered actin networks results in an isotropic contraction (Schuppler *et al.*, 2016). In the crossover region between protrusion and cell body, we find a partially aligned network (Small *et al.*, 1995; Svitkina *et al.*, 1997): At the front of the protrusion, the vast majority of actin filaments is oriented with their barbed ends towards the front (close to 80%) (Small *et al.*, 1995; Svitkina *et al.*, 1997). This represents the ideal orientation to generate a contraction along the nucleus-protrusion axis, since myosin II motors progress towards the barbed end of an actin filament (Hartman *et al.*, 2012). A smaller fraction of filaments (about 20%) is oriented orthogonal to the direction of migration (Small *et al.*, 1995; Svitkina *et al.*, 1997) and is thus not actively contributing to the translocation of the nucleus. In the contractile region between the protrusion and the cell body, the fraction of these orthogonally oriented filaments increases, likely due to actin reorientation caused by myosin contractility (Svitkina *et al.*, 1997). Finally, a small number of filaments is oriented

with their pointed ends towards the front of the protrusion (Small *et al.*, 1995; Svitkina *et al.*, 1997), which would in principle result in an extensile local force dipole (Lenz, 2014). Due to the small number of such extensile configurations and the fact that filament buckling prevents the long range transmission of extensile forces in actin networks (Ronceray, Broedersz, *et al.*, 2016), their contribution to the overall contractile force can however likely be neglected. As a consequence, filaments in the protrusion-associated actin network are predominantly found with their barbed ends oriented towards the protrusion front, which should result in a strongly directed contraction. Consistent with this, traction forces at the front of migrating cells are found to be typically oriented orthogonal to the membrane, pointing towards the cell body (Du Roure *et al.*, 2005).

This highly oriented protrusion-associated network overlaps with a disordered nucleus-associated network of mixed orientation (Verkhovskiy *et al.*, 1997). When these two networks are connected by myosin motors, this then leads to a mix of relative orientations of the connected filaments and consequent force dipoles. The dominant contribution to the contractile force is due to actin filaments oriented with their barbed ends towards the protrusion front. This can then lead to two qualitatively different relative orientations: parallel and anti-parallel. Approximately anti-parallel filaments will generate a predominantly contractile force dipole along the nucleus-protrusion axis (Lenz, 2014), while approximately parallel filaments will either result in no force or a contractile force orthogonal to the nucleus-protrusion axis (Lenz, 2014). The latter will thus not contribute to the nuclear translocation. Hence, the overall translocation force actin on the cell body is determined by the number of anti-parallel actin filaments in the crossover region.

### Protrusion growth

To allow a continuous translocation of the cell body, the leading protrusion needs to constantly expand during migration to stay ahead of the cell body. This process is driven by actin polymerization: The increased concentration of Rac1 and Cdc42 near the leading edge of polarized cells leads to a high degree of actin polymerization toward the cell membrane at the front of the cell. The pushing of the actin network against the plasma membrane generates a pressure resulting in an expansion of the cell front (Mogilner and Oster, 1996). Hence, the rate of actin polymerization and thus the growth velocity of the cell's leading edge is determined by the local concentration of actin monomers as well as the mechanical properties of the actin network (Mogilner and Oster, 1996; Mogilner and Rubinstein, 2005), which both depend on the degree of cell polarization (Iden *et al.*, 2008). To understand how the actin concentration and the network mechanics determine the leading edge dynamics, we consider minimal model for actin force generation against a plasma membrane (Mogilner and Oster, 1996).

The force generation through actin polymerization relies on continuous insertion of actin monomers at the tip of the filament in a brownian ratchet like mechanism termed *polymerization ratchet* (Mogilner and Oster, 1996; Peskin *et al.*, 1993). This requires however the occurrence of a gap between the tip of the filament and the plasma membrane generated by stochastic fluctuations of the length of the filament. As discussed in Chapter 2, actin filaments are easier

bent than compressed, making it likely that bending is the primary source of actin length fluctuations (Mogilner and Oster, 1996). In that case, the speed of protrusion growth  $v_p$  is given by the balance between actin polymerization rate  $k_{\text{on}}$  and depolymerization rate  $k_{\text{off}}$  at the front of the filament, which can be written as (Mogilner and Oster, 1996)

$$v_p = \delta \cos \theta (k_{\text{on}} c_a p(k) - k_{\text{off}}), \quad (3.12)$$

where  $\delta$  denotes the size of an actin monomer,  $\theta$  is the angle between the actin filament and the direction of migration,  $c_a$  is the local concentration of actin monomers in the cytosol and  $p(k)$  is the probability that there is sufficient space between the filament and the membrane, which is given by (Mogilner and Oster, 1996)

$$p(k) = \frac{\int_0^\infty \delta \cos \theta dx e^{-\frac{k(x-x_0)^2}{2}}}{\int_0^\infty dx e^{-\frac{k(x-x_0)^2}{2}}}. \quad (3.13)$$

Here,  $x_0$  is the equilibrium distance between the filament and the membrane and  $k$  denotes the effective spring constant of the actin filament (see Section 2.1).

Eqs. (3.12) and (3.13) suggest that filaments with lower spring constants  $k$  result in higher growth rates. This is however only true if the load that the membrane exerts onto the actin filament does not exceed the buckling force: Buckled filaments can hardly withstand any compressive force (Broedersz and MacKintosh, 2014), strongly decreasing the pressure pushing the membrane forward, which would result in a collapse of the protrusion. Since both the effective spring constant  $k$  as well as the buckling force  $F_b$  decrease with the length of the filament (see Section 2.1), this suggests that the effect of actin crosslinking and branching on protrusion growth depends on the load generated by the membrane: If the load does not exceed the buckling force, crosslinking and branching will be detrimental to protrusion growth. In the case where the load does exceed the buckling force however, crosslinking and branching are essential for protrusion growth as they reduce the unsupported filament length and thus allow the network to sustain larger compressive forces (Mogilner and Oster, 1996; Mogilner and Rubinstein, 2005).

To understand which of the two regimes is relevant in the context of cell migration, we compare typical values of the actin buckling force to membrane generated forces. As discussed in more detail in Section 2.1, the actin buckling force  $F_b$  can be written as (Broedersz and MacKintosh, 2014)

$$F_b = \frac{k_B T l_p \pi^2}{L^2}, \quad (3.14)$$

where  $l_p$  denotes the persistence length of the filament and  $L$  is the unsupported length of the filament. In the absence of crosslinking,  $L$  is simply the length of the filament. Here, we used Eq. (2.7) together with the fact that the bending modulus  $\kappa$  can be expressed in terms of the persistence length as  $\kappa = l_p k_B T$  (Broedersz and MacKintosh, 2014). Cells show a broad distribution in actin filament lengths up to  $\sim 15 \mu\text{m}$  (Small *et al.*, 1995; Svitkina *et al.*, 1997) (look for another source) and form actin driven protrusions (lamellipodia and filopodia) up to the length of tens of micrometers (Brückner, Schmitt,

*et al.*, 2022; Caballero, Voituriez, *et al.*, 2014; S. Cheng *et al.*, 2002). According to Eq. (3.14), supporting a protrusion of a length of 10  $\mu\text{m}$  without crosslinking would limit the compressive forces applied onto an actin filament by the membrane to  $F_b \approx 4 \times 10^{-3}$  pN at a temperature of  $T = 300$  K and with  $l_p = 10$   $\mu\text{m}$  (Milo *et al.*, 2016). To estimate the corresponding membrane force, we consider the Laplace pressure generated in a lamellipodium  $P = \tau(R_1^{-1} + R_2^{-1})$ , where  $R_1$  and  $R_2$  denote the two principle radii of curvature. Since the height  $h$  of a lamellipodium ( $\sim 150$  nm (Laurent *et al.*, 2005)) is significantly smaller than its width (tens of micrometers (Brückner, Schmitt, *et al.*, 2022)), we can approximate the Laplace pressure as  $P \approx \tau/h$ . Together with a surface tension of the order of 300 pN/ $\mu\text{m}$  (Lieber *et al.*, 2013) and a minimal membrane area per actin filament of about 50 nm<sup>2</sup> (filament diameter 6 nm (Milo *et al.*, 2016)), this yields a minimal membrane force per actin filament of 0.1 pN, which is orders of magnitude above the buckling force of a 10  $\mu\text{m}$  long actin filament. As a consequence, the maximal protrusion length that could be supported in the absence of branching, crosslinking and bundling would be around 2  $\mu\text{m}$  (see Eq. (3.14)), clearly indicating that within cells, the formation of interconnected actin networks or bundles is essential to protrusion growth, in agreement with the observation of connected networks and tight bundles in lamellipodia and filopodia respectively (Blanchoin *et al.*, 2014; Faix *et al.*, 2006; Medalia *et al.*, 2002) even though it is debated if the network structure in lamellipodia is primarily due to branching or crosslinking (Higgs, 2011; Medalia *et al.*, 2002; Urban *et al.*, 2010).

While the physics of actin bundles and filopodia growth were extensively studied elsewhere (Heussinger *et al.*, 2007; Mogilner and Rubinstein, 2005), here we focus on lamellipodium growth and thus the case of crosslinked and branched networks. As discussed above, the growth of lamellipodia involves the activation of Arp2/3, which plays a crucial role in determining the resulting actin structure, (see Pollard, Blanchoin, *et al.*, 2000; Pollard and Borisy, 2003 for comprehensive reviews): The WAVE regulatory complex that is activated at the front of the protrusion combines the assembled Arp2/3 complex with actin monomers that are integrated in an existing filament, resulting in the binding of Arp2/3 to the side of the filament (Mullins *et al.*, 1998; Pantaloni *et al.*, 2000). Upon binding to actin, Arp2/3 initiates the nucleation of new actin filaments whose pointed end is capped by the Arp2/3 complex. This creates a rigid connection between the preexisting filament and the newly formed filament that is characterized by a 70° branching angle. As a consequence, actin filament orientations are distributed over a broad range of angles with peaks at  $\pm 35^\circ$  (Maly *et al.*, 2001) and the majority of filaments being oriented with their barbed ends towards the front of the protrusion (Small *et al.*, 1995; Svitkina *et al.*, 1997). Note that in principle the Arp2/3 induced branching leads to an explosion of free filament ends, which represent binding sites for globular actin in the cytosol (Pollard and Borisy, 2003). To avoid complete depletion of globular actin in the cytosol and thus retain filament growth, capping proteins bind to barbed ends in the branched network, terminating further growth and thus limiting the total number of growing filaments (Wear *et al.*, 2004; Weeds *et al.*, 1993). Additionally, further away from the front of the protrusion, actin depolymerization occurs at an accelerated rate, supplying new actin monomers that can be integrated at the front of the protrusion (Pollard and Borisy, 2003). Apart from branching, crosslinkers lead to additional mechanical connections

between actin filaments (Blanchoin *et al.*, 2014). Together with filament capping, this results in mesh sizes in cells of about 30 nm (Bovellan *et al.*, 2014), strongly increasing the buckling force to about 0.6 nN (see Eq. (3.14)). The importance of this reduced mesh size and thus increased buckling force can be seen by the fact that cells that lack the crosslinker filamin display unstable protrusions (Cunningham *et al.*, 1992). Additionally, branched actin networks were found to increase in stiffness as they grow under load, which is thought to be caused by a tighter packing of actin due to filament bending, causing an increase of the branching angle (Bieling *et al.*, 2016).

Apart from increasing the mechanical support of actin filaments, branching has another positive effect on actin polymerization compared to the growth of filopodia and individual actin filaments: Branching induces a tilt of the filaments relative to the membrane. This tilt leads to larger gaps between the filament tip and the membrane as the filament bends due to thermal fluctuations (Mogilner and Oster, 1996; Mogilner and Rubinstein, 2005). Hence, this results in a faster filament growth compared to actin filaments that approach the membrane from a 90° angle (see Eq. (3.12)) and allows growth against higher membrane forces. Taken together, both the increased concentration of actin monomers in the cytosol in the absence of RhoA at the leading edge as well as the mechanical support through branching induced by Rac1 result in a coupling between the degree of cell polarization and protrusion growth, which makes cell polarity a key dynamical parameter for protrusion growth and cell migration (Krause and Gautreau, 2014).

Besides polymerization rate and filament stiffness, also membrane tension is an important factor controlling protrusion growth as growth is driven by actin pushing against the plasma membrane (Mogilner and Oster, 1996). Following the picture of the polymerization ratchet, the membrane tension induces a flow of actin away from the membrane towards the cell body. The net growth rate of the protrusion is then given by the balance between the polymerization velocity and the actin retrograde flow (Sens, 2020). Hence, higher membrane tension should result in slower protrusion growth. On the other hand, there is recent evidence for a positive feedback between retrograde flow and cell polarization, which could increase polymerization rate and thus protrusion growth at the front of the cell (Maiuri *et al.*, 2015). Additionally, increases in membrane tension during protrusion growth can inhibit the formation of competing protrusions further stabilizing the leading protrusion (Houk *et al.*, 2012). Taken together, these results highlight membrane tension as a key parameter controlling protrusion growth that couples in a non-trivial way to cell polarity.

### Adhesion structure and dynamics

Protrusion growth and thus cell migration as a whole relies on a mechanical coupling between the actin cytoskeleton and the substrate. In mesenchymal cell migration, this is realized through integrin based adhesions. These can take the form of matured focal adhesions that are connected to actin stress fibers, as introduced above, but also smaller, less mature adhesion complexes can be sufficient for migration (Burrige, 2017). In particular, migrating cells in their native, compliant, three dimensional environment display less focal adhesions and associated stress fibers compared to cells migrating on stiff, two dimensional plastic or glass substrates commonly used in cell migration exper-

iments (Burrige and Guilly, 2016). As a consequence, models that describe two dimensional migration on stiff substrates might exaggerate the role of focal adhesions for cell migration in physiological conditions. However, focal adhesions allow us to introduce the key components and concepts underlying integrin-based adhesion. For this, we briefly describe the structure and dynamics of integrin-based adhesion complexes during cell migration and discuss their interaction with other components of the migration machinery, specifically actin polymerization, myosin contractility, and cell polarity.

Essential for any adhesion complex that connects the cellular cytoskeleton to the substrate are transmembrane proteins. The most prominent group of such transmembrane proteins involved in mesenchymal cell migration are integrins (S. H. Lo, 2006). Integrins need to be mechanically linked to actin structures to allow force transmission to the substrate. In focal adhesions however, even though direct interactions between actin and integrin are possible (Van Der Flier *et al.*, 2001), there is a spatial separation between integrins and actin (Kanchanawong *et al.*, 2010), such that direct force transmission is not possible. This gap is bridged by the linker protein talin, which has binding sites for both actin and integrins (Critchley, 2009). Talin binding to integrin further induces a conformational change of integrin, which increases its affinity for possible extracellular binding partners (Shattil *et al.*, 2010). Consequently, focal adhesions are organized in a layered structure with integrins at the bottom with a narrow layer of proteins involved in signaling on top. Then follows the force transduction layer containing talin that is linked to actin structures in the highest layer (Kanchanawong *et al.*, 2010). This layered structure with a number of different molecular components allows cells to sense and adapt their adhesive properties to the mechanical tension transmitted through their adhesions.

The force-adaptation of cellular adhesions emerges from the interplay of different mechanosensitive adhesion molecules. For example, integrins behave as catch-bonds with a peak lifetime at a load of about 30 pN when bound to fibronectin (Kong *et al.*, 2009) while talin exposes cryptic binding sites upon stretching, which allows binding of other molecules of the adhesion complex either involved in signaling or reinforcing the connection to the actin cytoskeleton (Ciobanasu *et al.*, 2014; Menkel *et al.*, 1994; Yan *et al.*, 2015). Even though the molecular details behind the force-adaptation of adhesion complexes are only partly known, this results in an overall integrin recruitment and adhesion growth under tension, which is essential for focal adhesion maturation (Burrige and Guilly, 2016).

During migration, an asymmetry in focal adhesion assembly and disassembly needs to be sustained by the cell to allow for protrusion growth at the front of the cell and adhesion detachment at the rear (Broussard *et al.*, 2008). To do so, cells utilize a combination of mechanical and chemical signaling to control adhesion formation and detachment. In the cell rear, focal adhesions are essential to inhibit complete rear retraction and retain a spreaded morphology during migration (Wehrle-Haller, 2012), which is supported by RhoA induced contractility. On the other hand, adhesions must disengage with the substrate to allow a translocation of the cell. This is also driven by myosin contractility in the form of stress fibre contractions (Broussard *et al.*, 2008). Due to the catch-bond nature of the adhesion bonds, this requires however a previous destabilization of the focal adhesions to avoid cell rupture Kirfel

*et al.*, 2004). At the cell front, cells initially form transient, so-called nascent adhesions near the cell membrane. This process relies on Rac1 and Cdc42 activity (Nobes *et al.*, 1995) and could be supported by the retrograde flow by engaging the catch-bond property of integrins (Wehrle-Haller, 2012). Interestingly, this process does however not rely on myosin contractility (Choi *et al.*, 2008), which only comes into play as these transient adhesions mature into more stable focal adhesions (Burridge and Guilluy, 2016; Rivelino *et al.*, 2001). Over time, the contractile forces move the focal adhesions towards the cell body, where they largely disassemble (Digman *et al.*, 2008; Rid *et al.*, 2005; Wehrle-Haller, 2002). Overall, adhesions represent a mechanical anchor for the actin cytoskeleton that supports actomyosin-driven contractility and inhibits retrograde flow thus allowing protrusion growth.

The role of adhesion complexes during cell migration is conceptualized in the *molecular clutch* model (Chan *et al.*, 2008). There, the mechanical coupling between the actin cytoskeleton and the substrate is modeled as an elastic spring that is permanently attached to the substrate and can bind to and unbind from actin filaments with rates  $k_{\text{on}}$  and  $k_{\text{off}}$ , respectively. As the actin moves towards the cell body with the retrograde flow velocity  $v_r$ , bound elastic springs get stretched until they unbind from the actin filament. The rate with which the stretching occurs depends on the compliance of the substrate, with slower loading on softer substrates. The unbinding rate  $k_{\text{off}}$  and thus the average extension of a bound spring generally depends on the load on the bond and either decrease (slip-bonds) or increase (catch-bonds) with increased stretching. The interactions between adhesion bonds and actin filaments either give rise to a constant, friction like force or oscillatory loading and failure, depending on the substrate stiffness (Chan *et al.*, 2008) and the binding and unbinding rates (Sens, 2020). This then gives rise to different migration morphologies. To capture more detailed aspects of how substrate stiffness modifies the friction between the actin retrograde flow and the substrate, more detailed effects, such as load-dependent talin unfolding and consequent adhesion reinforcement, can be easily integrated in this simple framework (Elosegui-Artola, Oria, *et al.*, 2016). Overall, the frictionlike effect of adhesion binding and unbinding makes adhesion complexes an essential component of the cellular migration machinery as they allow both, adhesion expansion as well as rear retraction in a polarization dependent manner.

### 3.3 A general, bottom-up model for confined cell migration

It is astounding that despite the immense molecular complexity of the migration machinery, the emergent migration behavior can be captured in a simple conceptual picture such as the four-step process and relatively simple phenomenological and data driven models (Brückner and Broedersz, 2023; Caballero, Comelles, *et al.*, 2015). This difference between molecular and behavioral complexity did however result in the paradoxical situation that despite the extensive knowledge of the cell migration process that is based on more than a century of research, there is a substantial fragmentation when it comes to modeling approaches (Danuser *et al.*, 2013; Edelstein-Keshet *et al.*, 2013). This is partially driven by the amount of information that is available in the

field, which allows for a myriad of modeling approaches on many different levels of detail, ranging from microscopic models for subcellular processes (Danuser *et al.*, 2013) to coarse-grained models which treat cells effectively as point particles (Selmeczi, Li, *et al.*, 2008). All of these approaches made important contributions to the field. Nonetheless, both approaches come with their own limitations: Models that describe detailed molecular dynamics are difficult to constrain from migration data due to the large number of parameters that these models consist of. Models that do acknowledge the emergent character of cell migration however rely typically on phenomenological or data-driven approaches (Brückner and Broedersz, 2023; Selmeczi, Li, *et al.*, 2008). As a consequence, these models are typically not generalizable and are unable to predict the effect of different cellular environments, drug treatments, or differences between different cell lines on the observed migration behavior, resulting in different models for each substrate or cell line (see Section 3.1). Thus, a modeling approach that is able to connect the simple, emergent migration behavior to the underlying molecular processes is needed.

Due to the extensive characterization of the migration behavior on two-state patterns that was previously done in our group (Brückner, Fink, Schreiber, *et al.*, 2019; Brückner, Schmitt, *et al.*, 2022; Brückner, Fink, Rädler, *et al.*, 2020), these represent an ideal system to attempt connecting a bottom-up model to top-down models before subsequently generalizing our model to other substrates. From (Brückner, Schmitt, *et al.*, 2022), it is apparent that protrusion-growth plays an essential role in the interaction of the cell with its microenvironment, guiding the overall migration behavior. Guided by that observation and in line with the four-step process discussed above, our model focuses on actin polymerization against the cell membrane and the consequent retrograde flow, adhesion bonds with the substrate, the contractile link between protrusion and nucleus, and the interplay between actin polymerization and cell polarity (Fig. 3.6). To construct such a model, we build on existing models for one-dimensional mesenchymal migration with protrusions on both sides of the nucleus (Lavi *et al.*, 2016; Ron *et al.*, 2020; Sens, 2020). These models treat the mechanical coupling between nucleus and protrusion however only heuristically by introducing an elastic coupling between nucleus and protrusion that was attributed to the effective material properties of cells. The force acting onto the nucleus did thus only depend on the length of the protrusion, while other factors of the cellular microenvironment were not accounted for. As a consequence, they are not directly applicable to describe cell migration on substrates with a more complex two-dimensional geometry. To generalize these models to arbitrary geometries, we thus start by deriving an expression for the protrusion force in terms of the protrusion's dimensions that are determined by the geometry and the adhesive properties of the substrate.

In the protrusion, membrane tension (membrane force  $f_\tau$ ) generates a retrograde flow (velocity  $v_r$ ) of actin towards the cell body that is reinforced by myosin contractility (force  $f_c$ ) in the crossover region between protrusion and cell body (see Section 3.2). The sum of membrane and contractile forces is balanced by the viscous drag of actin filaments in the cytosol (drag coefficient  $\zeta_0^a$ ) and the adhesion force  $f_{\text{ad}}$  that arises from the binding kinetics of adhesion bonds to the actin filaments (Fig. 3.6A), such that

$$\zeta_0^a v_r + f_{\text{ad}} = f_c + f_\tau. \quad (3.15)$$

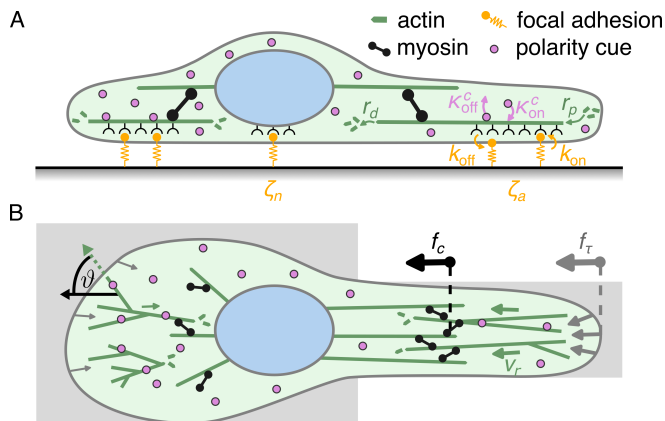


Figure 3.6: **Components of the migration model** (taken from Flommersfeld *et al.*, 2023). **A.** Side view with key molecular components. The stochastic (un)binding of adhesion molecules with rates  $k_{\text{on/off}}$  gives rise to effective friction coefficients of protrusion ( $\zeta_a$ ) and nucleus ( $\zeta_n$ ). Actin polymerizes at the edge of the protrusions (rate  $r_p$ ) and depolymerizes near the nucleus (rate  $r_d$ ). Polarity cues transiently bind to actin with rates  $\kappa_{\text{on}}^c$  and  $\kappa_{\text{off}}^c$ . **B.** Top view on unisotropic substrate. The retrograde flow (velocity  $v_r$ ) is driven by myosin contractility ( $f_c$ ) and membrane forces ( $f_\tau$ ). Confinement-induced actin alignment (angle  $\theta$ ) stimulates protrusion growth, resulting in increased membrane tension and retrograde flow.

The force that is exerted by the adhesion bonds in the protrusion is given by  $f_{\text{ad}} = \rho_b \langle n f_b \rangle \ell_r w_p$ , where  $\rho_b$  is the total surface density of bonds,  $n$  is the fraction of bound bonds,  $f_b$  is the force per bond,  $w_p$  is the width of the protrusion and  $\ell_r$  is the region at the front of the protrusion over which the retrograde flow is concentrated. Following Sens, 2020, we approximate  $\langle n f_b \rangle \approx n \langle f_b \rangle$  and use  $\langle f_b \rangle = k_b v_r / k_{\text{off}}(f_b)$ , which leads to

$$f_{\text{ad}} = \frac{\rho_b \ell_r k_b n \langle f_b \rangle w_p}{k_{\text{off}}(f_b)} v_r = \zeta_1^a(f_b) v_r, \quad (3.16)$$

where  $k_b$  is the effective spring constant associated with adhesive bonds and  $k_{\text{off}}(f_b)$  denotes the bond's (load-dependent) unbinding rate. Overall, the collective binding and unbinding dynamics of the adhesion bonds result in an effective friction force. We can thus rewrite Eq. (3.15) as

$$\zeta_a v_r = f_c + f_\tau, \quad (3.17)$$

with  $\zeta_a = \zeta_0^a + \zeta_1^a(f_b)$ .

To find the myosin generated contractile force, we build up on our discussion of actomyosin contractility inside cells in Section 3.2: Myosin generates a contractile force by traversing counter-oriented actin filaments inside the network in the crossover region between protrusion and cell body and the overall contractility is determined by the number of actin filaments associated with both the nucleus and the protrusion. While we have no reason to believe that the number of nucleus-associated filaments is sensitive to the cellular environment, the number of protrusion-associated filaments in the crossover region is

determined by the influx of new actin filaments due to the retrograde flow and the depolymerization rate  $r_d$ . The total rate of influx of actin from a protrusion of width  $w_p$  is then given by  $\rho_b w_p \ell_r \langle N_b \rangle^{-1} v_r / \ell_a$ , where  $\langle N_b \rangle$  denotes the average number of adhesion bonds per actin filament and  $\ell_a$  is the size of an actin monomer. The prefactor  $\rho_b w_p \ell_r / \langle N_b \rangle$  accounts for the fact that protrusion associated actin needs to be mechanically connected to the substrate to support force transmission between the front of the protrusion and the nucleus. In the crossover region, we expect the retrograde flow to cease, making depolymerization the main driver of actin filament loss in the contractile region. The total number of protrusion-associated actin filaments in the crossover region at steady state is thus given by

$$N_F^p(v_r) = \frac{v_r \rho_b w_p \ell_r}{r_d \ell_a \langle N_b \rangle}. \quad (3.18)$$

Together with the number of antiparallel oriented, nucleus-associated filaments  $N_F^n$  and the total number of myosin motors  $r_m \rho_m$ , where  $r_m$  denotes the myosin interaction radius and  $\rho_m$  is the myosin line density, we can then write the number of contractile actomyosin configurations  $N_{\text{am}}$  as

$$N_{\text{am}} = n_{\parallel} r_m \rho_m N_F^n N_F^p(v_r) = \tilde{N}_F \rho_b \rho_m w_p v_r, \quad (3.19)$$

where  $n_{\parallel}$  denotes the fraction of incoming actin filaments oriented parallel to the nucleus-protrusion axis and we introduced the geometry-independent parameter  $\tilde{N}_F = n_{\parallel} N_F^n r_m \ell_r / (\ell_a r_d \langle N_b \rangle)$ . The total contractile force is then simply given by

$$f_c = \tilde{N}_F \rho_b w_p \rho_m f_m v_r = \frac{\tilde{N}_F \rho_b \rho_m w_p f_m}{\zeta_a - \tilde{N}_F \rho_b \rho_m w_p f_m} f_{\tau}, \quad (3.20)$$

where  $f_m$  denotes the force generated by an individual myosin filament. Physically, larger membrane forces increase the retrograde flow, which elevates the actin density in the crossover region resulting in an increasing contractility (Figs. 3.6B).

This leads to a coupling between myosin contractility and the membrane force. Hence, to find an expression for the contractile force in terms of the protrusion dimensions, we require an expression for the membrane force  $f_{\tau}$ . For this, we consider the formation of a protrusion of length  $L_p$ , height  $h_p$ , and width  $w_p \gg h_p$  (Laurent *et al.*, 2005; Shahapure *et al.*, 2010). The resulting increase in surface area is opposed by the membrane force  $f_{\tau} = 2(h_p + w_p)\tau \approx 2w_p\tau$ . Interestingly, for constant surface tension  $\tau$  the contractile force is independent of protrusion length (Eq. (3.20)), which is incompatible with protrusion-guided migration and in particular the data driven model in Brückner, Schmitt, *et al.*, 2022. The surface tension of cells can however vary with surface area (Gauthier *et al.*, 2011; Houk *et al.*, 2012; Roffay *et al.*, 2021) for which we account by introducing an area dependence of the membrane tension, resulting in  $\tau = \tau_0 + 2\tau_1 L_p / h_p$ , with parameters  $\tau_0$  and  $\tau_1$ . The membrane force is then

$$f_{\tau} = 2w_p\tau_0 + \frac{4\tau_1}{h_p} w_p L_p. \quad (3.21)$$

The first term is due to the baseline membrane tension, which should be balanced by the internal cytosolic pressure, such that only the second term contributes to the mechanical coupling between nucleus and protrusion in terms

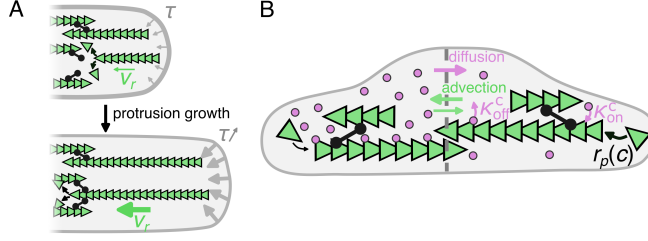


Figure 3.7: **Effect of the retrograde flow on the overall contractility and polarization.** **A.** The retrograde flow velocity  $v_r$  determines the actin concentration in the crossover region and thus the contractile force. Protrusion growth leads to an increase in membrane tension  $\tau$  and thus retrograde flow, resulting in an increased contractility further increasing the retrograde flow. **B.** The retrograde flow advects a polarity cue that can bind to and unbind from actin with rates  $\kappa_{\text{on}}^c$  and  $\kappa_{\text{off}}^c$ , respectively. If strong enough, this leads in an accumulation of polarity cue in the shorter side of the cell, where it inhibits actin polymerization, resulting in a reinforcement of cell polarity that is countered by diffusion of the polarity cue.

of the contractile force (Eq. (3.20))

$$f_c = \frac{4\tau_1 \tilde{N}_F \rho_b \rho_m w_p f_m}{(\zeta_a - \tilde{N}_F \rho_b \rho_m w_p f_m) h_p} w_p L_p = k_c L_p. \quad (3.22)$$

In general, the effective spring constant  $k_c$  depends on the the contractile force itself through the myosin load-velocity relation (Howard, 2005b) and the mechanosensitivity of the adhesion bonds. Considering that the typical nuclear velocities found during mesenchymal cell migration ( $< 30\text{nm/s}$  (B. Amiri *et al.*, 2023; Brückner, Fink, Schreiber, *et al.*, 2019; Gupton *et al.*, 2006)) are at least an order of magnitude below the unloaded myosin velocity ( $200 - 800\text{nm/s}$  (Howard, 2005c)), it appears however reasonable to approximate the force generated per myosin filament  $f_m$  by the myosin stall force  $f_s$ . Further, Brückner, Schmitt, *et al.*, 2022 found that a non-linear coupling between nucleus and protrusion did not significantly improve the agreement with experimental data. This suggests that in our case also the mechanosensitivity of the adhesion bonds can be neglected for a model that describes the population averaged migration behavior, such that we use  $n = n_0$  and  $k_{\text{off}} = k_{\text{off}}^0$  in the expression for  $\zeta_a$ . Finally, we expect the focal adhesions are the dominant contribution to  $\zeta_a$  due to the importance of focal adhesions for the formation of intact lamellipodia (Damiano-Guercio *et al.*, 2020) and thus neglect the viscous contribution  $\zeta_0^a$ , such that overall  $\zeta_a \approx \zeta_1^a(0)$  (a more detailed discussion of the effect of a force dependence of  $k_c$  can be found in (Flommersfeld *et al.*, 2023)). This leaves us with a linear elastic coupling between nucleus and protrusion, which has been assumed in several migration models (Brückner, Schmitt, *et al.*, 2022; Ron *et al.*, 2020; Sens, 2020). In our model, this elastic coupling emerges from the interplay between increased membrane tension, retrograde flow, and myosin contractility (Fig. 3.7A).

This result, together with Eq. (3.17) allows us to express the retrograde

flow velocity in terms of the protrusion dimensions and since the velocity of the front of the protrusion is given by the difference between the (projected) polymerization velocity and the retrograde flow velocity, the velocity left/right protrusion is given in terms of its position  $x_{\ell/r}$  as

$$\dot{x}_{\ell/r} = -\frac{k_{\ell/r}(x_{\ell/r})}{\zeta_a(x_{\ell/r})}(x_{\ell/r} - x_n) \mp \ell_a S_{\ell/r} r_p(x_{\ell/r}), \quad (3.23)$$

where we substituted  $L_p = x_{\ell/r} - x_n$ , introduced the order parameter  $S_{\ell/r} = \langle |\cos(\vartheta_{\ell/r})| \rangle$  that measures the average orientation of actin filaments (Fig. 3.6B), and  $k_{\ell/r}(x_{\ell/r}) = k_c(x_{\ell/r}) + 4\tau_1 w_p(x_{\ell/r})/h_p$ . The protrusion dynamics then determine the nuclear dynamics through the balance of the two protrusion forces (Eq. (3.22))

$$\dot{x}_n = \frac{k_c(x_\ell)}{\zeta_n(x_n)}(x_\ell - x_n) + \frac{k_c(x_r)}{\zeta_n(x_n)}(x_r - x_n). \quad (3.24)$$

Where the nuclear friction coefficient  $\zeta_n$  is defined analogously to the friction experienced by the actin retrograde flow as  $\zeta_n = \zeta_0^n + \zeta_1^n(0)$ , with  $\zeta_1^n(0) = \rho_b \ell_n k_b n_0 w_n / k_{\text{off}}^0$ . Since the nucleus is much larger than the actin filaments, it is less clear if the internal friction can be neglected. Hence, we account for both contributions in the expression for  $\zeta_n$ .

To be able to evaluate Eq. (3.23) we require an expression for the polymerization rate  $r_p$ , which depends on the local concentration of certain polarity cues (Rappel *et al.*, 2017). Following previous work (Lavi *et al.*, 2016; Maiuri *et al.*, 2015), we account for this process by considering a generic back-polarity cue that can be advected by the actin retrograde flow and inhibits actin polymerization (Fig. 3.7B). Beyond those two requirements our model does not rely on other, specific properties of the polarity cue. Hence, there are a number of different biological candidates for such a polarity cue. The best supported and most natural candidate would be myosin II, other proteins can however also not be excluded such as RhoA (see Flommersfeld *et al.*, 2023 for a more detailed discussion). Here, we thus stick to the notion of an abstract polarity cue that could either have a direct biological correspondent or could summarize the effect of a number of different polarity markers.

Since the polymerization rate depends on the local polarity cue concentration  $c$ , we first need to analyze the dynamics of  $c$  in the two protrusions. For that, we consider the difference in the average concentration between the two halves of the cell  $\Delta c = c_r - c_\ell$ , where  $c_{\ell/r}$  is the concentration to the left/right of the nucleus. The polarity cue binds to and unbinds from actin filaments with rates  $\kappa_{\text{on}}^c$  and  $\kappa_{\text{off}}^c$  and is thus advected with the retrograde flow. The advective flux between the two parts of the cell is then  $\Delta v_r n_c c_0$ , where  $\Delta v_r = v_r(x_r) - v_r(x_\ell)$ ,  $n_c = \kappa_{\text{on}}^c / (\kappa_{\text{on}}^c + \kappa_{\text{off}}^c)$  is the bound fraction of polarity cue, and  $c_0$  is the average cue concentration in the cell. Together with diffusion of the polarity cue in the cytosol, the flux between the two cell parts is then

$$J(x, t) = -(1 - n_c) \tilde{D} \partial_x c(x, t) - \Delta v_r n_c c_0 + \tilde{\sigma} \xi(t), \quad (3.25)$$

with the diffusion constant  $\tilde{D}$ . Guided by the structure of the data-driven model in Brückner, Schmitt, *et al.*, 2022, we assume that the polarity to be the dominating source of noise in our model. We account for this through the Gaussian white noise  $\xi(t)$  of strength  $\tilde{\sigma}$ . To simplify the treatment of

the polarity cue and since we are only interested in the average concentration difference between the two sides of the cell. To obtain the flux through the center plane of the cell  $J_0(\Delta c, t)$ , we approximate  $\partial_x c \approx \Delta c/L_c$ , which leads to

$$J_0(\Delta c, t) \approx -(1 - n_c)\tilde{D}L_c^{-1}\Delta c - n_c c_0 \Delta v_r + \tilde{\sigma}\xi(t). \quad (3.26)$$

To find an equation for the dynamics of the local polarity cue concentration, we use the continuity equation

$$\frac{\partial c(x, t)}{\partial t} = -\frac{\partial J_0(x, t)}{\partial x}, \quad (3.27)$$

which, together with no-flux boundary conditions at the front of the protrusions, describes the concentration profile along the entire long axis of the cell. Due to the boundary conditions, the only flux of polarity cue in or out of the two halves of the cell is through the midplane (Fig. 3.7). The flux for each half of the cell then gives

$$\frac{\partial c_r(t)}{\partial t} \approx -\frac{0 - J_0}{L_c/2} = 2L_c^{-1}J_0 \quad (3.28)$$

and

$$\frac{\partial c_\ell(t)}{\partial t} \approx -\frac{J_0 - 0}{L_c/2} = -2L_c^{-1}J_0. \quad (3.29)$$

Using  $\Delta c = c_r - c_\ell$ , we then get an approximate expression for the dynamics of  $\Delta c$  in a cell with no-flux boundary conditions

$$\frac{\partial \Delta c}{\partial t} \approx \frac{4J_0(\Delta c, t)}{L_c} \approx -D\Delta c(t) - \frac{4n_c c_0}{L_c}\Delta v_r(\Delta c) + \frac{4\tilde{\sigma}}{L_c}\xi(t), \quad (3.30)$$

with  $D = 4(1 - n_c)\tilde{D}L_c^{-2}$ .

To express Eq. (3.30) in terms of the actin organization in the protrusion, we note that at steady state, the retrograde flow equals the projected polymerization velocity (see Eq. (3.23)), such that  $\Delta v_r(\Delta c) = \ell_a S_r r_p(x_r) - \ell_a S_\ell r_p(x_\ell)$ . To find a leading order description of the dynamics of  $\Delta c$ , we then split  $r_p$  in an even ( $r_p'$ ) and an odd ( $r_p''$ ) part in  $\Delta c$ . Together with  $c(x_{\ell/r}) = c_0 \mp \Delta c(t)/2$ , we then get

$$\Delta v_r(\Delta c) = \ell_a r_p'(\Delta c)(S_r - S_\ell) + \ell_a r_p''(\Delta c)(S_r + S_\ell). \quad (3.31)$$

The even term in  $\Delta c$  acts as a bias, which dilutes the side of the cell in which the actin filaments are more aligned with the direction of migration. Due to this simple effect on the concentration dynamics, we do not expect the detailed functional dependence of  $r_p'$  to play a qualitative role and thus only keep the leading order term, such that  $r_p' \approx r_p(c_0)$ . The odd term, however, will either oppose or reinforce the concentration gradient depending on its sign. Since we assume that the back-polarity cue inhibits actin polymerization and thus retrograde flow, we expect the odd term reinforces the concentration gradient to leading order. To ensure that  $\Delta c$  remains bound, we expand  $r_p''$  up to third order, such that  $r_p''(\Delta c) \approx -r_1 \Delta c + r_3 \Delta c^3$ , with  $r_{1/3} > 0$ . From this we get

$$\Delta v_r(\Delta c) = \ell_a r_p(c_0)(S_r - S_\ell) - \ell_a r_1(S_r + S_\ell)\Delta c + \ell_a r_3(S_r + S_\ell)\Delta c^3 \quad (3.32)$$

To align our notation with Brückner, Schmitt, *et al.*, 2022, we introduce the polarization  $P(t) \equiv -P_0\Delta c(t)$ , which is determined by

$$\dot{P} = -\alpha P - \beta P^3 + \delta(S_r - S_\ell) + \sigma\xi(t), \quad (3.33)$$

with  $\sigma = -4P_0\tilde{\sigma}L_c^{-1}$ ,  $\delta = 4P_0n_c c_0 L_c^{-1}\ell_a r_p(c_0)$ ,  $\alpha = D - 4n_c c_0 L_c^{-1}\ell_a r_1(S_r + S_\ell)$ , and  $\beta = 4P_0^{-2}n_c c_0 L_c^{-1}\ell_a r_3(S_r + S_\ell)$ . To couple Eq. (3.33) to Eq. (3.23), we account for the leading order effect of the polarity on the polymerization rate through  $r_p(t) = r_p(c_0) + r_1 P_0^{-1} P(t)$ . The resulting mechanistic model given by the closed set of Equations (3.23), (3.24), and (3.33) describing protrusion-driven 1D cell migration is illustrated in Fig. 3.8.

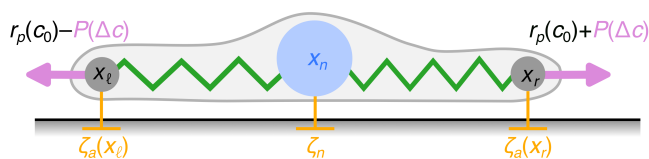


Figure 3.8: **Schematic representation of the model.** The two protrusion coordinates are driven by polarization dependent polymerization rate  $r_p(P)$  and are connected to the nucleus through linear elastic springs. Both the protrusion coordinate and the nuclear coordinate are subject to a friction force that accounts for the interactions with the substrate and in the case of the nucleus with the cytosol.

### 3.4 Migration and decision making in lateral confinement

In the following, we will apply this general model to migration on concrete substrates for which further specification of the dependence of model parameters on the substrate's physical properties and geometry is needed. To do this, we utilize both bottom-up considerations and insights that were obtained from top-down models when available.

For this, we start with cells migrating on dumbbell shaped two-state patterns, where the cells are exposed to lateral confinement as they migrate from one island to the other (Fig. 3.1D). This system was previously analyzed extensively in our group and multiple data-driven models were developed for it (Brückner, Fink, Schreiber, *et al.*, 2019; Brückner, Schmitt, *et al.*, 2022). A key insight of these studies was that confinement stimulates protrusion growth and cell polarization resulting in an overall acceleration of the cell. A mechanistic explanation for this phenomenon on the molecular level is however still lacking. We start by proposing such a mechanism and show that the data-driven models can be re-derived from our bottom-up model. In contrast to the models in (Brückner, Fink, Schreiber, *et al.*, 2019; Brückner, Schmitt, *et al.*, 2022) the bottom-up model can however be generalized more easily to other geometries, which we demonstrate by applying it to a chain of square-shaped islands that are connected by bridges of varying width. In this geometry, cells on an island can choose between two channels of different width. We analyze how the cellular decision making depends on the pattern widths as well as on

different model parameters that characterize the adhesiveness of the pattern as well as the contractility and polarity of the cell.

### Bridging the gap to data-driven models on two-state patterns

We account for the geometry of the two-state pattern in our model by noting that the actin organization is a key determinant of protrusion growth and cell polarity in Eqs. (3.23) and (3.33) through the order parameter  $S_{\ell/r}$ . In the absence of confinement, actin branching (Mullins *et al.*, 1998) and random fluctuations lead to a range of filament orientations (Small *et al.*, 1995; Svitkina *et al.*, 1997). In confinement however, we expect the distribution of orientations to be reduced (Fig. 3.9A), either through direct geometric constraints for filaments longer than the pattern width or through propagation of a preferred orientation over a correlation length scale from the edge of the confined protrusion into the bulk through alignment interactions, as in liquid crystals (Fürthauer *et al.*, 2019; Lee *et al.*, 1971; Saintillan *et al.*, 2013).

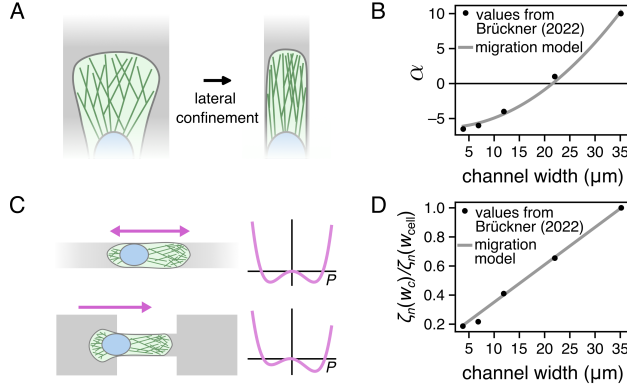


Figure 3.9: **Cell migration in lateral confinement** (adapted from Flombersfeld *et al.*, 2023). **A.** Lateral confinement of the protrusion leads to actin filament alignment. **B.** Fit of the analytic expression for  $\alpha$  on dumbbell-shaped patterns to the values reported in Brückner, Schmitt, *et al.*, 2022. **C.** Lateral confinement induces spontaneous polarization of the cell. For homogeneous confinement (upper), both polarization directions are equally likely. For asymmetric confinement (lower), polarization is biased in the direction of stronger confinement. **D.** Fit of the analytic expression for  $\zeta_n(w_c)/\zeta_n(w_{\text{cell}})$  on dumbbell-shaped patterns to the values reported in Brückner, Schmitt, *et al.*, 2022.

To account for such boundary-induced alignment, we assume that the order parameter  $S$  increases with confinement as  $S = 1 - sw_p^2$ , where  $s > 0$  accounts for the strength of actin alignment interactions. From this we find an analytic expression for  $\alpha$  (Eq. (3.33)) as a function of protrusion width:

$$\alpha(w_{p,\ell}, w_{p,r}) = D - 4n_c c_0 L_c^{-1} l_a r_1 (2 - sw_{p,r}^2 - sw_{p,\ell}^2). \quad (3.34)$$

This expression presents a mechanistic explanation for the geometry-adaptation phenomenon found in Brückner, Schmitt, *et al.*, 2022: With increasing confinement  $\alpha$  becomes negative, inducing a self-reinforcement of the polarity and

consequently protrusion growth. This qualitative change arises from the competition between advection and diffusion that is summarized by the right hand side of Eq. (3.34). In the absence of confinement, actin polymerization is less directed, resulting in slower protrusion growth and a lower retrograde flow such that diffusion in the cytosol is fast enough to dominate the advection of the polarity cue. In confinement however, the increased actin alignment results in faster protrusion growth and thus faster retrograde flow, which leads to a reinforcement of the polarity. To test if the channel width dependence in Eq. (3.34) agrees qualitatively with the channel width dependence of  $\alpha$  found from fitting experimental data, we fit  $\alpha(w_{\text{cell}}, w_c)$  for an unconfined cell (width  $w_{\text{cell}}$ ) entering a confining channel (width  $w_c$ ) with its leading protrusion to the parameter values found in Brückner, Schmitt, *et al.*, 2022, which leads to an excellent agreement (Fig. 3.9B). In particular, our model correctly predicts the observed non-linear dependence of  $\alpha$  on pattern width.

When comparing Eq. (3.33) to Eq. (3.11), we do however find that our model contains an additional term  $\delta(S_r - S_\ell)$  that vanishes when the cell migrates in uniform confinement but biases polarization towards the confined side in a case of asymmetric confinement as found on dumbbell-shaped patterns (Fig. 3.9C). As a consequence, in our model cells that protrude into the channel are more likely to polarize towards the channel, while both polarization directions are equally likely in Brückner, Schmitt, *et al.*, 2022. For the population-averaged migration statistics on the dumbbell-shaped patterns, this is likely to only have a small effect, but when cells encounter asymmetric confinement that we will discuss later, we will see that this plays an important role for the cellular decision making.

A second group of parameters that depends in general on pattern width are the effective spring constants and friction coefficients. Interestingly, in Brückner, Schmitt, *et al.*, 2022 the nuclear friction coefficient does depend on channel width, while the friction coefficient of the protrusion is independent of the geometry. Also here, our bottom-up model can give insights into this difference in their channel width dependence. When unconfined, the nuclear friction is determined by the unconfined width of the cell body  $w_{\text{cell}}$ , such that  $\zeta_n(x_n) = \zeta_n(w_{\text{cell}})$  (see Eq. (3.24)). If a cell migrates however into a confinement of width  $w_c$  that is narrower than the width of the cell, the nuclear friction will gradually decrease until the entire nuclear region is confined to the width  $w_c$ . To isolate the effect of the confinement and simplify the comparison to Brückner, Schmitt, *et al.*, 2022, we rewrite the nuclear friction coefficient as  $\zeta_n(x_n) = \gamma(x_n)\zeta_n(w_{\text{cell}})$ , with  $\gamma(x_n) = \zeta_n(x_n)/\zeta_n(w_{\text{cell}})$ . We are mostly interested in the minimal value of  $\gamma$  when the nuclear region is completely confined, which is then given by

$$\frac{\zeta_n(w_c)}{\zeta_n(w_{\text{cell}})} = \frac{1 + \rho_b \ell_n k_b n_0 / (k_{\text{off}}^0 \zeta_0^n) w_c}{1 + \rho_b \ell_n k_b n_0 / (k_{\text{off}}^0 \zeta_0^n) w_{\text{cell}}}. \quad (3.35)$$

We fit Eq. (3.35) to the values reported in Brückner, Schmitt, *et al.*, 2022, finding an excellent agreement between our analytic expression and the fitted parameter values at different confinement widths (Fig. 3.9D). To account for the gradual decrease of  $\gamma(x_n)$  as the nucleus moves into the bridge, we follow

Brückner, Schmitt, *et al.*, 2022 and use

$$\gamma(x_n) = \frac{\zeta_n(w_c)}{\zeta_n(w_{\text{cell}})} + \frac{1}{2} \left( 1 - \frac{\zeta_n(w_c)}{\zeta_n(w_{\text{cell}})} \right) \left( 1 - \cos \left( \frac{2\pi(x_n - x_{\text{center}})}{L} \right) \right), \quad (3.36)$$

where  $x_{\text{center}}$  denotes the center of the confinement and  $L$  is the period of the pattern. Further, our model also gives insight into the geometry independence of the protrusion friction found in Brückner, Schmitt, *et al.*, 2022. While cells can form more adhesions on wider or more densely coated adhesive patterns, wider protrusions also lead to larger contractile forces through the pattern width dependence of  $k_c$  (Eq. (3.22)). Consequently, on substrates with homogeneous adhesiveness,  $k_{\ell/r}/\zeta_a$  is independent of protrusion width and thus identical on both sides of the cell. Hence, the fact that both  $k$  and the friction coefficient of the protrusion  $\zeta_p$  in Eq. (3.10) are independent of the channel width can be interpreted as a cancelation of the channel width dependence of both parameters.

Note that there are however differences between the two models when it comes to the effective spring constants. First, in Brückner, Schmitt, *et al.*, 2022, both the protrusion and the nucleus are subject to the same spring constant and it is just the difference in friction coefficients that leads to differences in the rescaled spring constants  $k/\zeta_{n,p}$ . In contrast, our model predicts that the protrusions are subject to an additional membrane force that does not act onto the nucleus, resulting in a difference between the effective spring constants  $k_c$  and  $k_{\ell/r}$ . This difference can however be absorbed into the values of the friction coefficients, such that this does not affect the model qualitatively. More importantly however, while the model in Brückner, Schmitt, *et al.*, 2022 assumes geometry independent spring constants  $k$ , our model predicts that the pattern width dependence of  $k_c$  does not cancel out and could thus play a role for the migration behavior. Based on Brückner, Schmitt, *et al.*, 2022, it seems however as if this width dependence does not play an important role on two-state patterns. A possible reason for this could be the strong fluctuations of the protrusion coordinate and thus also the protrusion width, which determines the value of  $k_c$ . On patterns with narrower channels, we expect the rate with which cells protrude into the channel to be smaller purely for geometric reasons, such that cells mostly form unconfined protrusions on the islands. Thus we expect the average value of  $k_c$  to be significantly larger than  $k_c(w_c)$ . On wider patterns, cells protrude more often into the channel, such that the average value of  $k_c$  is closer to  $k_c(w_c)$ . This could result in a relatively weak pattern width dependence of the average spring constant  $\langle k_c \rangle$ , which could explain why a constant spring constant was sufficient in Brückner, Schmitt, *et al.*, 2022. Later, we will however discuss the migration behavior of cells that can decide between channels of different widths, where we will see that the geometry dependence of  $k_c$  does have an important role for the cellular decision making.

Finally, comparing the expressions for the protrusion dynamics found here and in Brückner, Schmitt, *et al.*, 2022 (Eqs. (3.23) and (3.10)), we see that Eq. (3.23) does not include an explicit expression that could be associated with the confining potential  $V(x_p)$  in Eq. (3.10). Instead, this can be captured through a geometry dependence of the polymerization rate. As discussed in Section 3.2, protrusion growth through actin polymerization requires the anchoring of actin filaments to the substrate through focal adhesions. Outside of the coated micropattern, this is however not possible, making it impossible

for cells to form protrusions of significant length beyond the boundaries of the pattern. We account for this by simply setting the polymerization rate to zero if a protrusion reaches beyond the boundaries of the pattern, resulting in a similar confining effect as  $V(x_p)$ .

Overall, we see that our bottom-up model is not only able to reproduce a number of key results that were previously found with data-driven approaches, but that we can also provide a mechanistic understanding of the observed phenomena, in particular the geometry-adaptation of the migration behavior. Beyond that, this approach allows us to derive analytic expressions for the pattern width dependence of a number of key model parameters, which on the one hand allows us to easily generalize our model to other pattern geometries without having to fit our model to new experimental data and on the other hand, this drastically reduces the number of parameters, since the entire pattern width dependence of the model can now be captured in a few parameters that characterize the pattern width dependence instead of having different, independent parameter values for every geometry.

To bridge the remaining gap between our model and the model found in Brückner, Schmitt, *et al.*, 2022, we consider the dynamics of a single, effective, experimentally defined protrusion coordinate that emerge from the dynamics of the two protrusions in our bottom-up model. The protrusion coordinate in Brückner, Schmitt, *et al.*, 2022 is defined as

$$x_p = \frac{\Delta x_\ell x_\ell + \Delta x_r x_r}{\Delta x_\ell + \Delta x_r}, \quad (3.37)$$

where  $\Delta x_{\ell/r}$  denotes the growth of the respective protrusion between two consecutive experimental observation times spaced by  $\Delta t$ . While  $\Delta x_{\ell/r}$  exhibit an intricate position and time dependence, we can at least find the model in Brückner, Schmitt, *et al.*, 2022 as an approximation of our bottom-up model: Assuming that the dynamics of  $\Delta x_{\ell/r}$  are slower than the dynamics of  $x_{\ell/r}$ , we approximate the dynamics of the protrusion coordinate as

$$\dot{x}_p = -\frac{k}{\zeta_a}(x_p - x_n) + \frac{\Delta x_r}{\Delta x_{\text{tot}}}\ell_a S_r r_p(x_r) - \frac{\Delta x_\ell}{\Delta x_{\text{tot}}}\ell_a S_\ell r_p(x_\ell), \quad (3.38)$$

where  $k = k_\ell = k_r$  and  $\Delta x_{\text{tot}} = \Delta x_\ell + \Delta x_r$ . Eq. (3.38) contains a simple elastic coupling of the protrusion coordinate and the nucleus together with a complex dependence on the projected polymerization velocities on both sides of the cell. The polymerization terms are phenomenologically captured in Brückner, Schmitt, *et al.*, 2022 by introducing a confinement potential that can be interpreted as the outer boundaries of the micropattern prohibiting further actin polymerization and a polarization force  $P(t)$  that essentially follows Eq. (3.33) without the additional bias term discussed above. When simulated, both models lead however to a qualitatively similar transition behavior (see Fig. 3.10). Next, we consider the nuclear dynamics and use  $k_c(x_{\ell/r}) \approx \langle k_c(x_{\ell/r}) \rangle$  together with as discussed above to rewrite Eq. (3.24) as

$$\dot{x}_n \approx \gamma_n(x_n)^{-1} k_n(x_\ell + x_r - 2x_n), \quad (3.39)$$

In the limiting case of strongly polarized cells, e.g. towards the right we get  $\Delta x_\ell + \Delta x_r \approx \Delta x_r$ , such that  $x_\ell \approx x_n$  and  $x_r \approx x_p$ . We thus find  $x_\ell + x_r - 2x_n \approx x_p - x_n$ . Similarly, in the case of a completely unpolarized cell,

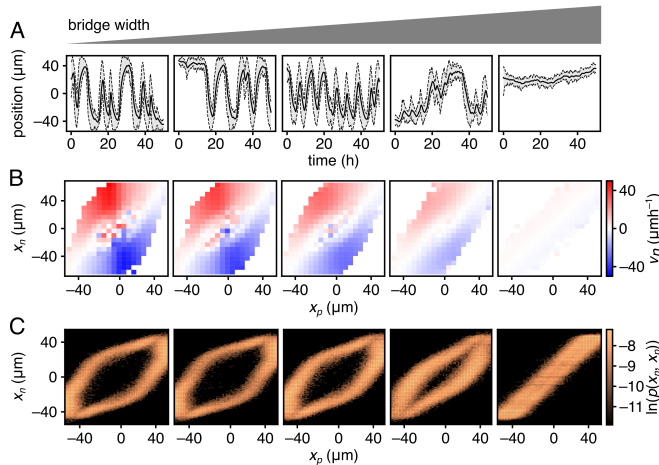


Figure 3.10: **Dynamics of the two protrusion model for varying bridge widths (4 $\mu\text{m}$ , 7 $\mu\text{m}$ , 12 $\mu\text{m}$ , 22 $\mu\text{m}$  and 35 $\mu\text{m}$ )** (taken from Flommersfeld *et al.*, 2023). **A.** Example trajectories. **B.** Nuclear velocity maps. **C.** Joint probability densities.

$\Delta x_r = \Delta x_\ell$  and thus  $x_\ell + x_r = 2x_p$ . At the same time,  $x_p \approx x_n$ , such that again  $x_\ell + x_r - 2x_n \approx x_p - x_n$ . Hence, in those two limiting cases we recover the nuclear dynamics found in Brückner, Schmitt, *et al.*, 2022.

In Brückner, Schmitt, *et al.*, 2022, it was also shown that the structure of the drift term  $F(x_n, v_n)$  of the effective underdamped description in Brückner, Fink, Schreiber, *et al.*, 2019 (Eq. (3.8)) arises from the interplay between the nucleus, the effective protrusion coordinate  $x_p$ , and the cell polarity. This allows us to bridge the entire gap from our bottom-up model to the top-down description of the migration dynamics on the level of an underdamped Langevin equation.

### Cellular decision making in asymmetric confinement

Apart from connecting the emergent, overall migration behavior to underlying molecular processes, once constrained from data and with the help of a top-down model, our bottom-up approach also allows us to predict cellular migration behavior on different substrates. To demonstrate this, we consider the role of lateral confinement in a different geometry (Fig. 3.11A). There, cells can migrate on a chain of square-shaped islands that are connected by channels of increasing width, such that cells on an island encounter different degrees of lateral confinement on both sides of the nucleus (Fig. 3.11B). As a consequence of this asymmetry, while in the case of the two-state pattern, the bias term in Eq. (3.33) and the width dependence of  $k_c$  (Eq. (3.22)) could be neglected, here we expect them to play an important role in the cellular decision making.

In particular, we expect that confinement has opposing effects on the preferred direction of migration. On the one hand, confinement-induced actin alignment stimulates polarization towards the narrower channel (Eq. (3.33)). On the other hand, the contractility decreases with confinement, due to  $k_c$  be-

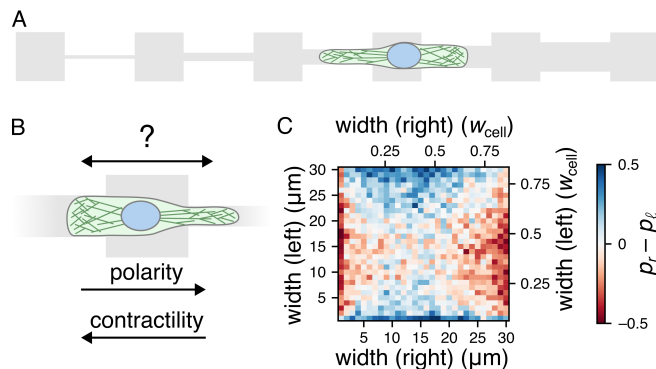


Figure 3.11: **Cellular decision making with asymmetric protrusions** (adapted from Flommersfeld *et al.*, 2023). **A.** Sketch of the substrate geometry. Cells migrate on a chain of islands that are connected by bridges of increasing width. **B.** Illustration of the protrusion driven cellular decision making. Cells form protrusions of different width on both sides of the nucleus. This affects cell polarity as well as contractility. **C.** Predicted migration bias of a cell seeded on an island with two adjacent, infinitely long channels of different widths.  $p_r/\ell$  denotes the probability that the cell migrates into the right/left channel.

ing proportional to the pattern width  $w_p$  (Eq. (3.22)). We do however expect this second effect to saturate at some point for a number of reasons: First, once the pattern is wider than the unconfined width of the protrusion, the force generation will be independent of the pattern width. Second, at some point all available actin and myosin in the protrusion are involved in the contraction, such that even if the protrusion is wider, it is not possible to use more actin and myosin in the protrusion. Finally, if the protrusion is significantly larger than the nucleus, only a part of it might be mechanically linked to the nucleus and thus contributing to the nuclear translocation. To account for such a mechanism, we thus use

$$k_c(w_p) = \begin{cases} \frac{w_p}{w_{\text{sat}}} k_c^{\text{free}}, & w_p < w_{\text{sat}} \\ k_c^{\text{free}}, & \text{else} \end{cases}, \quad (3.40)$$

where  $k_c^{\text{free}}$  denotes the effective spring constant of an unconfined cell and the free parameter  $w_{\text{sat}}$  is the width at which the pattern width dependence of the effective spring constant saturates that needs to be determined through comparison with experimental data. For  $w_p < w_{\text{sat}}$ , we do however expect a net force away from confinement in unpolarized cells. To demonstrate this, we consider cells that can choose between two infinitely long channels of different width. In that case, our model predicts then that the preferred migration direction depends on the two channel widths and transitions from favoring wider to narrower channels with increasing width (Fig. 3.11C). Applied to the experimentally more relevant scenario of migration on island chains, we expect a transition from a bias towards the right (wider) channel at narrow channel widths to a bias towards the left (narrower) channel at wide channel widths, which we indeed observe experimentally for two different mesenchymal cell lines (Fig. 3.12A) (see Flommersfeld *et al.*, 2023 for experimental details).

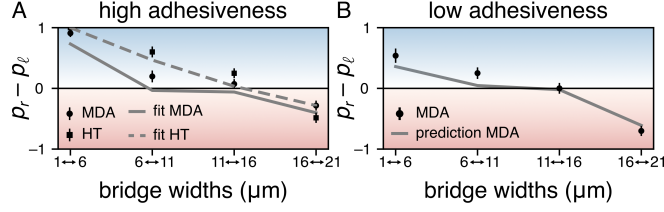


Figure 3.12: **Cellular decision making in lateral confinement** (taken from Flommersfeld *et al.*, 2023). **A.** Experimentally observed migration biases together with model fits for MDA-MB-231 and HT-1080 cells, where  $p_{r/\ell}$  denotes the probability for a cell to choose the right/left channel. With increasing bridge widths, cells transition from a bias towards wider bridges to a bias towards narrower bridges. **B.** Predicted migration biases of MDA-MB-231 cells on patterns of reduced adhesiveness together with experimental data.

Apart from the pattern geometry, other physical properties of the substrate, such as adhesiveness, as well as the internal properties of the migrating cells will affect cellular decision. In the following we will discuss how these will affect the parameters of our model and the expected cellular migration behavior. Starting with the adhesive properties of the substrate, we consider migration on a pattern of reduced adhesiveness (experimentally realized through a lower concentration of adhesion molecules on the surface). The density of adhesive molecules on the surface  $\rho_{\text{ad}}$  determines the number of adhesive bonds that the cell can form. We thus expect that the bond density  $\rho_b \propto \rho_{\text{ad}}$ , which affects the friction coefficients  $\zeta_{a/n}$ . To check if  $\rho_b$  also contributes to the effective spring constants we consider Eq. (3.22), from which we get

$$k_c = \frac{4\tau_1 \tilde{N}_F \rho_b \rho_m w_p f_s}{\left(\zeta_a - \tilde{N}_F \rho_b \rho_m w_p f_s\right) h_p} w_p. \quad (3.41)$$

Using however that  $\zeta_a = \zeta_1^a(0) = \rho_b \ell_r k_b n_0 w_p / k_{\text{off}}^0$  (Eq. (3.16)), we find that  $\rho_b$  cancels out in Eq. (3.22) and the effective spring constants are independent of the adhesiveness. This leaves us with the friction coefficients  $\zeta_a/n$  as  $\rho_b$  sensitive parameters. As discussed in the Section 3.3, the contribution of the viscous drag to the total drag coefficient of the actin filaments can be neglected. Hence,  $\zeta_a \propto \rho_b$  and the rescaled spring constants  $k_{\ell/r}/\zeta_a \propto \rho_b^{-1}$ . In contrast, for the nuclear friction the viscous drag does play an important role. To find an expression for  $\zeta_n$  in terms of  $\rho_{\text{ad}}$ , we consider Eq. (3.35) and write the contribution of the viscous drag to the nuclear friction coefficient  $\zeta_0^n$  as

$$\zeta_0^n = \frac{\zeta_0^n}{\zeta_n(w_{\text{cell}})} \zeta_n(w_{\text{cell}}) = \left(1 + \frac{\rho_b \ell_n k_b n_0}{k_{\text{off}}^0 \zeta_0^n} w_{\text{cell}}\right)^{-1} \zeta_n(w_{\text{cell}}) \quad (3.42)$$

and thus

$$\zeta_1^n(w_{\text{cell}}) = \left(1 - \left(1 + \frac{\rho_b \ell_n k_b n_0}{k_{\text{off}}^0 \zeta_0^n} w_{\text{cell}}\right)^{-1}\right) \zeta_n(w_{\text{cell}}). \quad (3.43)$$

Using that  $\zeta_1^n = \rho_b \ell_n k_b n_0 w_n / k_{\text{off}}^0$  we get

$$\zeta_n(w_{\text{cell}}) = \frac{\rho_b \ell_n k_b n_0 w_{\text{cell}} / (k_{\text{off}}^0 \zeta_0^n)}{1 - (1 + \rho_b \ell_n k_b n_0 w_{\text{cell}} / (k_{\text{off}}^0 \zeta_0^n))^{-1}} \zeta_0^n. \quad (3.44)$$

From the fit shown in Fig. 3.9D, we find

$$\rho_b \ell_n k_b n_0 w_{\text{cell}} / (k_{\text{off}}^0 \zeta_0^n) = 8.75 \rho_b(\rho_{\text{ad}}) / \rho_b(\rho_{\text{ad}}^{\text{ref}}), \quad (3.45)$$

where  $\rho_{\text{ad}}^{\text{ref}}$  denotes the fibronectin concentration for the experiments with high adhesiveness (corresponding to Fig. 3.12A). We can then rewrite Eq. (3.44) as

$$\begin{aligned} \zeta_n(w_{\text{cell}}, \rho_{\text{ad}}) &= \frac{8.75 \rho_b(\rho_{\text{ad}}) / \rho_b(\rho_{\text{ad}}^{\text{ref}})}{1 - (1 + 8.75 \rho_b(\rho_{\text{ad}}) / \rho_b(\rho_{\text{ad}}^{\text{ref}}))^{-1}} \zeta_0^n \\ &= \frac{\rho_b(\rho_{\text{ad}})}{\rho_b(\rho_{\text{ad}}^{\text{ref}})} \frac{1 - (1 + 8.75)^{-1}}{1 - (1 + 8.75 \rho_b(\rho_{\text{ad}}) / \rho_b(\rho_{\text{ad}}^{\text{ref}}))^{-1}} \zeta_n(w_{\text{cell}}, \rho_{\text{ad}}^{\text{ref}}). \end{aligned} \quad (3.46)$$

Based on this, we can determine the values of the rescaled spring constant for MDA-MB-231 cells on patterns with reduced adhesiveness (corresponding to Fig. 3.12B, where  $\rho_{\text{ad}} = 0.5 \rho_{\text{ad}}^{\text{ref}}$ ) relative to the experiment with high adhesiveness. To test our model, we thus fix our model parameters corresponding to MDA-MB-231 cells on highly adhesive patterns by fitting the data in Fig. 3.12A and then successfully predict the migration biases with reduced adhesiveness (Fig. 3.12B). Even though the effect of the changed adhesiveness varies from island to island, we find overall that for cells on less adhesive substrates, biases towards the narrower channel are increased and biases towards the wider channel are reduced.

Next, we use our model to propose a possible interpretation of the differences between MDA-MB-231 cells and HT-1080 cells and discuss the role of model parameters associated with internal differences between cell lines in cellular decision making. We observe two trends when comparing the parameter values obtained from our fits to the experimental data shown in Fig. 3.12A (see Flommersfeld *et al.*, 2023 for the obtained values): The rescaled spring constants ( $k/\zeta$ ) are slightly lower for the HT-1080 cells than for the MDA-MB-231 cells and parameters associated with the polarization dynamics ( $\alpha, \beta, \delta$ ) are strongly reduced in HT-1080 cells compared to MDA-MB-231 cells. The difference in rescaled spring constants could be explained through different adhesive properties of the cell lines or differences in the actin and myosin expression levels. The more striking difference between the two cell lines is however the difference in polarization, where all parameters associated with the polarization dynamics are reduced by about a factor of two. There are three obvious biological parameters that impact the polarization dynamics: the diffusion constant of the polarity cue in the cytosol  $\tilde{D}$ , the average polarity cue concentration  $c_0$  and the fraction of actin bound polarity cue  $n_c$  (see Eqs. (3.33) and (3.34)), where  $c_0$  only occurs in combination with  $n_c$ . An explanation for the observed difference in the polarization-associated parameters could thus be an overall reduced concentration of polarity cue in HT-1080 cells compared to MDA-MB-231 cells. Interestingly however, also  $D - 8n_c c_0 \ell_a r_1 L_c^{-1}$  is reduced by about a factor of two even though  $D = 4(1 - n_c) \tilde{D} L_c^{-2}$  (Eq. (3.30)) does not directly depend on  $c_0$ . This could indicate a coupling between the overall concentration of the polarity cue  $c_0$  and the bound fraction of the polarity cue  $n_c$ . A possible

mechanism behind such a coupling could be that with a lower absolute number of polarity cue, more unoccupied binding sites are available, leading to an increased  $n_c$  and thus a decrease of  $D$  with decreasing  $c_0$ . Regardless of the detailed mechanism that needs further experimental exploration, our model suggests that the differences between HT-1080 and MDA-MB-231 cells can be summarized as HT-1080 cells being less contractile and crucially less polarized than MDA-MB-231 cells.

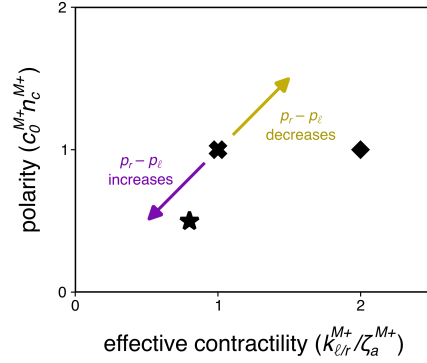


Figure 3.13: **The polarity-contraction phase space for migration in asymmetric lateral confinement** (taken from Flommersfeld *et al.*, 2023). The migration behavior of cells on island chains can be qualitatively characterized in the contractility-polarity space. The estimated position of the different island chain experiments relative to the case of MDA-MB-231 cells on highly adhesive patterns (M+) are indicated by the black markers (cross: MDA-MB-231 cells on highly adhesive patterns, diamond: MDA-MB-231 cells on less adhesive patterns, star: HT-1080 cells on highly adhesive patterns).

Inspired by the observed separation of biological parameters in either affecting the effective contractility or polarizability of cells, we characterize cellular migration in asymmetric lateral confinement qualitatively in a reduced two-dimensional phase space consisting of the effective contractility and the polarizability of cells. We estimate the position corresponding to different experimental conditions and cell lines in this reduced phase space by the position along the effective contractility dimension to correspond to the value of  $k_{r/\ell}/\zeta_a$  and the position along the polarization dimension to be determined by the value of  $n_c c_0$  (Fig. 3.13). The position in the polarity-contraction space, determines the cellular decision making as following: Increasing polarizability (e.g. by going from HT-1080 to MDA-MB-231 cells) leads to a stronger effect of the confinement induced actin alignment and consequent protrusion growth towards the narrower channel, which results in an overall increase of the bias towards the narrower channel and thus a decrease in  $p_r - p_\ell$  for the orientation shown in Fig. 3.11. Perhaps counterintuitively, we also observe that an increased effective contractility (e.g. because of reduced adhesiveness) increases the bias towards narrower channels. This can be explained as follows: On the one hand, an increase in the overall contractility increases the absolute difference in spring constants between the two sides and thus increases the net force towards the wider side in unpolarized cells. On the other hand, for polarized

cells increased contractility also reinforces the effect of protrusion growth according to Eq. (3.22), such that overall the bias towards the narrower channel increases with increasing contractility.

To summarize, connecting a detailed bottom-up model to data-driven top-down models for migration in lateral confinement did not only allow us to identify possible mechanisms underlying the observed migration phenomenology but also led to new insights into the role of protrusion width for cellular force generation. Beyond that, it revealed a bias in the polarization dynamics in asymmetric confinement that remained elusive for the previously established data-driven approaches when applied to migration on two-state patterns. These new aspects of our migration model are direct consequences of the proposed molecular mechanisms underlying the structure of our simple, coarse grained model. To test if width dependent protrusion force and biased polarization can in fact be observed experimentally, we applied our model to island chains, where cells typically encounter confinements of different widths on both sides of the cell body. The observed dependence of the cellular decision making on the confinement widths does agree qualitatively with the predictions of our model and we show that our model can even quantitatively predict the effect of substrate adhesiveness on the migration behavior, further supporting our model. Finally, our model illustrates how both cell contractility and polarity determine cellular decision making in confined environments, which can be characterized in a reduced phase space for cellular decision making in confinement, the polarity-contractility space.

### 3.5 Biased migration on anisotropic substrates

After using migration in laterally confining micropattern geometries to test and constrain our model, we aim to demonstrate its generality by applying to explain the emergence of biased migration on substrates with anisotropic physical properties. For that we first discuss migration on asymmetric, *ratchet*-shaped adhesive patterns that result in a directed migration behavior called *ratchetaxis* before briefly discussing an extension of our model to cell migration on compliant substrates with varying stiffness and show how our model gives rise to *durotaxis*.

#### Ratchetaxis

While we discussed the effect of the overall substrate adhesiveness on the migration behavior in the Section 3.4, how anisotropies in the adhesion properties of the cellular microenvironment can steer migration behavior remained unexplored there. Here we want to apply our model to an experimental system that induces such anisotropies in the cellular adhesions in an elegant way through the use of asymmetric micropatterns (see Caballero, Comelles, *et al.*, 2015 for a review of the experimental system). For that, cells are placed on a series of adhesive patches with a non-adhesive region between neighboring patches. Cells that are located on one patch can then engage with neighboring patches through their protrusions, which ultimately allows the cell to pull its cell body over the non-adhesive region to a neighboring patch. Depending on the shape of the patches, the strength and stability of the protrusions on both sides of

the cell are different, resulting in biased migration (Caballero, Voituriez, *et al.*, 2014).

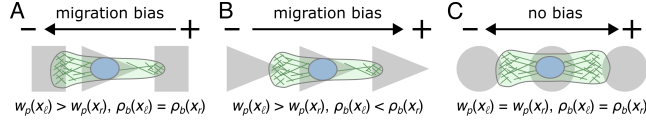


Figure 3.14: **Cell migration on directed substrates (ratchetaxis)** (taken from Flombersfeld *et al.*, 2023). **A.** Triangular pattern with symmetric neighboring patches. **B.** Periodic triangular patches. **C.** Periodic circular patches. In contrast to symmetric patterns (C), triangular patterns (A, B) lead to protrusions of different widths  $w_p$  on both sides of the nucleus. If neighboring patterns are also asymmetric (B) this can result in different densities of adhesive bonds  $\rho_b$  at the front of the protrusions.  $x_{\ell/r}$  denote the position of the left/right protrusion. These asymmetries in protrusion width and adhesiveness lead to biased migration.

To disentangle the effect of pattern shape on migration behavior, we consider three different pattern geometries (Fig. 3.14). First, cells on a single triangular patch pointing to the right with symmetric, rectangular neighboring patches. Second, a periodic series of triangular patches pointing to the right and finally as a control a series of circular patches. Following the experimental characterization in Caballero, Voituriez, *et al.*, 2014, we denote the direction corresponding to the pointed side of triangular patterns as  $+$ -direction and the direction corresponding to the blunt side as  $-$ -direction. On the first pattern, due to the asymmetry of the patch on which the cell body is located, the width over which protrusions can form in the  $-$ -direction is wider. According to Eq. (3.22) the effective spring constant of a protrusion is proportional to its width. Hence, we account for this asymmetry of the patch through an asymmetry in the effective spring constants on both sides of the cell such that  $k_c(x_\ell) > k_c(x_r)$ , where we followed the orientation of the pattern as shown in Fig. 3.14, with the pointed side of the pattern being oriented towards the right. As discussed above in more detail in Section 3.4,  $k_{\ell/r}/\zeta_a$  is however independent of the width of the protrusion on homogeneously coated substrates due to the cancellation of the pattern width dependence of  $k_{\ell/r}$  and  $\zeta_a$ . Thus in the case of symmetric neighboring patches (Fig. 3.14A, C),  $k_{\ell/r}/\zeta_a$  is independent of the shape of the patch on which the cell body is located. In the case of asymmetric neighboring patches however (Fig. 3.14B), due to the tapering of the pattern, protrusions in the  $-$ -direction overlap with non-adhesive regions. This reduces the average adhesion bond density  $\rho_b$  below that protrusion, resulting in an asymmetry in the values of  $\zeta_a$  on both sides of the cell with  $\zeta_a(x_\ell) < \zeta_a(x_r)$ .

Accordingly, to check if our model does give rise to the correct migration biases on the different patterns, we vary  $k_\ell/\zeta_a$  and  $k_c(x_\ell)/\zeta_n$  while keeping  $k_r/\zeta_a$  and  $k_c(x_r)/\zeta_n$  fixed to introduce an asymmetry between the two sides of the cell. We then quantify the migration bias in terms of the average long-term bias  $\bar{p} = \langle (N_+ - N_-)/(N_+ + N_-) \rangle$  for the different parameter combinations (Fig. 3.15A). Following the previous discussion of the effect of pattern geometry on parameter values, we increase  $k_c(x_\ell)/\zeta_n$  with fixed  $k_\ell/\zeta_a$  to model migra-

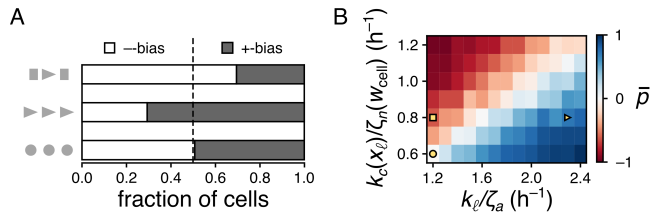


Figure 3.15: **Migration biases on different geometries** (adapted from Flommersfeld *et al.*, 2023). **A.** Migration biases for different model parameters for different geometries. Pattern geometry affects the rescaled effective spring constants  $k_c(x_{\ell/r})/\zeta_n(w_{\text{cell}})$  and  $k_{\ell/r}/\zeta_a(x_{\ell/r})$  and thus the overall migration bias  $\bar{p}$ . To explore the effect of the asymmetry in rescaled spring constants, we keep  $k_c(x_r)/\zeta_n(w_{\text{cell}})$  and  $k_r/\zeta_a(x_r)$  fixed while varying the other parameters. The parameter values corresponding to the patterns shown in Fig. 3.14 are indicated by yellow markers (periodic circles pattern: circle, single triangle pattern: square, periodic triangle pattern: triangle). **B.** The model reproduces the experimentally observed first-step migration biases on different micropatterns.

tion on a triangular pattern with symmetric neighboring patches (Fig. 3.14A). Consistent with experimental observations in Caballero, Voituriez, *et al.*, 2014, this results in biased migration towards the --direction both in the long-term bias (Fig. 3.15A) as well as for the first step migration behavior (Fig. 3.15B) for which a majority of cells performs a step in the --direction. To model migration on periodic triangular patterns, we then also increase  $k_{\ell}/\zeta_a$ , which indeed reverses the migration bias and ultimately results in a +-bias for both the long-term as well as the first step migration biases (Fig. 3.15A, B) which is again consistent with the data in Caballero, Voituriez, *et al.*, 2014. The values used for the simulations of the first step bias on the different geometries are indicated by a yellow markers in Fig. 3.15A. We thus see that our model can easily be generalized to describe migration on different confining geometries.

To explore the behavior for other parameter combinations than the ones describing the three geometries shown in Fig. 3.14 we consider migration on periodic triangular patterns with varying pattern spacing (Lo Vecchio *et al.*, 2020). Increased pattern spacing  $\Delta x_{\text{pattern}}$  leads to a reduced adhesion density below the protrusion and thus changes in  $\zeta_a(x_{\ell/r})$ . To derive an analytical expression for the change in  $k_{\ell/r}/\zeta_a(x_{\ell/r})$  with pattern spacing, we consider the adhesive area below a protrusion  $A_{\text{ad}}$ , which differs depending on what side of the triangular neighboring patch a protrusion encounters. Following the orientation shown in Fig. 3.14 the right protrusion encounters the blunt end of the pattern while the left protrusion overlaps with the pointed end, which can be written as

$$A_{\text{ad}} = g_{\ell/r}(L_p - \Delta x_{\text{pattern}})w_p, \quad (3.47)$$

with  $L_p$  and  $w_p$  denoting the length and width of the protrusion respectively and the geometric factor  $0 < g_{\ell/r} \leq 1$  accounts for the shape of the pattern. Since protrusions are typically narrower than the blunt end of the pattern, we choose  $g_r = 1$  and  $g_{\ell} < 1$ . The average density of adhesive molecules below

the protrusions is then given by

$$\rho_{\text{ad}} = \rho_{\text{ad}}^{\text{hom}} \frac{A_{\text{ad}}}{A_p} = \rho_{\text{ad}}^{\text{hom}} g_{\ell/r} (1 - L_p^{-1} \Delta x_{\text{pattern}}), \quad (3.48)$$

where  $\rho_{\text{ad}}^{\text{hom}}$  is the average adhesion density on homogeneously coated surfaces. For the cell line used in Lo Vecchio *et al.*, 2020 (NIH3T3 cells), the number of adhesion bonds that cells can form saturates at high numbers of adhesive molecules. We include such a saturation behavior through through

$$\rho_{\text{b}} = \rho_{\text{b}}^{\text{hom}} \tanh\left(\frac{\rho_{\text{ad}}}{\rho_{\text{sat}}}\right), \quad (3.49)$$

where  $\rho_{\text{sat}}$  determines at what adhesion molecule density the bond density saturates and we assumed that the density of the pattern is high enough such that the bond density on homogeneously coated surfaces  $\rho_{\text{b}}^{\text{hom}}$  is equal to the saturation density, which was shown to be the case in Lo Vecchio *et al.*, 2020. Using Eqs. (3.48) and (3.49) together with the expression for  $\zeta_a$  (see Section 3.3), we can express the rescaled spring constants  $k_{\ell/r}/\zeta_a$  in terms of the pattern spacing  $\Delta x_{\text{pattern}}$  as

$$\frac{k_{\ell/r}}{\zeta_a} = \frac{k_{\ell/r}}{\zeta_a^{\text{hom}}} \frac{1}{\tanh\left(\frac{g_{\ell/r} \rho_{\text{ad}}^{\text{hom}}}{\rho_{\text{sat}}} (1 - L_p^{-1} \Delta x_{\text{pattern}})\right)}, \quad (3.50)$$

where  $\zeta_a^{\text{hom}}$  is the effective friction coefficient of the protrusion on a homogeneously coated substrate.

For the experiments in Caballero, Voituriez, *et al.*, 2014, a pattern spacing of  $\Delta x_{\text{pattern}} = 20.5\mu\text{m}$  was used and  $L_p$  was found to be approximately  $27\mu\text{m}$ . By imposing that at a pattern spacing of  $20.5\mu\text{m}$  the rescaled spring constants match the values shown in Fig. 3.15A ( $k_r/\zeta_a = 1.2 \text{ h}^{-1}$  and  $k_{\ell}/\zeta_a = 2.3 \text{ h}^{-1}$ ), we constrain the parameters  $k_{\ell/r}/\zeta_a$  and  $g_{\ell}$  (Fig. 3.16A). This leaves us with a single free parameter  $\rho_{\text{sat}}/\rho_{\text{ad}}^{\text{hom}}$  that determines the onset of saturation. For a value of  $\rho_{\text{sat}}/\rho_{\text{ad}}^{\text{hom}} = 0.05$  ( $g_{\ell} = 0.12$ ,  $k_{\ell/r}/\zeta_a^{\text{hom}} = 1.2 \text{ h}^{-1}$ ), we find good agreement with the experimental data in Lo Vecchio *et al.*, 2020 (Fig. 3.16B).

Overall, we conclude that our mechanistic model can give rise to a similar biased migration behavior on asymmetric adhesive patterns as the phenomenological treatment of this process in terms of a biased persistent random walk in Caballero, Voituriez, *et al.*, 2014. Our approach does however yield a direct mechanistic explanation of the direction-dependent migration persistence: The increased protrusion width on the blunt side of the pattern is counteracted by a decrease in average protrusion length due to the reduced average adhesion density on that side. Depending on the balance between those two effects that is affected by pattern spacing, this results in the overall force generated in the  $-$ -direction to either be larger or smaller than the protrusion force in the  $+$ -direction. While these two effects of the pattern geometry on protrusion formation were also identified from the experimental analysis in Caballero, Voituriez, *et al.*, 2014, the theoretical treatment in terms of a direction dependence of the persistence in a discrete, persistent random walk (see Section 3.1) was then based on phenomenological arguments. Here, we show that such a biased migration also directly emerges in a mechanistic, bottom-up migration model.

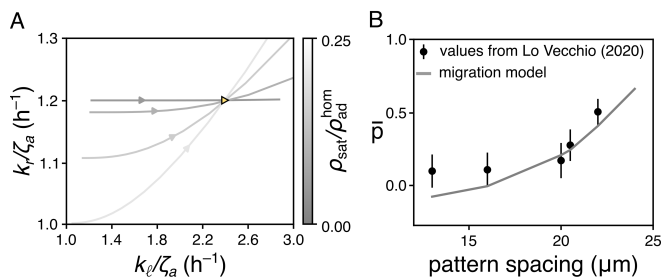


Figure 3.16: **Effect of pattern spacing on the migration bias on periodic triangular patterns** (taken from Flommersfeld *et al.*, 2023). **A.** Dependence of the rescaled spring constants on pattern spacing for different values of the saturation parameter  $\rho_{\text{sat}}/\rho_{\text{ad}}^{\text{hom}}$  (0.05, 0.10, 0.15, 0.20). With increasing pattern spacing both  $k_\ell/\zeta_a$  and  $k_r/\zeta_a$  increase, but  $k_\ell/\zeta_a$  is much more sensitive to the pattern spacing due to the asymmetric shape of the adhesive patches. The parameter combination chosen to fit migration bias at a pattern spacing of 20.5  $\mu\text{m}$  in the main text is indicated by the yellow triangle. **B.** Effect of pattern spacing on the average long-term migration bias  $\bar{p} = \langle (N_+ - N_-)/(N_+ + N_-) \rangle$  on periodic triangular patterns, with the number of steps in the  $+/-$ -direction  $N_{+/-}$ . As observed experimentally, the bias increases with increasing pattern spacing (experimental data from Lo Vecchio *et al.*, 2020)

## Durotaxis

Another form of directed cell migration due to anisotropies in the environment is durotaxis. A mechanistic model with a similar structure to ours was previously shown to give rise to single cell and collective durotaxis (Sunyer, Conte, *et al.*, 2016). In this model, the interaction between the molecular clutch at the front of the protrusion with a substrate of different stiffness on both sides of the cell gave rise to a net force towards the stiffer region. Here we briefly discuss some preliminary results on how such a mechanism would be implemented in our model and compare the emergent durotactic behavior from the resulting model to a phenomenological model that treats durotaxis in terms of a persistent random walk with stiffness dependent persistence (Novikova *et al.*, 2017). We show that such a stiffness dependent persistence time does not arise from a purely mechanical model, but does arise in our model when accounting for the effect of the substrate stiffness on the polarization dynamics.

As discussed in Section 3.1, cell migration is commonly modeled in terms of a persistent random walk. In the continuous limit, the resulting migration dynamics are described by the telegrapher's equation (Eq. (3.2)). In this model, there are two obvious ways how a migration bias could be introduced: either through a position dependent persistence time  $\lambda(x)$  or a position dependent velocity  $v_0(x)$ . There are however contradictory experimental results on the coupling between cell velocity and substrate stiffness, with one study finding a decrease in velocity with increasing stiffness (Missirlis *et al.*, 2014), another study finding an increase (House *et al.*, 2009), and a third study finding no stiffness dependence at all (Raab, Swift, *et al.*, 2012). In contrast all these studies find an increase in persistence time with increasing stiffness, suggesting that

while the stiffness dependence of the migration velocity might differ between cell types, the coupling between persistent time and substrate stiffness seems to be a relatively general feature of migrating cells. Based on this, in Novikova *et al.*, 2017 it is shown that the telegrapher's equation with a position dependent persistent time is sufficient to explain durotaxis, a more detailed comparison to experimental data is however lacking. In contrast to this, in Sunyer, Conte, *et al.*, 2016 it is shown that a mechanistic model of a similar structure to ours can explain individual and collective durotaxis. There, collective durotaxis is much more efficient, since the distance over which a cell collective can probe the substrate stiffness is bigger than the distance that an individual cell can cover, leading to a higher sensitivity to shallow stiffness gradients. Since this study was however mainly concerned with collective durotaxis, a more detailed analysis of the emergent single cell durotactic behavior is missing. In particular, they did not consider the stiffness dependence of the persistence time and migration velocity, making a comparison to the phenomenological model in Novikova *et al.*, 2017 difficult. Here, we want to sketch out how the mechanism proposed in Sunyer, Conte, *et al.*, 2016 can be implemented in our model (Fig. 3.17), discuss a possible coupling between substrate stiffness and the polarity dynamics and briefly compare the resulting durotactic behavior to the phenomenological model in Novikova *et al.*, 2017.

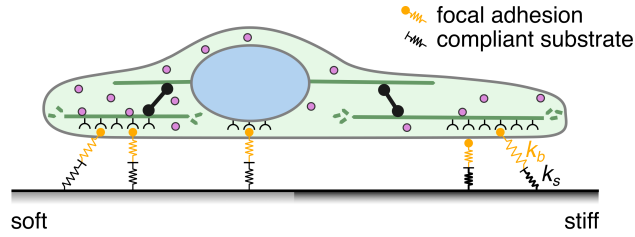


Figure 3.17: **Migration model on compliant substrates.** The substrate is modeled in terms of elastic springs that are put in series to the adhesion bonds that connect the insight of the cell to the substrate.

The model is based on a change in the effective bond stiffness  $k'_b$  of the adhesion bonds when binding to a soft substrate. This is modeled by putting a second spring representing the compliant substrate (spring constant  $k_s$ ) in series with the adhesion bonds (Fig. 3.17). The effective stiffness of the combined spring is then given by

$$k'_b(x) = (k_s^{-1}(x) + k_b^{-1})^{-1}. \quad (3.51)$$

Replacing  $k_b$  with  $k'_b(x)$  in the friction coefficients of  $\zeta_a/n$  then leads to a stiffness-sensitive migration model. Since the effective spring constants  $k_c$  and  $k_{\ell/r}$  depend on  $\zeta_a$  (Eqs. (3.22) and (3.23)), this also leads to a stiffness dependence of the spring constants. Overall, we find that the rescaled spring constants  $k_c/\zeta_n$  and  $k_{\ell/r}/\zeta_a$  all increase with decreasing stiffness. Based on the observation that viscous drag of the nucleus also significantly contributes to  $\zeta_n$ , while  $\zeta_a$  is dominated by the adhesive friction, we expect however  $k_{\ell/r}/\zeta_a$  to be stronger affected by changes in the substrate stiffness than  $k_c/\zeta_n$ .

Based on this discussion, we simulate our model on a substrate with sharp transition from a soft region on the left to a stiff region on the right (Fig. 3.17)

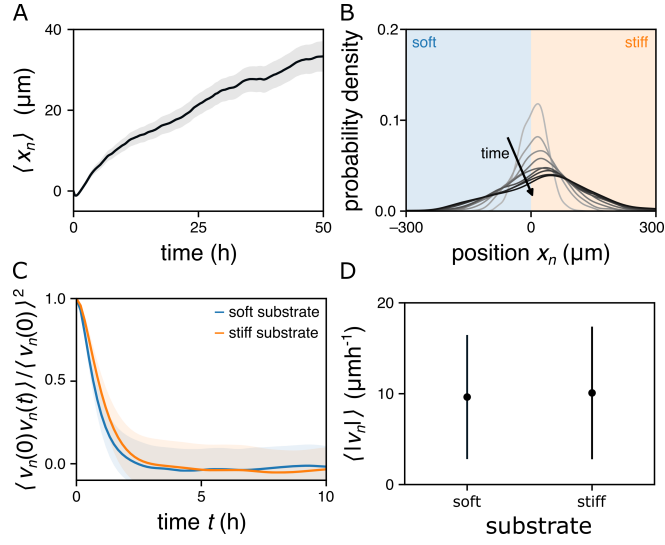


Figure 3.18: **Durotaxis with a purely mechanical ratchetaxis mechanism and little stiffness sensitivity of  $k_c/\zeta_n$ .** **A.** The average nuclear position over time shows a clear trend towards the stiffer region ( $x_n > 0$ ). **B.** The distribution of  $10^3$  cells on the substrate that were initiated at  $x_n(t = 0) = 0$  gets increasingly asymmetric as cells spread over the substrate ( $\Delta t = 5$ h). **C.** The velocity autocorrelation on soft and stiff homogenous substrates reveal a slight increase in persistence time on the stiffer substrate. **D.** The average cell speed on soft and stiff substrates show as slight increase in cell speed on stiff substrates. Error bars and shaded regions indicate one standard deviation. Simulation parameters can be found in Section 3.7.

by increasing both  $k_c/\zeta_n$  and  $k_{\ell/r}/\zeta_a$  in the soft region. To do so, we seed individual cells at the transition point from soft to stiff ( $x_n = 0$ ) and track their migration dynamics. If the difference in  $k_{\ell/r}/\zeta_a$  on both sides of the substrate is larger than the difference in  $k_c/\zeta_n$ , this does indeed result in a migration bias towards the stiffer region of the substrate (Fig. 3.18A, B). As we increase the difference in  $k_c/\zeta_n$  while keeping the difference in  $k_{\ell/r}/\zeta_a$  the same, we do however observe a reduced durotaxis efficiency (Fig. 3.19A, B). The underlying mechanism can be illustrated by considering a cell with one protrusion in the soft and the other protrusion in the stiff region: The protrusion in the softer region, will effectively experience a smaller adhesive friction, resulting in a shorter protrusion. At the same time, the reduced adhesive friction results in a faster retrograde flow and an increased value of  $k_c$ . However, if the shortening of the protrusion is stronger than the increase in  $k_c$  (i. e.  $k_{\ell/r}/\zeta_a$  is more sensitive to  $k_s$  than  $k_c/\zeta_n$ ), the protrusion force  $k_c L_p$  will be reduced on the soft side leading to a net force pulling the nucleus towards the stiffer side. To compare the migration behavior of our model to the stiffness-sensitive telegrapher's equation (Novikova *et al.*, 2017), we quantified the migration persistence and velocity on homogeneous substrates of different stiffness, corresponding to the two regions in the previous scenario (Figs. 3.18C, D and 3.19C, D). In the case where  $k_c/\zeta_n$  is relatively little affected by the substrate stiffness (Fig. 3.18),

both the persistence time (quantified through the velocity autocorrelation) as well as the average cell speed slightly increase on stiffer substrates. Interestingly, when we increased the stiffness-sensitivity of  $k_c/\zeta_n$  (Figs. 3.19) we observed however a decrease in average cell speed with increasing stiffness while still observing an increased persistence time. This sensitivity of the qualitative behavior of the average cell speed to the precise parameter values might explain the conflicting experimental findings on the effect of substrate stiffness on cell velocity. Overall, we find however that the stiffness-dependence of both statistics is relatively minor in this model.

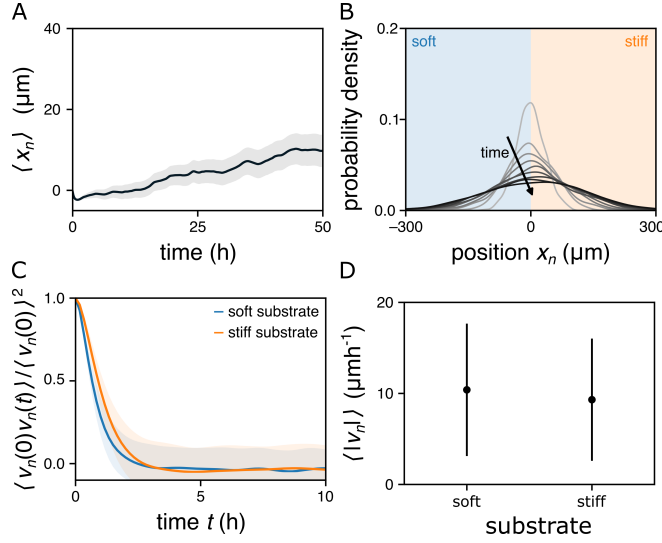


Figure 3.19: **Durotaxis with a purely mechanical ratchetaxis mechanism but higher stiffness sensitivity of  $k_c/\zeta_n$ .** **A.** The average nuclear position shows a weaker trend towards the stiffer region ( $x_n > 0$ ) compared to Fig. 3.18. **B.** The asymmetry in the distribution of  $10^3$  cells on the substrate ( $x_n(t=0) = 0$ ) is reduced ( $\Delta t = 5$ h). **C.** The velocity autocorrelation on soft and stiff homogenous substrates reveal a slight increase in persistence time on stiffer substrates. **D.** The average cell speed is slightly decreased on stiff substrates in contrast to Fig. 3.18. Error bars and shaded regions indicate one standard deviation. Simulation parameters can be found in Section 3.7.

A key difference between the purely mechanical model in Sunyer, Conte, *et al.*, 2016 and our migration model is that our model also accounts for the polarization dynamics of cells. These are determined by the retrograde flow and thus in principle depend on the adhesive friction and protrusion length. So far, we neglected this coupling between stiffness and polarity and focused on the mechanism proposed in Sunyer, Conte, *et al.*, 2016 instead. To get an intuition for the effect that substrate stiffness has on the polarization dynamics, we consider the average protrusion length of a stationary cell on a compliant substrate, which is given according to Eq. (3.23) by

$$L_p = \frac{\zeta_a(x_{\ell/r})}{k_{\ell/r}(x_{\ell/r})} \left( \ell_a S_{\ell/r} r_p(c_0) + \frac{\ell_a S_{\ell/r} r_1}{P_0} |P(t)| \right) \quad (3.52)$$

Since to leading order  $\zeta_a(x_{\ell/r})/k_{\ell/r}(x_{\ell/r}) \propto \zeta_a(x_{\ell/r})^2$  (Eq. (3.23)) and  $\zeta_a \propto k'_b$ , we then get to leading order

$$L_p \propto k'_b{}^2. \quad (3.53)$$

Hence, on stiffer substrates, cells form shorter protrusions. The length of the protrusion together with the adhesive friction controls the retrograde retrograde flow velocity as  $v_r \propto L_p/\zeta_a$  (Eqs. (3.17) and (3.22)), which leads to

$$v_r \propto k'_b. \quad (3.54)$$

Thus, based on our model, we would expect that also the retrograde flow is reduced on softer substrates. As a consequence, we expect that the diffusive term in Eq. (3.30) is strongly suppressed with increasing stiffness, since the rescaled diffusion constant scales as  $D \propto k'_b{}^{-2}$ . At the same time, the advective contribution, which reinforces polarization, is increased on stiffer substrates (Eq. (3.54)). Noticeably, the polarization dynamics couple thus even stronger to the substrate stiffness than the rescaled spring constants.

To get an intuition for the effect of the coupling between substrate stiffness and polarization dynamics, we account for this in a simplistic way, by keeping the rescaled spring constants fixed and simulate our model with simplified, stiffness dependent polarization dynamics given by

$$\dot{P} = -\alpha(k_s)P + \sigma\xi(t), \quad (3.55)$$

with  $\alpha > 0$  for simplicity. Similar to the discussion of the purely mechanical durotaxis mechanism, we simulate cells on a substrate with a sharp transition from soft to stiff at  $x_n = 0$ , which we implement by increasing  $\alpha$ , when cells are in the soft region relative to the value in the stiff region. Even with stiffness independent rescaled spring constants, the polarization dynamics give rise to durotaxis (Fig. 3.20A, B). The dynamics of the probability density of the cell positions appear however to be qualitatively different to the purely mechanical mechanism: While for stiffness dependent rescaled spring constants, we observed a translocation of the peak of the distribution towards the stiffer region (Figs. 3.18B and 3.19B), for polarity driven durotaxis, we observe the formation of a pronounced, but localized peak in the soft region and a spread out distribution on the stiffer side (Fig. 3.20B) resulting however in a similar translocation of the average position over time (Figs. 3.18A and 3.20B). We also observe a stronger increase in persistence time and cell speed with increasing stiffness in the case of polarity driven protrusion (Fig. 3.20C, D).

Overall, we find however that both mechanisms result in durotaxis and stiffness dependent migration persistence, consistent with the phenomenological model in Novikova *et al.*, 2017. They seem to differ however quantitatively and in the case of cell speed even qualitatively in the stiffness dependence of the persistence time and average cell speed. A more detailed analysis of the different models will however be needed to ensure that these differences are intrinsic to the different models and not artefacts of the selected parameter values. The experimental evidence for a strong coupling between cell persistence and substrate stiffness (House *et al.*, 2009; Missirlis *et al.*, 2014; Raab, Swift, *et al.*, 2012) might suggest that the polarity dynamics might play a significant role during single-cell durotaxis, even though both effects are likely to contribute to the overall migration behavior. However, a more detailed experimental characterization of the migration statistics and cell morphology for

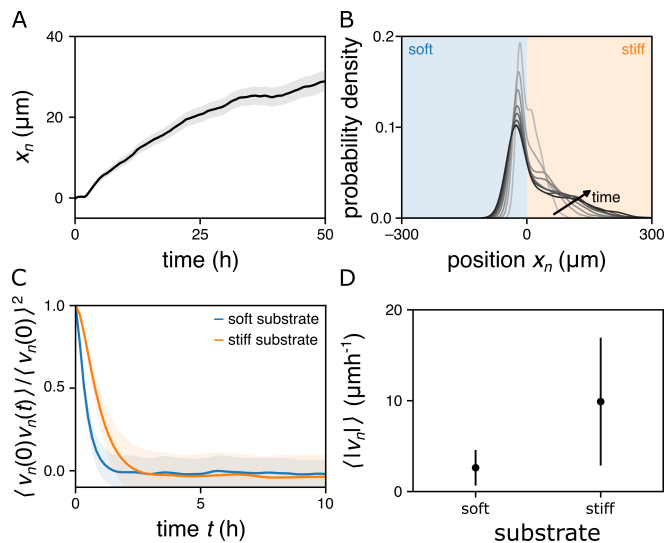


Figure 3.20: **Durotaxis with a polarity-dominated ratchetaxis mechanism.** **A.** The average nuclear position shows a comparable trend towards the stiffer region ( $x_n > 0$ ) as in Fig. 3.18. **B.** The asymmetry in the distribution of  $10^3$  cells on the substrate ( $x_n(t=0) = 0$ ) appears to be qualitatively different compared to the purely mechanical durotaxis model ( $\Delta t = 5$ h). **C.** The velocity autocorrelation on soft and stiff homogenous substrates reveals a strong increase in persistence time on the stiffer substrate. **D.** Similarly, the average cell speed is strongly increased on stiff substrates. Error bars and shaded regions indicate one standard deviation. Simulation parameters can be found in Section 3.7.

different cell lines on substrates of varying stiffness would be needed to be able to constrain reliable mechanistic and phenomenological models for single-cell durotaxis.

### 3.6 Discussion and Outlook: Towards shape and collective migration

To summarize, we developed a generalizable model for directed mesenchymal cell migration in structured microenvironments from basic biophysical principles. At the core of our model is the coupling between substrate-controlled protrusion formation and cellular migration behavior. Guided by data-driven and phenomenological models, we applied our model to explain the emergence of directed migration, stimulated by a number of different physical cues, including lateral confinement, anisotropic adhesion patterns and stiffness gradients. Beyond that, we demonstrated that our model can bridge the gap between two previously relatively separate approaches to cell migration: mechanistic bottom-up models and data-driven top-down models. This connection could benefit both approaches: It allows for a mechanistic interpretation of the observed emergent migration behavior captured by data-driven approaches and increases the generalizability of such models. On the other hand data-driven

models can be used to select the right level of complexity for a bottom-up model and could help constraining model parameters of the often times under-constrained bottom-up models.

As we demonstrated in the case of migration in lateral confinement, this connection between bottom-up and top-down model can be explicitly traced out if they are both formulated in terms of Langevin equations, with the effective underdamped dynamics of cell as a whole emerge from the interplay of a number of different internal degrees of freedom that follow overdamped dynamics. In our case, we could use an intermediate, overdamped model that was previously constrained from data (Brückner, Schmitt, *et al.*, 2022) to help bridge the gap between overdamped and underdamped description. This and other overdamped data-driven approaches (S. Amiri *et al.*, n.d.) can drastically help in identifying relevant degrees of freedom and yield more direct access to their effective dynamics. If such a model is however not available, our model can also be directly related to the emergent underdamped dynamics, by calculating the deterministic drift of the underdamped Langevin equation through

$$\begin{aligned}
 F(x_n, v_n) &= \left\langle \frac{d\dot{x}_n}{dt} \middle| x_n, v_n \right\rangle = \left\langle \frac{d\dot{x}_n}{dx_n} v_n + \frac{d\dot{x}_n}{dx_\ell} \dot{x}_\ell + \frac{d\dot{x}_n}{dx_r} \dot{x}_r \middle| x_n, v_n \right\rangle \\
 &= - \frac{k_c(x_\ell) + k_c(x_r)}{\zeta_n(x_n)} - \frac{l_a(S_l k_c(x_\ell) - S_r k_c(x_r))}{\zeta_n(x_n)} \left( r_p(c_0) + \frac{r_1}{P_0} \langle P(t) | x_n, v_n \rangle \right) \\
 &\quad - \zeta_n(x_n)^{-1} \left[ \frac{k_\ell k_c(x_\ell)}{\zeta_a(x_\ell)} (\langle x_\ell | x_n, v_n \rangle - x_n) + \frac{k_r k_c(x_r)}{\zeta_a(x_r)} (\langle x_r | x_n, v_n \rangle - x_n) \right].
 \end{aligned} \tag{3.56}$$

Even though the remaining conditional averages of  $P$ ,  $x_\ell$  and  $x_r$  have to be typically evaluated numerically, the structure of Eq. (3.56) might be able to provide an intuition for the relation between microscopic mechanism and features of the emergent migration behavior. Thus, we believe that the combination of our mechanistic model and an underdamped Langevin inference approach (Brückner, Arlt, *et al.*, 2021) can be extremely fruitful to understand cell migration in various experimental scenarios on all different levels ranging from molecular organization to emergent migration behavior. We will demonstrate one application of this in the following Chapter.

In cases where the phenomenological model is not formulated in terms of an underdamped Langevin equation, such as in the cases of ratchetaxis and durotaxis discussed here, an explicit identification of aspects of the mechanistic model and properties of the phenomenological model is more difficult. In the cases discussed here, the corresponding models were formulated in terms of discrete and continuous persistent random walks. Since also an underdamped Langevin equation leads to some kind of persistent random motion, this allows at least a heuristic identification of different aspects of the two approaches.

So far, we focused on applying our model to describe the emergent one-dimensional, single cell migration behavior of the cell as a whole. There is however no fundamental reason, why this model could not be generalized beyond that. First, even one-dimensional models can already be informative about certain features of the cell morphology. This was previously demonstrated with related models that were able to describe the stick-slip dynamics of certain migrating cell together with other migration modes that are characterized through the cellular morphology (B. Amiri *et al.*, 2023; Sens, 2020). In

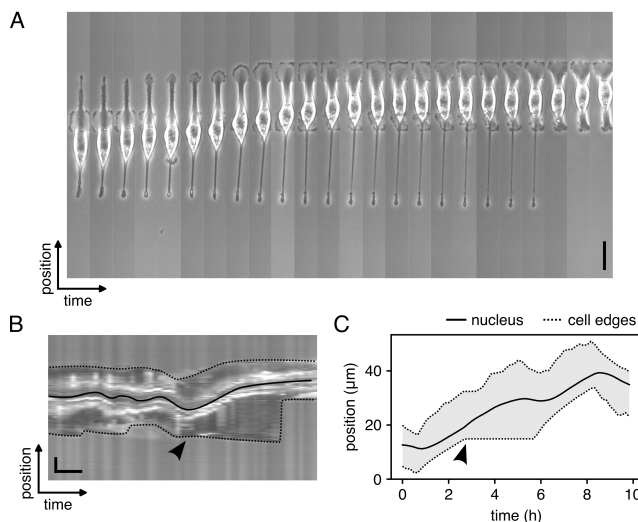


Figure 3.21: **Possible effects of myosin unbinding cascades** (taken from Flommersfeld *et al.*, 2023). **A.** Time series of a MDA-MB-231 cell with dysfunctional rear contractility (scale bar:  $50\mu\text{m}$ , time interval: 10min). **B.** The corresponding kymograph (horizontal scale bar: 1h, vertical scale bar:  $50\mu\text{m}$ ). **C.** Simulated kymograph with a model that accounts for load-dependent myosin unbinding cascades. All other parameters are identical to the ones used to model MDA-MB-231 cells on island chains of high adhesiveness. The arrow in B. and C. indicates the time point of rear contraction failure.

the context of our model, we discuss in Flommersfeld *et al.*, 2023 how force-sensitive unbinding of myosin motors can give rise to rear retraction failure that is associated with a characteristic morphology that we could also occasionally observe experimentally (Fig. 3.21). This demonstrates the potential of our and related mechanistic models can be used to relate morphological features of migrating cells to underlying molecular processes. Even more morphological features could be captured through two-dimensional generalizations of the model. Such a 2D generalization of a purely mechanical model was recently published in Chen *et al.*, 2023 and could form the basis of a generalization of our model by also accounting for the polarization dynamics.

Finally, our model could also be informative about the interactions between migrating cells and consequently collective migration. Experimentally, when migrating cells encounter each other in a confined environment, three distinct outcomes can be observed (Brückner, Arlt, *et al.*, 2021): both cells reverse upon collision and migrate away from each other, only one cell reverses its direction of motion with the other cell following this cell, and finally both cells sliding past each other while keeping their direction of migration. The statistics of and the dynamics during these events vary however between different cell lines. Here, we want to briefly discuss how these collision outcomes could emerge from the basic components of our model and how we expect differences in the adhesiveness of cells to other cells to affect the statistics and dynamics of the different outcomes. For simplicity, we start with cells that

do not adhere to each other such that their interactions are simply based on excluded volume interactions (Fig. 3.22). In that case, if two cells collide in a confined environment, we expect that based on the geometry of the collision two distinct mechanisms affect the dynamics of the leading protrusions of the cells. Where the protrusions do not directly collide, the protrusions can grow past the other cell but are now laterally confined by the other cell. Based on our model, we would thus expect that this confinement stimulates protrusion growth resulting in the cells getting accelerated past each other. Such an acceleration during sliding events was indeed observed for cells with low expression of cell-cell adhesion molecules (Brückner, Arlt, *et al.*, 2021). Where the two protrusion collide head on however, the polymerization force generated by the other cell, will oppose the actin polymerization at the front of the protrusion. Hence, the probability that a sufficiently large gap between the filament tip and the membrane opens up is reduced resulting in a lower polymerization rate in the leading protrusions upon collision. If this effect is strong enough, the polymerization rate in the trailing protrusion will eventually overtake the polymerization in the leading protrusion, resulting in a growth of the trailing protrusion and subsequently a repolarization of the cells. In a scenario, where the repolarization of both cells is similarly fast, this will result in a reversal of both cells and a migration away from each other. If one cell repolarizes slower than the other cell because it was e. g. more polarized before the collision, this would result to both cells migrating in the same direction after the collision and thus following each other. We thus see that our model together with simple excluded volume interactions is already able to qualitatively give rise to the observed collision events.

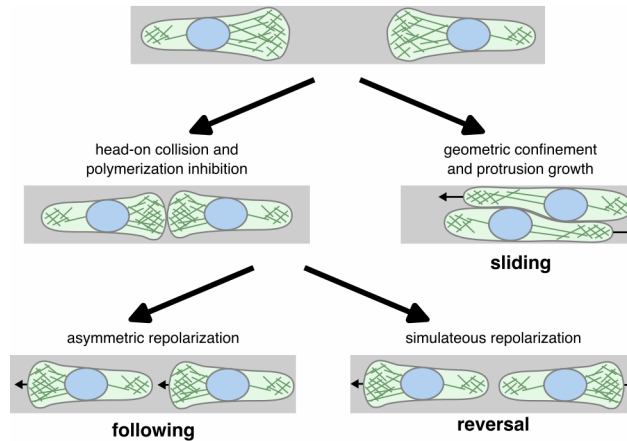


Figure 3.22: **Possible collision outcomes without cell-cell adhesions.** Based on our model and consistent with experimental observations, we expect three qualitatively different collision outcomes: following, reversal, and sliding.

A simple refinement of this model would be the introduction of cell-cell adhesions (Fig. 3.23). During sliding, this would lead to an effective friction between cells, which would counteract the confinement induced acceleration. Consistent with this, in Brückner, Arlt, *et al.*, 2021 sliding events without acceleration were observed for cells that form more cell-cell adhesions. Beyond

that, adhesions would also allow for a tug-of-war scenario upon collision and repolarization. If one cell wins this tug-of-war while still adhering to the other cell, it could drag along the loosing cell leading to an additional path to a following event upon collision. If the adhesions break however, we would obtain the same outcome as without adhesions with reversal of both cells. Based on this, we would expect that following events are more commonly observed in cells that form cell-cell adhesions, which is indeed consistent with the data in Brückner, Arlt, *et al.*, 2021.

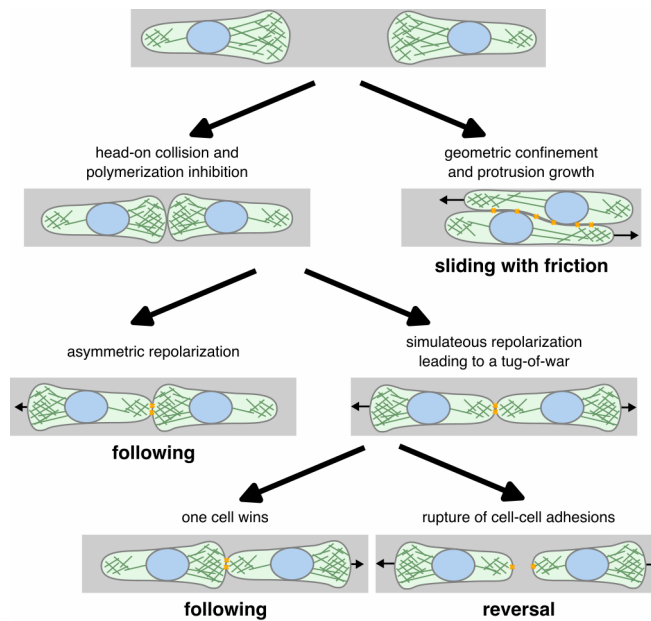


Figure 3.23: **Possible collision outcomes with cell-cell adhesions.** The addition of cell-cell adhesions adds an additional pathway for following events through a tug-of-war scenario and slows down sliding due to friction between cells.

This simple toy model for cell-cell interactions will likely reach its limits when compared quantitatively to the observed interaction behavior. Nonetheless, the qualitative agreement with experimental observations, could indicate that our model could form the basis of more refined models for interacting cells that e. g. also account for cell-cell adhesion based signaling. Overall, we believe that our model has the potential to be easily generalized to other aspects of single and collective cell migration. This applies in particular if these generalizations are guided by data-driven, top-down models for cell migration, where our model can give valuable insights into the physical mechanisms underlying the migration phenomenology.

### 3.7 Appendix: Simulation details on compliant substrates

To simulate our model on compliant substrates of different stiffness, we simulated Eqs. (3.23), (3.24), and (3.55) with the stiffness dependent parameters shown in Table 3.1. For the simulations on substrates of varying stiffness, we used the parameters corresponding to the stiff substrate for  $x > 0$  and the parameters corresponding to soft substrates for  $x < 0$ , with  $x \in \{x_n, x_p, x_\ell\}$ . We initialized  $N = 10^3$  cells at  $x_n = 0$ , with random polarization and simulated them for 50h. If cells overlapped with both regions, we used the parameter values corresponding to the soft substrate for  $k_\ell/\zeta_a$  and  $k_c(x_\ell)/\zeta_n$  and the parameter values for the stiff substrate for  $k_r/\zeta_a$  and  $k_c(x_r)/\zeta_n$ . For the polarity-dominated durotaxis model, we used  $\alpha = (\alpha_{\text{soft}} + \alpha_{\text{stiff}})/2$  when cells overlapped with both regions. To determine the persistence time and average cell speed on soft and stiff substrates, we simulated  $N = 300$  cells on homogeneous substrates of both stiffnesses with the corresponding parameter values given in Table 3.1. The cells were initialized with random polarity.

model	mechanical (Fig. 3.18)	mechanical (Fig. 3.18)	mechanical (Fig. 3.19)	mechanical (Fig. 3.19)	polarization (Fig. 3.20)	polarization (Fig. 3.20)
substrate	stiff	soft	stiff	soft	stiff	soft
$k_{\ell/r}/\zeta_a$ ( $\text{h}^{-1}$ )	1.0	2.2	1.0	2.2	1.4	1.4
$k_c(x_{\ell/r})/\zeta_n$ ( $\text{h}^{-1}$ )	0.5	0.8	0.45	0.9	0.6	0.6
$\ell_a r_p(c_0)$ ( $\mu\text{mh}^{-1}$ )	10	10	10	10	10	10
$\alpha$ ( $\text{h}^{-1}$ )	1.5	1.5	1.5	1.5	1.5	10
$\sigma$ ( $\mu\text{mh}^{-3/2}$ )	100	100	100	100	100	100
$\ell_a r_1 P_0^{-1}$	1	1	1	1	1	1

Table 3.1: Model parameters used to simulate migration on compliant substrates.

## The nucleus in 3D confined cell migration

In the previous chapter, we focused on cellular migration behavior on two-dimensional substrates, which is controlled by the interactions of the cellular cytoskeleton with the microenvironment. However, the observed migration behavior on 2D substrates does not directly translate to physiologically relevant conditions (Wu *et al.*, 2018). One of the key reasons for this is that *in vivo*, cells mostly migrate in complex, three-dimensional, confining environments, resulting in a different migration behavior compared to 2D systems. Three dimensional confinement affects cell migration in a two-folded way: First, even though the molecular components of the migration machinery are preserved from 2D to 3D migration, the physical confinement in 3D allows cells to utilize different migration modes (Faure-André *et al.*, 2008; Irimia *et al.*, 2007). In particular, cells can employ adhesion independent modes of migration, such as amoeboid migration, that are not possible on two-dimensional surfaces (R. J. Hawkins *et al.*, 2009; Lämmermann *et al.*, 2008; Reversat *et al.*, 2020). Second, the cell nucleus as the largest and stiffest organelle in the cell plays a crucial role in three dimensional migration, as it has to be strongly deformed for cells to migrate through narrow confinements in their environment (McGregor *et al.*, 2016). Due to the mechanical properties of the nucleus, this requires the generation of large intracellular forces to translocate the nucleus. Additionally, this can even result in confinement-dependent signaling or changes in gene transcription (Kalukula *et al.*, 2022) that can strongly affect the migration behavior. Unfortunately, in most experimental systems, physical confinement of the cell and in particular the nucleus goes hand-in-hand with an adaptation of the migration mode (Faure-André *et al.*, 2008; Irimia *et al.*, 2007). This makes it challenging to disentangle these two effects of 3D confinement, which would be required to systematically generalize 2D migration models to 3D environments.

To make a step towards such a generalization of our migration model from Chapter 3, we consider a generalization of the two-state patterns discussed in Section 3.4 (Fig. 4.1): Metastatic cancer cells (MDA-MB-231) migrate within microcavities which consist of an adhesive 2D surface at the bottom and non-adhesive hydrogel side-walls of variable stiffness (for more information about the experimental details see Stöberl *et al.*, 2023). The shape of the cavity resembles the previously discussed two-state patterns with two square-shaped

chambers of either side of a narrow constriction. Note that the cells are not confined from the top but the side-walls are high enough to ensure that cells do not spill over the edge of the cavity. Since cells are not compressed from the top and the confining channel is relatively short, cells still display a mesenchymal migration mode that is driven by the formation and adhesion of a leading edge protrusion to the other chamber before the cell body is moved through the confinement (see Stöberl *et al.*, 2023 for examples of the cell morphology). Hence, this setup allows us to study the effect of cellular and nuclear confinement without altering the mode of migration compared to 2D substrates.

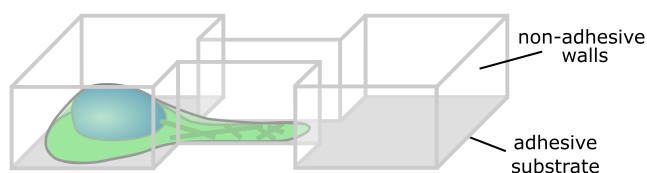


Figure 4.1: **Experimental system to study 2D mesenchymal cell migration in 3D confinement.** Cells can migrate along adhesive, fibronectin coated surfaces at the bottom of dumbbell-shaped microcavities from one chamber to the other. The side walls of the cavity are made out of non-adhesive hydrogel, with variable stiffness.

To set the stage for our analysis of this system, we first review the current literature on the role of the nucleus during confined cell migration. In particular, we focus on the role of nuclear mechanics during cell migration and discuss recent evidence for possible nuclear adaptations in confinement. While these studies correlate the overall migration ability of cells in confining environments with nuclear properties such as stiffness, a full dynamical characterization of the migration behavior in 3D confinement is still missing. As a consequence, also the interplay between nuclear confinement and the migration machinery remains largely unexplored, making it difficult to systematically constrain and test mechanistic migration models. To obtain such a dynamical characterization, we infer a dynamical model in terms of an underdamped Langevin equation for this system at varying constriction widths. With increasing confinement, we observe increasing quantitative and qualitative adaptations of the migration dynamics. The observed channel width dependence appears to be consistent with the previously proposed conceptual picture of the nucleus as a potential barrier in 3D (McGregor *et al.*, 2016; Patteson *et al.*, 2019). In contrast to this general conceptual picture however, our approach integrates the effects of nuclear deformations in a fully dynamical model. To test this interpretation of the inferred non-linear dynamics more rigorously, we aim to generalize the mechanistic model from Chapter 3 to account for three-dimensional confinement. A natural question that arises when trying to generalize this model, is through what mechanisms cells generate sufficient forces to move their nucleus into physical confinement. Since this question is a topic of debate in the literature (Davidson, Battistella, *et al.*, 2020; Keys *et al.*, 2022; McGregor *et al.*, 2016), we aim to obtain insights into this by using the observed nuclear deformations to deduce the force balance acting on the nucleus during migration.

This analysis reveals that cells adapt their force generation in confinement, resulting in a transition from a pulling-dominated to a pushing dominated translocation. Based on this, we propose a mechanistic migration model that builds up on our model for 2D migration but additionally accounts for nuclear deformations and an adaptive force generation. We show that this model can describe the channel width dependence of a number of key migration statistics and that it can successfully predict the effect of increased confinement on the non-linear migration dynamics that we found through our inference approach.

#### 4.1 The complex role of the nucleus in confinement: From physical barrier to adaptive ruler

Both in healthy processes (e.g. immune cell migration) as well as disease (e.g. cancer metastasis), cells migrate through the complex environment of the extracellular matrix (ECM) (Friedl, Wolf, *et al.*, 2011; Yamaguchi *et al.*, 2005). As cells invade this matrix, they squeeze through tight meshwork forming confinements ranging from less than 1  $\mu\text{m}$  up to tens of microns (Khatau *et al.*, 2012; Paul *et al.*, 2017). While protease-based remodeling of the ECM can help cells to overcome such constrictions, it is not required for successful migration through narrow confinements (Jill Mackarel *et al.*, 1999; Wolf *et al.*, 2007). Considering the size of the nucleus (with a typical diameter of around 10  $\mu\text{m}$ ) this highlights the intriguing ability of cells to deform their nuclei during migration. This is particularly impressive as the nucleus composes the largest and stiffest organelle in the cell (Dahl *et al.*, 2008; Lammerding, 2011).

Motivated by these striking deformations, the role of the nucleus in confined cell migration was extensively studied over the last two decades. Commonly used assays that closely mimic physiological conditions, such as migration in heterogeneous collagen matrices (Lämmermann *et al.*, 2008; Wolf *et al.*, 2007), have the limitation that they do not allow for a tight control over the degree of confinement. To overcome this, microchannel assays were employed that allow studying confined cell migration under well defined conditions (Irimia *et al.*, 2007). Different studies using such microchannel assays revealed that the mechanical properties of the cell and in particular the nucleus determine the ability of cells to migrate into these channels (Fu *et al.*, 2012; Rolli *et al.*, 2010; Rowat *et al.*, 2013). More specifically, a more detailed analysis of the migration dynamics through narrow confinement revealed that nuclear deformations are rate-limiting (Davidson, C. Denais, *et al.*, 2014; Lautscham *et al.*, 2015). How strongly the nuclear deformations hinder migration depends on the mechanical properties of the nucleus to which both the nuclear lamina as well as the chromosome content of the nucleus contribute (Fu *et al.*, 2012; Rowat *et al.*, 2013). The nuclear lamina is a dense network of intermediate filaments (lamins) that are associated with the inside of the nuclear envelope and give mechanical support to the nucleus (Dobrzynska *et al.*, 2016). Depending on the molecular makeup of this network, the nucleus displays more viscous or more elastic properties. Specifically, lamins can be divided into two groups: lamin A and lamin B. High lamin B contents result in an elastic response of the nucleus to deformations on timescale of multiple hours, while high lamin A contents lead to more irreversible deformations (Harada *et al.*, 2014). In some highly migratory cells, such as immune cells and certain invasive cancer

cell lines, lamins are down-regulated (Krause and Wolf, 2015), which allows for an easier migration through highly confined environments but can have a negative impact on the lifetime of cells due to an increased DNA damage induced by nuclear deformations (C. M. Denais *et al.*, 2016; Harada *et al.*, 2014; Raab, Gentili, *et al.*, 2016). Apart from the nuclear lamina, the chromosome organization plays a key role in determining the mechanical properties of the nucleus: Highly organized and compacted heterochromatin is stiffer than less organized, open euchromatin (Pajerowski *et al.*, 2007). Surprisingly, a reduced fraction of heterochromatin in the nucleus however results in decreased transmigration rates through confinement, which could be related to changes in the gene transcription with changing chromosome organization (Fu *et al.*, 2012). Depending on the degree of nuclear deformations, either the nuclear lamina or the chromatin organization dominates the viscoelastic response of the nucleus, with chromatin dominating the viscoelastic response at small strains and the nuclear lamina dominating at larger strains (Stephens *et al.*, 2017). This leads to complex rheological properties that can be captured in terms of models that account for those two key components of the nucleus separately (Hobson *et al.*, 2020). Overall, these studies suggest that in general the nucleus hinders migration in confined environments, the extent to which depends on its molecular makeup and the degree of chromosome condensation. Consistent with this, we find that in our experimental system the ability of cells to transition from one chamber to the other strongly decreases at narrow channel widths as visible from the dynamics of the nuclear coordinate  $x_n$  (Fig. 4.2).

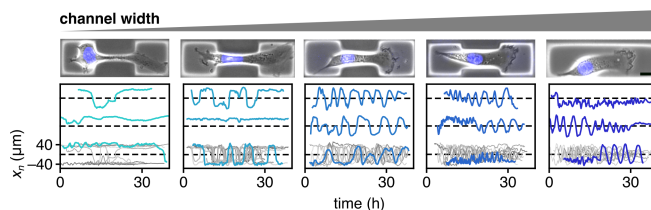


Figure 4.2: **Effect of the degree of confinement on the migration dynamics** (adapted from Stöberl *et al.*, 2023). Representative examples of cell trajectories for different channel widths (from left to right: 4  $\mu\text{m}$ , 7  $\mu\text{m}$ , 12  $\mu\text{m}$ , 20  $\mu\text{m}$  and 35  $\mu\text{m}$ ). With reducing channel width, cells spend more and more time in the chambers. Scale bar: 20  $\mu\text{m}$ .

So far we have focused on the role of the nucleus during confined cell migration as a passive cargo that needs to be transported along. Recent evidence however suggests that the nucleus takes a much more active role during cell migration and might even adapt its mechanical properties to confinement. In dendritic cells the accumulation of a perinuclear actin network can be observed when cells move their nucleus into confinement (Thiam *et al.*, 2016). This network causes a transient rupture of the nuclear lamina, which could facilitate the deformation of the nucleus. Consistent with this, cells that did display this confinement induced actin accumulation or displayed it at a location away from the nucleus showed a reduced ability to migrate through the confinement. Beyond the case of highly specialized dendritic cells, recent AFM measurements of the stiffness of cancer cells that migrate in confinement indicate that these

cells soften in confinement (Rianna *et al.*, 2020). A distinction between the contribution of the nucleus and the cytoskeleton to this softening is however difficult. Another possible nuclear adaptation mechanism that was speculated on based on theoretical arguments, would be a confinement induced reduction in nuclear volume due to water outflux through pores in the nuclear envelope (Cao *et al.*, 2016). A precise, dynamic quantification of nuclear volumes has however proven to be challenging, such that so far it remains unclear if such a volume adaptation occurs in migrating cells and how significant it is (Davidson, Sliz, *et al.*, 2015). Apart from these confinement-induced adaptations of the nuclear properties, the nucleus could also play an active role in sensing confinement and triggering changes in the cytoskeletal activity. Such a coupling between nuclear deformation and cytoskeletal activity was recently observed upon compressing cells from the top with flat silicon microcantilevers down to a well-controlled height (Lomakin *et al.*, 2020; Venturini *et al.*, 2020). Below a certain threshold height, cells displayed an active response to the compression by an increased cortex contractility. This coupling between nuclear deformation and actomyosin contractility is caused by a release of  $\text{Ca}^{2+}$  that is triggered by an increased tension in the nuclear membrane due to a confinement induced increase in nuclear surface area. In these experiments, the confinement was however externally induced, such that it remains an open question if such a coupling between nuclear shape and cytoskeletal activity also plays a role during self-imposed confinement, where cells migrate by themselves into a constriction.

Overall, we see that the nucleus plays a crucial role in 3D confined cell migration with its complex rheological properties, potential confinement adaptation and its role in measuring the degree of confinement. It has to be stated however that in particular the evidence for a stiffness adaptation and the function of the nucleus as a “ruler” for confinement have so far only been shown for specific cell lines, making it unclear how general this phenomena are. Additionally, despite recent progress in that direction (such as in Rianna *et al.*, 2020 and Davidson, Sliz, *et al.*, 2015), dynamical measurements of the nuclear properties of migrating cells in confinement are still rare. Hence, much of which is known about the mechanical properties of the nucleus stems from experiments performed with isolated nuclei which is oblivious to possible interactions between the nucleus and the cytoskeleton. This makes it challenging to choose the right level of description for the nucleus in the context of confined cell migration.

## 4.2 Inferring a data-driven model for cell migration in physical confinement

To get a better idea for how the nucleus effects the overall migration behavior in confinement, we follow the approach introduced in Chapter 3 of using data-driven, top-down models to guide the construction of more mechanistic, bottom-up models. While for the case of 2D migration, detailed, data-driven models for the emergent migration behavior were already available, this is not the case for migration in 3D confinement. Existing phenomenological models typically focus on the role of the nucleus as an effective potential barrier that needs to be overcome during migration (McGregor *et al.*, 2016). Even though this can even be used to correctly describe the reduced migration ability at

increased nuclear strains (Patteson *et al.*, 2019) this approach neglects the interplay between the nucleus and the complex, geometry-dependent migration machinery. Hence, a full dynamical, data-driven characterization of the overall migration behavior in 3D confinement is still lacking.

As discussed in Section 3.1, the dynamics of the nucleus of a migrating cell along the long axis of two-dimensional two-state patterns can be captured in terms of the underdamped Langevin equation (Brückner, Fink, Schreiber, *et al.*, 2019)

$$\frac{dv_n}{dt} = F_w(x_n, v_n) + \sigma_w \xi(t). \quad (4.1)$$

Here,  $F_w(x_n, v_n)$  captures how the deterministic acceleration of the nucleus depends on its position  $x_n$  and velocity  $v_n$  in a confinement of width  $w$ , and the Gaussian white noise  $\xi(t)$  of strength  $\sigma_w$  accounts for the stochastic nature of cell migration. Here, we apply this approach to our three-dimensional generalization of the two-state patterns to obtain a systematically constrained top-down model of confined cell migration that captures the full migration dynamics at varying confinement widths. Since the experimental procedure results in a broad range of channel widths, we bin the data with respect to the measured width of the pattern in the centre of the channel. That way, we have sufficient data for each considered channel width to constrain the terms in Eq. (4.1) (the bins and the corresponding statistics can be found in Stöberl *et al.*, 2023). We then apply the Underdamped Langevin Inference (ULI) algorithm (Brückner, Ronceray, *et al.*, 2020) to infer an estimator of  $F_w(x_n, v_n)$  from experimental trajectories. This algorithm is based on a truncated expansion of the deterministic drift  $F_w(x_n, v_n)$  in terms of  $N$  manually chosen basis functions  $\hat{c}_\alpha(x_n, v_n)$ , such that (Brückner, Ronceray, *et al.*, 2020)

$$F_w(x_n, v_n) \approx \sum_{\alpha=0}^N F_{\alpha,w} \hat{c}_\alpha(x_n, v_n). \quad (4.2)$$

The order to which this expansion is performed determines the number of parameters that have to be estimated from the data. The free parameters  $F_w^\alpha$  can be estimated by projecting the migration dynamics onto the basis functions as (Brückner, Ronceray, *et al.*, 2020)

$$F_{\alpha,w} = \langle \dot{v}_n \hat{c}_\alpha(x_n, v_n) \rangle. \quad (4.3)$$

Since ULI is a parametrized inference method, the basis functions have to be chosen manually. Specifically, the inferred estimator for the drift term  $F_w(x_n, v_n)$  and thus the accuracy of the inferred model will depend on the choice of the basis function. Here, we choose monomials in  $x_n$  and  $v_n$  as basis functions due to the simplicity and flexibility of this basis. To simplify the inference and reduce the number of unnecessary parameters in Eq. (4.2), we select the possible monomials based on symmetry considerations: The pattern is mirror symmetric with respect to both its long and its short axis. Since cells can be polarized along the long axis their orientation relative to the center of the pattern does however also affect their acceleration. To account for this, we impose that  $F_w(-x_n, -v_n) = -F_w(x_n, v_n)$  by only including monomials  $\hat{c}_{\ell,m} = x_n^\ell v_n^m$  with an odd combined order  $\ell + m$ . Without this exclusion criterium, the introduction of higher order terms in the expansion of  $F_w(x_n, v_n)$  quickly

leads to a high number of model parameters. Depending on the amount of available data, this can result in underconstrained models with fail to reproduce the experimentally observed migration behavior. As a consequence, enforcing the experimental symmetries in our basis functions allows us to capture more complex aspects of the migration dynamics that require higher order terms in the expansion of  $F_w(x_n, v_n)$ .

### Model selection

However, to infer a model, one still needs to choose the maximum orders  $\ell_{\max}$  and  $m_{\max}$  of the monomial basis functions in  $x_n$  and  $v_n$ , respectively. Depending on the chosen values of  $\ell_{\max}$  and  $m_{\max}$  the inferred non-linear dynamics might vary dramatically. Thus, ULI does not yield a unique expression for the terms in Eq. 4.1 and we require additional criteria to select a satisfying model. *A priori*, it is not even clear that there exists a unique, optimal expression for  $F_w(x_n, v_n)$ . Here, we make a leap of faith and assume that such an optimal and at least semi-unique inferred model exists. We can confirm this afterwards by comparing the structure of the different obtained models. We try to identify such optimal models by sweeping over a broad range of values for  $\ell_{\max}$  and  $m_{\max}$  and infer the corresponding models from 50% of the experimental data. This inference only utilizes the instantaneous position, velocity and acceleration of the nucleus, such that we can assess the predictive power of each model by creating a synthetic dataset by simulating Eq. (4.1) (see Stöberl *et al.*, 2023 for details) and compare the model predictions for a number of key, long-timescale statistics with the other 50% of the data that were not used during the inference. By gradually increasing the required predictive power for a model to be accepted, we then check if indeed a semi-unique, optimal model emerges for every considered geometry that can then be used to assess the impact of physical confinement on the migration dynamics.

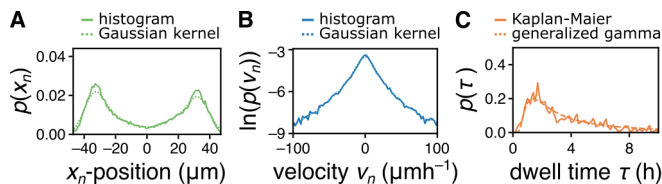


Figure 4.3: **Examples of the long-timescale statistics** (adapted from Stöberl *et al.*, 2023). **A.** The distribution of nuclear velocities together with the gaussian kernel estimate. **B.** The distribution of nuclear position together with the gaussian kernel estimate. **C.** The dwell time distribution obtained by either using a Kaplan-Maier estimator or generalized gamma distribution to estimate the survival function.

Following previous work on 2D two-state patterns (Brückner, Fink, Schreiber, *et al.*, 2019), we use the probability distribution of the nuclear position  $p(x_n)$  and velocity  $p(v_n)$  as well as the dwell time distribution  $p(\tau)$  to assess the predictive power of the inferred models (Fig. 4.3). To denoise the distributions to ensure a numerically more stable comparison between the inferred models and experimental data, we estimate  $p(x_n)$  and  $p(v_n)$  in a parameter-free way

using a kernel density estimation (Parzen, 1962; Rosenblatt, 1956) with a Gaussian kernel, which closely matches the distributions obtained from histograms (Fig. 4.3, A and B). Since the recorded trajectories are finite, a simple histogram of the dwell times would result in a biased estimate of the distribution. This can be corrected for by using a *Kaplan-Maier estimator* (Kaplan *et al.*, 1958), which allows for a parameter-free estimate of the survival function  $S(\tau)$  of a cell sitting in one chamber. The estimate of the dwell time distribution  $p(\tau)$  is given by  $p(\tau) = \partial_\tau(1 - S(\tau))$  (Fig. 4.3C). Similar to the histograms for  $p(x_n)$  and  $p(v_n)$ , the estimate for  $p(\tau)$  obtained in that way is relatively noisy, which makes a comparison between different distributions difficult. To obtain a less noise-prone estimate of the dwell time distribution, we use a parameterized estimator of the survival function by fitting a generalized gamma distribution (Stacy, 1962) to the data (Fig. 4.3C). We found a close agreement between the dwell time distributions obtained with both methods, confirming that the generalized gamma distribution is indeed a suitable parametrization of the survival function.

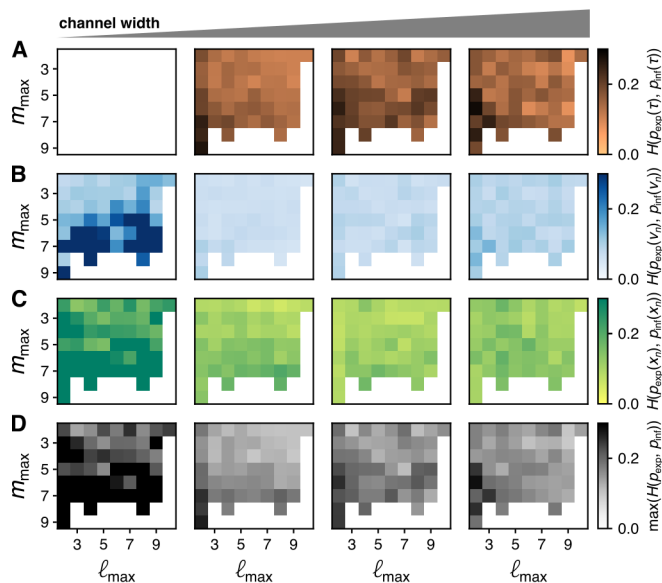


Figure 4.4: **Overview of the Hellinger distances between experimental and model statistics for models of different orders and channel widths (from left to right: 4  $\mu\text{m}$ , 7  $\mu\text{m}$ , 9  $\mu\text{m}$ , 12  $\mu\text{m}$ ) (adapted from Stöberl *et al.*, 2023).** **A.** Hellinger distances of the dwell time distributions. **B.** Hellinger distances of the velocity distributions. **C.** Hellinger distances of the position distributions. **D.** Maximum Hellinger distance of the three considered statistics.

To quantify the predictive power of the inferred model, we require a similarity measure between the predicted and the experimentally determined distributions. Since all three distributions are probability distributions, we can use the same measure for all three quantities. There is a host of measures for the similarity between probability distributions that one can choose from. The Kullback-Leibler divergence  $D_{\text{KL}}(p|q)$  between two probability distribu-

tions  $p(x)$  and  $q(x)$  of a generic random variable  $x$  (Kullback *et al.*, 1951) is potentially the most well known of such distributions and would also allow for an information theoretical interpretation of the obtained difference between distributions. In our case, the Kullback-Leibler divergence turned out to be not particularly well suited because it diverges if  $q$  is 0 for a value of  $x$  for which  $p$  is finite. We thus choose a different measure to quantify the difference between the predicted and the experimentally determined distributions, the so-called *Hellinger distance*  $H(p_{\text{exp}}, p_{\text{inf}})$  (Hellinger, 1909), with  $p_{\text{exp}}$  and  $p_{\text{inf}}$  denoting probability densities obtained from experimental data and predicted by an inferred model, respectively. The Hellinger distance is bounded to values between 0 (perfect agreement between  $p_{\text{exp}}$  and  $p_{\text{inf}}$ ) and 1 (complete disagreement between  $p_{\text{exp}}$  and  $p_{\text{inf}}$ ), which makes it numerically more stable in our case. When sweeping over  $\ell_{\text{max}}$  and  $m_{\text{max}}$ , we find that there are strong differences in the Hellinger distances and thus the performances of the inferred models (Fig. 4.4). Interestingly, we find that an increase in  $m_{\text{max}}$ , the maximal order in  $v_n$ , quickly results in models with an inferior performance compared to simpler models with lower values of  $m_{\text{max}}$ . In contrast, higher values in  $\ell_{\text{max}}$  often times leads to an increased predictive power of the inferred models, suggesting that the dynamics are more complex with respect to the positional degree of freedom than the velocity.

To select between models, we define a threshold value  $H_{\text{thresh}}$  such that models are accepted if they score a value of  $H(p_{\text{exp}}, p_{\text{inf}}) < H_{\text{thresh}}$  for all three statistics. For the narrowest considered channel width ( $w \approx 4 \mu\text{m}$ ), cells perform almost no transitions. As a consequence, the dwell time distribution can not be reliably estimated in that case and was excluded from as a selection criterium for this bridge width. Note that there will be a lower bound to  $H(p_{\text{exp}}, p_{\text{inf}}) < H_{\text{thresh}}$  due to the finite data set. We will thus not be able choose arbitrarily low values of  $H_{\text{thresh}}$ . To test if this approach can indeed be used to identify a semi-unique optimal model, we started out with a value of  $H_{\text{thresh}} = 0.15$ , which already ensures that large parts of the probability distributions are correctly predicted by the model. We found however that this criterium was not strict enough to lead to unique models, but instead found large differences for different values of  $\ell_{\text{max}}$  and  $m_{\text{max}}$ . We then gradually decreased the threshold until we obtained a selection of models that qualitatively and quantitatively agree closely for each bridge width. At a value of  $H_{\text{thresh}} = 0.14$ , we found satisfying agreement between the deterministic terms  $F_w$  of different models for some channel widths, but larger qualitative differences for other channel widths (Fig. 4.5). For a value of  $H_{\text{thresh}} = 0.13$  we found a good qualitative and quantitative agreement between accepted models for all channel widths while still being able to find models that were accurate enough to be accepted with the exception of the narrowest channel width (Fig. 4.6). For these, the inferred model was not able to reproduce the sharply peaked positional probability distributions well enough to pass the threshold. Since we are however more interested in the dynamical properties of our model, we loosened the selection criterium in that case to  $H_{\text{thresh}} = 0.14$ , which still lead to a semi-unique model. Overall, we find that with increasing predictive power, the inferred models become qualitatively and quantitatively more and more similar, indicating that there is indeed a single, unique model that describes the experimental migration behavior optimally. For the accepted models, we then chose specific values of  $\ell_{\text{max}}$  and  $m_{\text{max}}$  (see Table 4.1 and Fig. 4.7A) to

analyze the effect of confinement on the cellular dynamics. Our results do however not depend sensitively on the choice of the model as long as they pass our threshold.

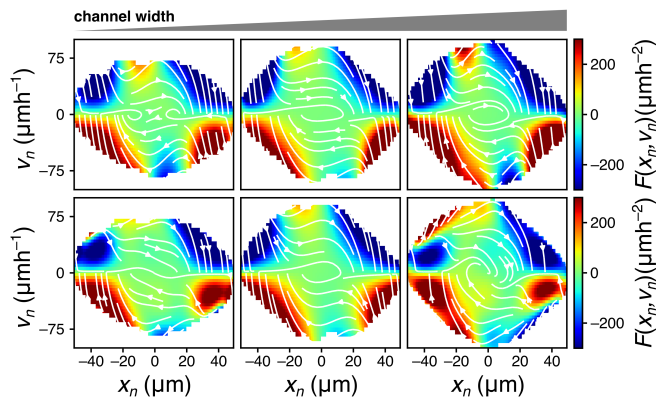


Figure 4.5: **Comparison between exemplary models with a threshold of 0.14** (adapted from Stöberl *et al.*, 2023). Shown are the bridge widths 7  $\mu\text{m}$ , 9  $\mu\text{m}$  and 12  $\mu\text{m}$ .

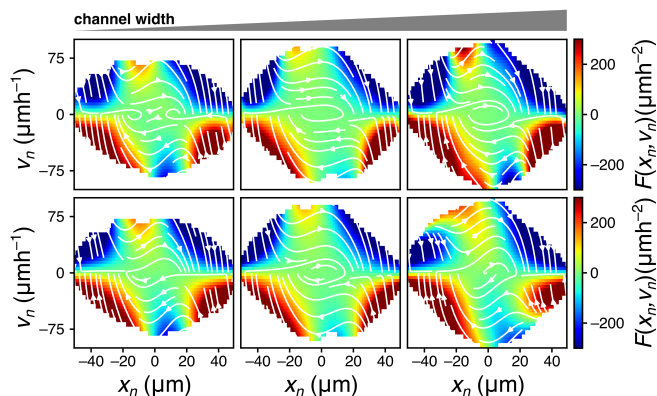


Figure 4.6: **Comparison between exemplary models with a threshold of 0.13** (adapted from Stöberl *et al.*, 2023). Shown are the bridge widths 7  $\mu\text{m}$ , 9  $\mu\text{m}$  and 12  $\mu\text{m}$ .

bridge width	4 $\mu\text{m}$	7 $\mu\text{m}$	9 $\mu\text{m}$	12 $\mu\text{m}$
$\ell_{\max}$	3	9	8	7
$m_{\max}$	2	3	2	3

Table 4.1: Orders of the basis functions used to infer the models used to analyze the effect of confinement on the migration dynamics.

### Model comparison and interpretation

To gain insight on how 3D confinement and especially nuclear deformations, affect the non-linear migration behavior of cells, we focus on channel widths of  $12\ \mu\text{m}$  and below (Fig. 4.7A), where we transition from transmigration without nuclear deformations ( $w = 12\ \mu\text{m}$ ) to strong nuclear deformations induced by the confinement ( $w < 12\ \mu\text{m}$ ). For  $w \geq 7\ \mu\text{m}$ , we find qualitatively similar models: The nucleus strongly decelerates when located near the center of the chambers. In contrast, as the nucleus approaches the constricting channel, it accelerates into the channel and transitions to the other side of the pattern. The structure of these nonlinear dynamics is at first glance reminiscent of cells migrating on corresponding 2D micropatterns (Brückner, Fink, Schreiber, *et al.*, 2019). Interestingly, at the narrowest channel width ( $4\ \mu\text{m}$ ) this region of acceleration vanishes, which is consistent with the more stationary behavior that we observed in the experimental trajectories at this channel width (Fig. 4.2). Even though we can observe some quantitative and qualitative differences between the inferred deterministic terms  $F_w(x_n, v_n)$  of the underdamped Langevin dynamics in Fig. 4.7A, it is difficult to identify a clear signature of increasing confinement from a simple visual comparison.

To help with that and to better visualize the effect of nuclear deformations on the non-linear dynamics, we compute the difference  $\langle \Delta F \rangle_w = F_{12\mu\text{m}} - F_w$  (Fig. 4.7B), which we term *Nuclear Confinement Maps* (NCM). Between all three considered channel widths, the NCMs share a number qualitative features: Cells that migrate along the exemplary trajectory from the left to the right chamber indicated by the black line in Fig. 4.7 (center) start out in a region where  $\langle \Delta F \rangle_w > 0$  (circle in Fig. 4.7B, C). In previous work from our group on 2D micropatterns and as extensively discussed in Section 3.4, we found that increasing confinement of the protrusion stimulates increasing protrusion growth and thus stronger accelerations of the nucleus towards the channel (Brückner, Schmitt, *et al.*, 2022). The pronounced region of  $\langle \Delta F \rangle_w > 0$  in the chambers could indicate that this *geometry adaptation* mechanism is also present in 3D confinement. Once the nucleus approaches the channel entrance (triangle in Fig. 4.7B, C), it crosses over into a region of  $\langle \Delta F \rangle_w < 0$  in the NCM. Since the region of  $\langle \Delta F \rangle_w < 0$  coincides with the point at which further translocation of the nucleus would require large nuclear deformations, this suggests that this feature of the NCM may be due to an effective deformation energy barrier that impedes entry into the channel. Once the nucleus transitioned into the channel (square in Fig. 4.7B, C), we again observe a region of acceleration that is consistent with an elastic release of the tension that was build up to deform the nucleus in the previous step. If cells reach high enough velocities, they cross through another region of  $\langle \Delta F \rangle_w < 0$  as they move out of the channel (star in Fig. 4.7B, C). Overall, the NCMs indicate that there is a clear qualitative signature of 3D nucleus confinement that suggest that elastic deformations of the nucleus affect the transmigration dynamics. Further, while the differences between the inferred models appear to be consistent with the previously proposed interpretation that nuclear deformations act as an effective energy barrier (McGregor *et al.*, 2016), they also highlight the need to account for the coupling of the nucleus to the cellular migration and force generation machinery to explain for the complex, underdamped migration dynamics, which clearly deviate from the diffusion of an overdamped particle in

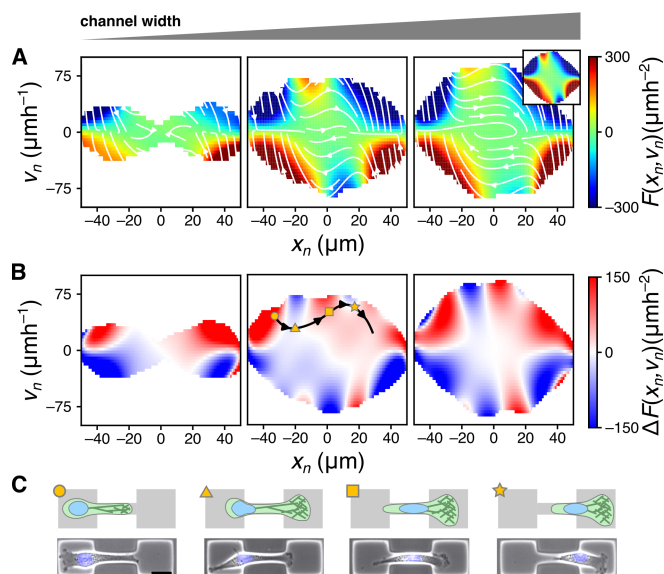


Figure 4.7: **Inferred non-linear dynamics of the nucleus for varying channel widths (from left to right: 4  $\mu\text{m}$ , 7  $\mu\text{m}$ , 9  $\mu\text{m}$ )** (adapted from Stöberl *et al.*, 2023). **A.** The inferred deterministic term  $F_w(x_n, v_n)$  within the experimentally sampled region. The unsampled region is shown in white. Central inset: Predicted deterministic dynamics obtained from simulations of the mechanistic model ( $w = 7 \mu\text{m}$ ). Right inset:  $F_w(x_n, v_n)$  for a channel width of 12  $\mu\text{m}$ . **B.** The difference between the deterministic term  $F_w(x_n, v_n)$  and the reference term at 12  $\mu\text{m}$  (‘Nuclear Confinement Maps’). The black line indicates an exemplary trajectory of a transitioning cell. Inset: Predicted confinement signature map obtained from simulations of the mechanistic model (7  $\mu\text{m}$ ). **C.** Snapshots of the typical cellular morphology at different points during the transition indicated in (B). Scale bar: 20  $\mu\text{m}$ .

a double-well potential as proposed previously in Patteson *et al.*, 2019.

### 4.3 Cellular force generation and the nucleus: Is it pulled or is it pushed?

While the inferred underdamped dynamics of the nucleus give us some indication of the role of the nucleus in 3D confined cell migration, more information on the mechanical properties and the interaction between the nucleus and the cellular migration machinery is needed to constrain a mechanistic model for mesenchymal cell migration in 3D confinement. In particular, a key question in this context is how cells generate sufficient forces to move their nuclei into confinement. Both *pulling* forces generated in front of the nucleus and *pushing* forces generated in the cell rear have been shown to play a role in confined cell migration. Studies on embryonic mouse fibroblasts squeezing their nuclei through narrow constrictions indicate that these cells translocate their nucleus predominantly through actomyosin contractile forces that are gener-

ated in front of the nucleus (Cao *et al.*, 2016; Davidson, Battistella, *et al.*, 2020). This conclusion is based on both theoretical considerations as well as direct experimental evidence. First, analysis of the observed nuclear shapes found that their pronounced hour-glass shape when moving through the confinement (Davidson, Sliz, *et al.*, 2015) is consistent with simulations of a nucleus that is pulled through an equivalent constriction (Cao *et al.*, 2016). There, the nucleus is modeled as a hyperelastic shell with a poroelastic core. Second, laser cutting of the cytoskeleton in front of the nucleus of a cell migrating into confinement resulted in a clear retraction of the nucleus towards the cell rear, indicating the release of a contractile tension in the front upon cutting. In contrast, laser cutting in the cell rear did not result in a release of tension. A study with MDA-MB-231 breast cancer cells in the same experimental system however suggests a more complex picture (Thomas *et al.*, 2015). There, the role of the myosin II isoforms myosin IIA and IIB during confined migration were analyzed. While myosin IIA, which is associated with traction force generation (Jorrich *et al.*, 2013), was accumulated in front of the nucleus, myosin IIB was found to accumulate in the rear of the cell. Without myosin IIB, cells were migrating less efficient through confinement suggesting that for MDA-MB-231 cells forces generated in the rear of the cell play a significant role during confined migration. Beyond that, dendritic cells were found to be able to move their nuclei through narrow confinement without being able to form adhesions with their leading protrusion (Thiam *et al.*, 2016). This indicates that even without being able to generate pulling forces due to the lack of focal adhesions at the leading edge of the cell, these cells are able to generate sufficient forces to deform their nucleus and move through the constriction. More recently, two preprints analyzed the mechanism behind rear contractility driven nuclear translocation in more detail (Ju, Falconer, Dean, *et al.*, 2022; Keys *et al.*, 2022). In Keys *et al.*, 2022 a classification of migrating cells in *cortex-driven* and *non-cortex-driven* migration is performed based on the cellular morphology. Here, *cortex-driven* corresponds to a force generation mode where pushing forces play a significant role, while *non-cortex-driven* migration is thought to be dominated by pulling forces. Consistent with the literature that we discussed above, they found that under strong confinement the migration of mouse embryonic fibroblasts was *non-cortex-driven*, while the migration of MDA-MB-231 and HT-1080 cells was *cortex-driven* migration. In the absence of confinement all three cell lines displayed a morphology consistent with *non-cortex-driven* migration. Similarly, in Ju, Falconer, Dean, *et al.*, 2022 indications for a confinement induced rear contractility were found for a different cancer cell line (1205Lu cells). Both studies suggest that nuclear deformations are a key requisite for increased rear contractility, which could be explained by the mechanism discovered in Lomakin *et al.*, 2020 and Venturini *et al.*, 2020 that nuclear deformations trigger an increased  $\text{Ca}^{2+}$  release and consequent cortical contractility.

Overall, these studies suggest that a mechanistic model for 3D confined cell migration does not only have to account for the mechanical properties of the nucleus but would also need to consider two distinct force generation mechanisms that might be connected to nuclear deformations. Despite the mounting evidence that such distinct mechanisms exist and both play a role in many instances of confined cell migration, a quantitative understanding the interplay between confinement and these force generation mechanisms is still

lacking, which would be crucial for a model that can describe migration at varying degrees of 3D confinement.

### The nucleus as a force sensor

To obtain quantitative information on the dependence of the cellular force generation on the degree of confinement, we use that the nuclear shape is dictated by the forces that propel it through confinement. Previously, nuclear shapes were used to infer the complete force distribution along the outline of the nucleus (Estabrook *et al.*, 2021). Here, we are only interested in the overall balance between pulling and pushing forces such that we use a simplified version of the same rationale. At the heart of any method that relates shapes to forces lies a model for the mechanical properties of the deformed object. Even though the cell nucleus displays rich and complex rheological properties as discussed in Section 4.1, it is unclear how much of this complexity contributes on the length and time scales that we are interested. Apart from the mechanical properties of the isolated nucleus, it is also unclear if possible adaptation mechanisms play a role in our system. As a consequence, we first need to measure the mechanical properties of the nucleus in confinement in our system before being able to relate the observed nuclear deformations to cellular force generation.

For that, we utilize a key feature of our experimental system: the control over the stiffness of the hydrogel walls. By embedding fluorescent beads in the hydrogel and choosing the wall stiffness to be close to the nuclear stiffness (see Stöberl *et al.*, 2023 for further experimental details), we can observe how the cell and specifically the nucleus deforms the substrate it transitions through the confining channel. This allows us to measure the contact force between the cell and the hydrogel. If the channel is narrow enough to induce significant nuclear deformations, this contact force should be dominated by the mechanical response of the deformed nucleus. To obtain a simple estimate of the contact force  $F_h$  from the observed deflection  $\Delta w/2$  of the side walls without relying on complex finite element simulations, we use a simple Hertz' model (Hertz, 1882; Puttock *et al.*, 1969)

$$F_h \left( \frac{\Delta w}{2} \right) = \frac{4}{3} \frac{E_h}{1 - \nu_h^2} \sqrt{R_i} \left( \frac{\Delta w}{2} \right)^{3/2}, \quad (4.4)$$

where  $R_i$  is the initial radius of the (unconfined) cell nucleus and  $E_h$  and  $\nu_h$  are the Young's modulus and Poisson's ratio of the hydrogel, respectively. At the same time, this requires the nucleus to be compressed down to a width of  $2R_c \approx w_d = w + \Delta w$ , where  $2R_c$  is the width of the compressed nucleus in the direction of compression and  $w$  and  $w_d$  denote the width of the undeformed and deformed channel, respectively. Using that the normal force generated by a compressed spherical object is given by (Hertz, 1882; Puttock *et al.*, 1969)

$$F_n(\Delta R) = \frac{4}{3} \frac{E_n}{1 - \nu_n^2} \sqrt{R_i} (\Delta R)^{3/2}, \quad (4.5)$$

with  $\Delta R = R_i - w_d/2$ . We can then estimate the expected wall deflection induced by a spherical elastic nucleus of Young's modulus  $E_n$  and Poisson

ratio  $\nu_n$  by equating Eqs. (4.4) and (4.5) as

$$\frac{\Delta w}{2} = \frac{\left(\frac{E_n}{1-\nu_n^2}\right)^{2/3}}{\left(\frac{E_h}{1-\nu_h^2}\right)^{2/3} + \left(\frac{E_n}{1-\nu_n^2}\right)^{2/3}} \left(R_i - \frac{w}{2}\right). \quad (4.6)$$

Note that Eq. (4.6) in principle allows us to determine the mechanical parameters  $\nu_n$  and  $E_n$  associated with the nucleus in this simplistic model. As discussed in Section 4.1, a more detailed analysis revealed that the rheological properties of the nucleus are more complex than that of a linear elastic sphere. In our system however, the bead displacement data does not have the same precision and deformation range as experiments with isolated nucleus. Hence, our data is only sufficient to constrain a simplistic mechanical model of the nucleus. Another simplifying assumption that goes into Eq. (4.6) is that the nuclear deformations are predominantly elastic. This is supported by the observation that nuclear shape rapidly recovers to its original round shape after exiting the channel, with a relaxation time of 20 minutes (Fig. 4.8). This observation suggests that in our set-up with relatively short time scales of deformation the nuclear response is predominantly elastic. This is consistent with relatively low lamin A levels found in MDA-MB-231 cells (Bell *et al.*, 2022), which was shown to increase the reversibility of nuclear deformations (Harada *et al.*, 2014).

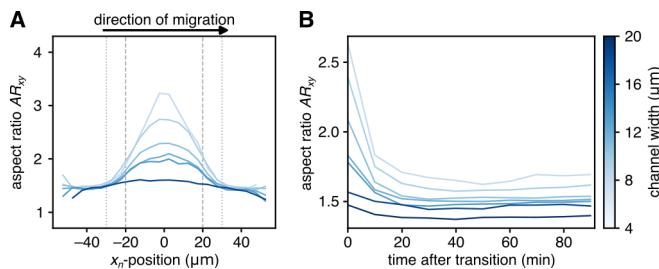


Figure 4.8: **Aspect ratio of the nucleus for different channel widths ( $x$ -dimension/ $y$ -dimension)** (taken from Stöberl *et al.*, 2023). **A.** Aspect ratio with respect to the nuclear position. The cells are oriented such that they migrate from left to right. The grey dashed lines indicate the edges of the channel and the grey dotted lines the point at which the nucleus starts entering (left)/ fully left (right) the channel. **B.** Nuclear shape recovery after a transition.

To further reduce the number of free parameters in Eq. (4.6) that we have to constrain with the bead deflection data, we aim to measure the nuclear Poisson ratio independently. For that, we quantify the volume of the nucleus as it transition from one chamber to the other by using confocal imaging (see Stöberl *et al.*, 2023 for further experimental details). This analysis revealed a temporary and repeated reduction in nuclear volume when the nucleus enters the channel, which could potentially be arise from an outflux of water through the water-permeable nuclear membrane upon compression as proposed previously (Cao *et al.*, 2016). The quantification of the nuclear volumes in and

out of confinement allows us to determine the Poisson ratio of the nucleus of MDA-MB-231 cells through (Demtröder, 2017)

$$\nu_n = \frac{1}{2} \left( 1 - \frac{\Delta V w}{V \Delta w} \right). \quad (4.7)$$

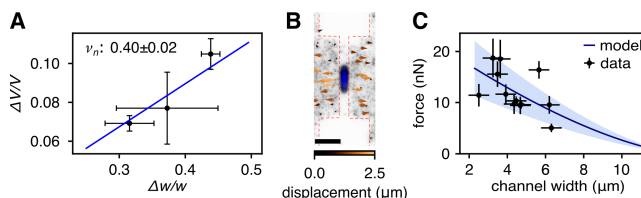


Figure 4.9: **Experimental characterization of the nuclear mechanics under confinement** (adapted from Stöberl *et al.*, 2023). **A.** Relative volume change of the nucleus when confined by the channel with three different widths (mean  $\pm$  SD for  $n > 2$  cell nuclei per channel width) together with fit of Eq. (4.7) (blue line). **B.** Exemplary snapshot of the fluorescently labeled nucleus of an MDA-MB-231 cell passing through a soft PEG-NB hydrogel channel. Color-coded arrows indicate the displacement field of fluorescent beads embedded in the hydrogel. Scale bar: 20  $\mu\text{m}$ . **C.** Normal forces between the nucleus and the hydrogel wall as a function of channel width together with the fit of our simple mechanical model for the nucleus (blue line, shaded area indicates one standard deviation).

We find that the observed volume changes at different channel widths can be explained in terms of a single, deformation-independent Poisson ratio of  $\nu_n = 0.40 \pm 0.02$  (Fig. 4.9A). Since the mechanical properties of the hydrogel are experimentally determined (Stöberl *et al.*, 2023), this leaves us with a single free parameter  $E_n$  in Eq. (4.6). Using Eq. (4.6) together with Eq. 4.4 to fit our model to the experimentally determined contact forces between nucleus and wall (Fig. 4.9B, C), we determine the value of  $E_n$  as  $E_n = 0.4\text{kPa}$ . Note that our simplistic model is sufficient to explain the observed channel width dependence of the contact forces without requiring more detailed mechanical models of the nucleus or confinement dependent values of  $E_n$ . Overall, we find that within the precision of our experimental system, the mechanical response of the nucleus to confinement is well described by a spherical elastic material with confinement independent mechanical parameters but with a Poisson ratio that results in a volume reduction upon compression.

### Relating nuclear shape to intracellular force generation

Following a similar approach to Estabrook *et al.*, 2021, we use this simple mechanical model for the nucleus (Eq. (4.5)) to deduce whether the nucleus is being predominantly *pulled* or *pushed* through the confinement. To obtain a first insight into the effect that external forces have on the confined nucleus in the center of the channel, we quantify the deviation from an isotropic (force free) expansion of the nucleus under compression through the channel walls. The previous quantification of the nucleus Poisson ratio allows us to use

the two-dimensional time-lapse microscopy data to obtain information on the change of  $x$ - $z$  aspect ratios ( $AR$ ) as cells move from the chamber into the channel (see Fig. 4.10A and B for the definition of  $x$ ,  $y$ ,  $z$  in our setup). To find an approximate expression for the dimensions of the nucleus under compression in the presence of pulling and pushing forces acting along the direction of migration, we first calculate the shape of the unconfined nucleus with pulling and pushing forces applied and then apply the confinement-induced deformation in the  $y$ -direction together with an isotropic expansion in the  $x/z$ -direction.

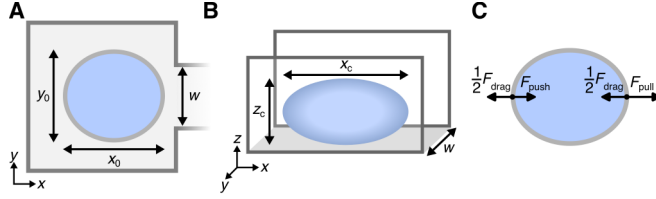


Figure 4.10: **The deformation of the nucleus** (adapted from Stöberl *et al.*, 2023). **A.** The force free nucleus. **B.** The nucleus in the channel. The observed shape is a result of lateral confinement by the channel walls and intracellular forces acting on the nucleus. **C.** Force balance on the nucleus in the direction of migration in the channel.

For this, we consider the strain  $u_{xx}$  in the  $x$ -direction induced by the sum of pushing and pulling forces acting on the nucleus. The strains in the orthogonal directions can then be written as  $u_{yy} = -\nu_n u_{xx}$  and  $u_{zz} = -\nu_n u_{xx}$  (Landau *et al.*, 1986b). For small deformations along the  $x$ -direction, the strains can be expressed as  $u_{xx} = \frac{dx}{x}$ ,  $u_{yy} = \frac{dy}{y}$ , and  $u_{zz} = \frac{dz}{z}$  (Hencky, 1928). To relate the finite deformations  $\Delta y$  and  $\Delta z$  to the deformation  $\Delta x$  induced by the forces acting in  $x$ -direction we integrate the infinitesimal strains and use that  $u_{yy} = u_{zz} = -\nu_n u_{xx}$ , such that

$$\int_{y_0}^{y_0+\Delta y} \frac{dy}{y} = \int_{z_0}^{z_0+\Delta z} \frac{dz}{z} = -\nu_n \int_{x_0}^{x_0+\Delta x} \frac{dx}{x}. \quad (4.8)$$

From that, we get

$$\frac{y_0 + \Delta y}{y_0} = \frac{z_0 + \Delta z}{z_0} = \left( \frac{x_0 + \Delta x}{x_0} \right)^{-\nu_n}. \quad (4.9)$$

Writing the deformation of the nucleus in the  $x$ -direction induced by the combination of pulling and pushing forces as  $\Delta x_{\text{forces}}$ , such that the new length of the nucleus is  $x_{\text{forces}} = x_0 + \Delta x_{\text{forces}}$ , we can then use Eq. (4.9) to write the corresponding nuclear dimensions in the orthogonal directions as

$$y_{\text{forces}} = y_0 + \Delta y_{\text{forces}} = y_0 \left( 1 + \frac{\Delta x_{\text{forces}}}{x_0} \right)^{-\nu_n} \quad (4.10)$$

and

$$z_{\text{forces}} = z_0 + \Delta z_{\text{forces}} = z_0 \left( 1 + \frac{\Delta x_{\text{forces}}}{x_0} \right)^{-\nu_n}, \quad (4.11)$$

where  $x_0/y_0/z_0$  denote the force-free dimensions of the nucleus.

Now we add the confinement due to the channel of width  $w$ , such that the width of the nucleus in the channel  $y_c = w$ . Consequently, the dimensions of the nucleus in the other directions in the channel are given by

$$x_c = x_{\text{forces}} \left( \frac{w}{y_{\text{forces}}} \right)^{-\nu_n} \quad (4.12)$$

and

$$z_c = z_{\text{forces}} \left( \frac{w}{y_{\text{forces}}} \right)^{-\nu_n}. \quad (4.13)$$

The aspect ratio between the two unconfined dimensions of the nucleus in the channel is then given by

$$AR_{\text{confined}} = \frac{x_c}{z_c} = \frac{x_0}{z_0} \left( \frac{x_{\text{forces}}}{x_0} \right)^{1+\nu_n}. \quad (4.14)$$

If the pulling force is stronger than the pushing force, we expect that  $\Delta x_{\text{forces}} > 0$  and thus  $AR_{\text{confined}} > x_0/z_0 = AR_{\text{free}}$ , while in the case that pushing forces are stronger than pulling forces, we expect  $\Delta x_{\text{forces}} < 0$  and thus  $AR_{\text{confined}} < AR_{\text{free}}$ . To express the effect of the intracellular force balance on the nuclear aspect ratios in a single parameter, we define the shape parameter

$$\varepsilon = \frac{AR_{\text{confined}}}{AR_{\text{free}}} = \left( \frac{x_{\text{forces}}}{x_0} \right)^{1+\nu_n}. \quad (4.15)$$

For  $\varepsilon > 1$  pulling is the dominant force driving nucleus translocation, while for  $\varepsilon < 1$  pushing dominates. Unfortunately, Eq. (4.15) cannot be used to determine  $\varepsilon$  from our experimental data, since we have no direct experimental access to  $x_{\text{forces}}$ . To express  $\varepsilon$  in terms of measurable quantities, we use that  $x_{\text{forces}} = x_c(w/y_{\text{forces}})^{\nu_n}$  and  $y_{\text{forces}} = y_0(x_{\text{forces}}/x_0)^{-\nu_n}$ . This allows us to write

$$\frac{x_{\text{forces}}}{x_0} = \left[ \frac{x_c}{x_0} \left( \frac{w}{y_0} \right)^{\nu_n} \right]^{\frac{1}{1-\nu_n^2}}. \quad (4.16)$$

Together with Eq. (4.15) we then get the following expression for the shape parameter in terms of experimentally accessible quantities:

$$\varepsilon = \left[ \frac{x_c}{x_0} \left( \frac{w}{y_0} \right)^{\nu_n} \right]^{\frac{1+\nu_n^2}{1-\nu_n^2}}. \quad (4.17)$$

We use Eq. (4.17) to characterize the experimentally observed nuclear deformations (Fig. 4.11A). Values of  $\varepsilon$  exceeding 1 indicate that in confinement the nucleus is being stretched in the direction of migration, while values below 1 indicate that the nucleus is compressed in the migration direction. In the absence of nuclear deformations ( $w \gtrsim 12 \mu\text{m}$ ),  $\varepsilon$  initially rises with increasing confinement width up to a maximal value of 1.4 at a channel width of  $12 \mu\text{m}$  (Fig. 4.11B). When transitioning into a regime where confinement induces significant nuclear deformations ( $w < 12 \mu\text{m}$ ),  $\varepsilon$  starts to decrease and eventually drops to values below 1 for channel widths below  $7 \mu\text{m}$ , where it reaches a value of 0.5 at  $4 \mu\text{m}$  confinement width. Thus, wild-type MDA-MB-231 cells show a non-monotonic dependence of the shape parameters  $\varepsilon$  with channel

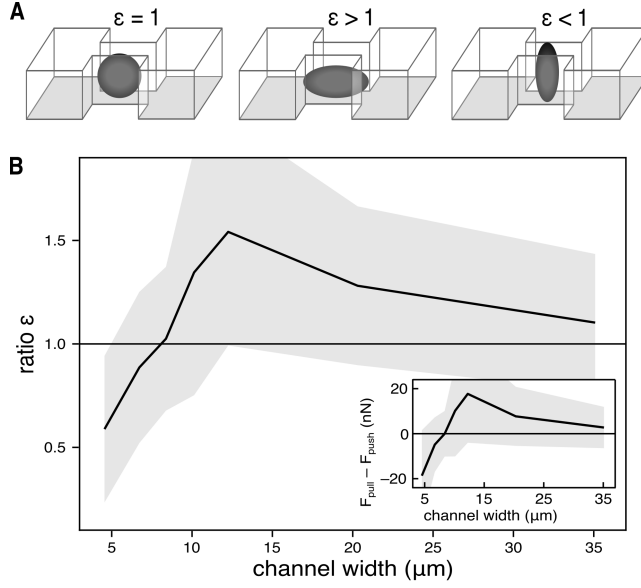


Figure 4.11: **Nuclear shapes in confinement** (taken from Stöberl *et al.*, 2023). **A.** Illustration of the shape parameter  $\varepsilon$ . At  $\varepsilon = 1$ , the nucleus expands isotropically in the two unconfined direction. At  $\varepsilon > 1$ , the nucleus displays a more elongated morphology and at  $\varepsilon < 1$ , the nucleus appears to be more compressed in the direction of migration. **B.** Values of the shape parameter  $\varepsilon$  in the channel at varying channel widths. In the absence of nuclear deformations, confinement leads to an increasingly elongated morphology. At channel widths that require nuclear deformations,  $\varepsilon$  decreases with further confinement. This change in nuclear deformations is indicative of a change in the nuclear force balance. Inset: The deduced difference between pulling and pushing forces acting on the nucleus. We observe a transition from pulling dominated to pushing dominated nuclear translocation.

width, suggesting a change in the forces acting on the nucleus with varying confinement.

To relate the observed nuclear deformations and in particular the shape parameter  $\varepsilon$  to the difference of pulling and pushing forces, we consider the force balance acting on the nucleus as it moves through the cytosol at constant speed (Fig. 4.10C). We assume that there are two contributions to these forces: a pulling force  $F_{\text{pull}}$  that is generated in front of the nucleus and a pushing force  $F_{\text{push}}$  acting from behind the nucleus. Since the drag force acts  $F_{\text{drag}}$  on the center of mass of the nucleus, we split it up with  $1/2F_{\text{drag}}$  acting on either side of the nucleus, such that overall the nucleus experiences a drag force  $F_{\text{drag}}$ . The force balances at the front and the rear of the nucleus are then given by

$$F_{\text{front}} = F_{\text{pull}} - \frac{1}{2}F_{\text{drag}} \quad (4.18)$$

and

$$F_{\text{back}} = F_{\text{push}} - \frac{1}{2}F_{\text{drag}}. \quad (4.19)$$

At a constant velocity and shape of the nucleus, the forces at the front and the back must balance out and be equal to the elastic force  $F_{\text{deform}}$  generated by the nucleus due to its deformation:

$$F_{\text{deform}} = F_{\text{front}} = -F_{\text{back}} \quad (4.20)$$

We can then rewrite  $F_{\text{deform}} = (F_{\text{front}} - F_{\text{back}})/2$  in terms of the pulling and pushing forces as

$$F_{\text{deform}} = \frac{F_{\text{pull}} - F_{\text{push}}}{2}. \quad (4.21)$$

As discussed above, the deformations of the nucleus can be approximated by the Hertz model. Here, we assume that the magnitude of the deformation force is identical whether the nucleus is compressed or stretched. This yields the following expression of the deformation force in terms of the nuclear deformation along the direction of migration:

$$F_{\text{deform}} = \text{sign}(\Delta x_{\text{forces}}) \frac{4}{3} \frac{E_n}{1 - \nu_n^2} \sqrt{\frac{x_0}{2}} \left| \frac{\Delta x_{\text{forces}}}{2} \right|^{\frac{3}{2}}. \quad (4.22)$$

Together with Eq. (4.16) the deformation force associated with a value of the shape parameter  $\varepsilon$  as

$$F_{\text{deform}} = \text{sign} \left( \varepsilon^{\frac{1}{1+\nu_n}} - 1 \right) \frac{1}{3} \frac{E_n}{1 - \nu_n^2} x_0^2 \left| \varepsilon^{\frac{1}{1+\nu_n}} - 1 \right|^{\frac{3}{2}}. \quad (4.23)$$

This expression allows us to estimate the nuclear deformation forces from the experimentally observed nuclear shapes as shown in Fig. 4.11B (inset). From this, we find that our mechanical nucleus model indicates that the change in the nuclear deformation behavior with changing channel widths is the consequence of a transition from a pulling-dominated migration regime at wider channel widths to a pushing-dominated migration regime at channel widths below 7  $\mu\text{m}$ . Thus, at least for MDA-MB-231 cells, the relative contribution of pulling and pushing forces to the translocation of the nucleus is not an intrinsic property of the cell itself, but adapts to the degree of three-dimensional confinement. This gives a new perspective on the debate about pulling and pushing forces in confined migration and could at least partially explain the seemingly conflicting results on whether pulling or pushing forces are responsible for nuclear translocation.

#### 4.4 Constraining a predictive, mechanistic model for cell migration in 3D confinement

We use the combination of the observed nuclear deformations together and the migration dynamics to constrain and test a mechanistic model for mesenchymal cell migration in 3D confinement. Motivated by the observed change in nuclear deformations with increasing confinement, we develop a model for cellular force generation during confined migration. The key aspect of the model is the combination of two confinement-dependent force generation mechanisms: pulling forces, generated by actomyosin contractility at the front of the cell, and pushing forces, regulated by the cortical tension in the rear. We incorporate these two mechanisms by generalizing a simple dynamical model that describes mesenchymal cell migration on 2D substrates (Brückner, Schmitt, *et al.*, 2022) to 3D by including nuclear deformations in confinement.

### A mechanistic model for cell migration in 3D confinement

As a basis, we use the mechanistic model from Brückner, Schmitt, *et al.*, 2022 for 2D confined migration that we derived from basic biophysical principles in Chapter 3. Here, we start by briefly summarizing the structure of the model, before discussing the adaptations made to account for the 3D nature of our experiments in more detail.

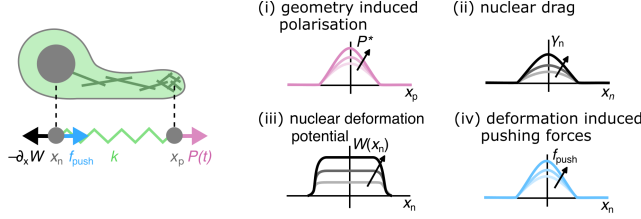


Figure 4.12: **Sketch of a minimal mechanistic model for mesenchymal cell migration** (adapted from Stöberl *et al.*, 2023). The protrusion and the nucleus are coupled elastically. Narrow confinement of the protrusion stimulates cell polarization (i). On the other hand it also increases the nuclear drag (ii) and induces nuclear deformations (iii). To overcome this migration challenge, cells can generate pushing forces (iv) that are triggered by nuclear deformations.

The model consists of three degrees of freedom: the nuclear position, the position of the leading protrusion of the cell, and a polarization (Fig. 4.12). The nucleus and the protrusion are coupled through an elastic spring of spring constant  $k$ . After absorbing the friction coefficients of the nucleus and the protrusion into the spring constants, we denote the rescaled spring constants as  $k_n$  and  $k_p$ , respectively. The nuclear dynamics are then given by

$$\gamma(x_n)\dot{x}_n = k_n(x_p - x_n) + f_{\text{push}}(x_n) + f_{\text{channel}}(x_n). \quad (4.24)$$

Here,  $\gamma(x_n)$  accounts for spatial variations in the nuclear friction coefficient (see discussion below). To account for the 3D nature of our experimental system, we include two additional terms in Eq. (4.24) compared to the model discussed in Chapter 3:  $f_{\text{push}}(x_n)$  denotes the pushing force generated by rear contractions of the cell and  $f_{\text{channel}}(x_n)$  accounts for nuclear deformations induced by the channel. The dynamics of the protrusion coordinate remain unchanged from 2D migration and are given by (see Section (Brückner, Schmitt, *et al.*, 2022)

$$\dot{x}_p = -k_p(x_p - x_n) - \partial_{x_p} V(x_p) + rP(t). \quad (4.25)$$

Here, the repulsive potential  $V(x_p) = (x_p/x_{\text{boundary}})^8$  limits protrusion formation to the region of the dumbbell-shaped micro-cavities. Additionally, to account for the internal organization of the cell, a polarization force  $P(t)$  acts on the protrusion coordinate driving protrusion formation in the direction of polarization. As derived in Chapter 3, the polarization force is sensitive to the geometry of the pattern and evolves according to

$$\dot{P} = -\alpha(x_p)P - \beta P^3 + \sigma\xi(t). \quad (4.26)$$

Here, the geometry sensitive parameter determines the value of the stable fixed point  $P^*$  of  $P(t)$  with  $P^* = \pm\sqrt{-\alpha/\beta}$  for  $\alpha < 0$  and  $P^* = 0$  for  $\alpha \geq 0$ . The constant  $\beta > 0$  ensures that  $P(t)$  remains bounded at all times. The term  $\sigma\xi(t)$  denotes a Gaussian white noise-process of strength  $\sigma$  and with  $\langle\xi(t)\rangle = 0$  and  $\langle\xi(t)\xi(t')\rangle = \delta(t - t')$  that accounts for stochastic fluctuations in the internal organization of the cell. To account for the increased confinement in the centre of the pattern (Fig. 4.13 (ii)), we gradually decrease  $\alpha$  towards the center of the pattern according to

$$\alpha(x_p) = \begin{cases} \alpha^{\min} + \frac{\alpha_0 - \alpha^{\min}}{2} \left(1 - \cos\left(\frac{x_p\pi}{L_\alpha}\right)\right), & |x_p| < L_\alpha \\ \alpha_0, & \text{else} \end{cases}, \quad (4.27)$$

where  $2L_\alpha$  is the region in the center of the pattern in which the polarization dynamics are affected by the confinement. The parameter  $\alpha^{\min}$  decreases with decreasing bridge width as (see Chapter 3)

$$\alpha^{\min} = -\alpha_1 + \alpha_2 w^2, \quad (4.28)$$

such that for narrow channels, cells display a finite average polarization when their protrusion coordinate is near the center of the pattern (Fig. 4.12 (i)). For channel widths beyond the unconfined width of the cell  $w_{\text{free}}$ , we expect the channel width to have no effect on the experiment. Hence, that in that regime we choose  $\alpha^{\min} = \alpha_0$ .

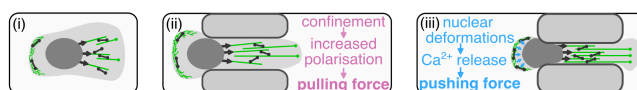


Figure 4.13: **Sketch of the proposed effect of the degree confinement on the cellular force production mechanisms** (adapted from Stöberl *et al.*, 2023). Compared to the unconfined case (i), confinement of the protrusion (ii) stimulates protrusion growth resulting in an increased pulling force. On the other hand, narrower protrusions contain less actomyosin, resulting in a reduction of the pulling force. Strong deformations of the nucleus (iii) trigger  $\text{Ca}^{2+}$  release, which results in a higher cortical contractility. Consequently, the pressure in the rear of the cell increases, resulting in an increased pushing force onto the nucleus.

The first adaptation required to account for 3D confinement in our model concerns the nuclear friction (Fig. 4.12 (ii)). Without deformations, we found that the nuclear friction is reduced in the centre of dumbbell shaped patterns due to the reduced number of focal adhesions in the constriction (see discussion in Section 3.4). In the presence of physical walls that strongly confine the nucleus, however, we expect that the nuclear friction increases in the channel due to interactions with the walls. We account for this through the channel width dependence of the minimal friction coefficient  $\gamma^{\text{centre}}$  in the centre of the channel. If the cell is completely unconfined ( $w \geq w_{\text{free}}$ ), we simply expect  $\gamma^{\text{centre}} = 1$ . When the cell is confined but the nucleus is not deformed ( $2R_n \leq w < w_{\text{free}}$ ), we expect a linear decrease of  $\gamma^{\text{centre}}$  with channel width due to the reduced adhesive area compared to the unconfined case (Eq. (3.35)).

Finally, in the presence of nuclear deformations ( $w < 2R_n$ ), we expect a non-linear increase of the nuclear drag with reducing channel width (Chang, 1961). Taken together, we use the following expression for the nuclear friction in the channel:

$$\gamma^{\text{centre}} = \begin{cases} 1, & w > w_{\text{free}} \\ \frac{1+\gamma_1 w}{1+\gamma_1 w_{\text{free}}}, & 2R_n < w \leq w_{\text{free}} \\ \frac{1+2\gamma_1 R_n}{1+\gamma_1 w_{\text{free}}} \left(1 + \frac{\gamma_2}{w}\right), & w \leq 2R_n \end{cases} . \quad (4.29)$$

Next, we consider the force  $f_{\text{channel}}$  generated due to the elastic deformations of the nucleus as it enters and leaves the channel (Fig. 4.12 (iii)). We found from the inferred underdamped migration dynamics (Section 4.2) that the nucleus acts as a barrier, impeding migration into the channel and accelerating migration out of the channel. Thus, we account for the elastic nuclear deformations induced by the channel through a potential barrier, such that

$$f_{\text{channel}}(x_n) = -\partial_{x_n} W(x_n). \quad (4.30)$$

As the nucleus moves into the confinement, it is compressed in the orthogonal direction, which leads to a lengthening of the nucleus. The confinement exerts a force opposite to the direction of movement onto the nucleus until it has completely entered the bridge. We thus use the following expression for the potential barrier:

$$W(x) = W_{\text{max}} \begin{cases} \frac{x}{L_W} - \pi^{-1} \cos\left(\frac{\pi x}{L}\right) \sin\left(\frac{\pi x}{L}\right), & 0 < x < L \\ 0, & \text{else} \end{cases} \quad (4.31)$$

where  $L_W = L_b/2 + R_n$  with  $R_n$  being the average radius of the unconfined nucleus. Since the pattern and consequently also the potential is symmetric, we can calculate the value of the potential barrier at position  $x_n$  through  $W(x = L_W - |x_n|)$ . We thus get the channel-induced deformation force

$$f_{\text{channel}}(x_n) = -\partial_x W(x) \partial_{x_n} x|_{x=L_W-|x_n|} = \text{sign}(x_n) \partial_x W(x)|_{x=L_W-|x_n|}. \quad (4.32)$$

The observed 3/2-scaling of the nuclear normal forces with the nuclear deformations (Fig. 4.9C) represents a lower bound for the dependence of the force opposing the nuclear deformations. Since an analytic expression for the force opposing the movement of a elastic spherical object that is pushed or pulled into confinement is not available, we assume that  $f_{\text{channel}}$  follows the same 3/2-scaling, such that

$$W_{\text{max}} = W_0 (2R_n - w)^{\frac{3}{2}}. \quad (4.33)$$

Finally, we include a pushing force  $f_{\text{push}}$  in our model for 3D confined cell migration (Fig. 4.13 (iii)). This is motivated by the observed nuclear shapes which are consistent with strong pushing forces driving nuclear translocation at narrow channel widths (see Section 4.3) together with recent evidence that nuclear deformations can trigger increases in cortical tension through  $\text{Ca}^{2+}$  release (Lomakin *et al.*, 2020; Venturini *et al.*, 2020), which allows cells to generate pushing forces to move the nucleus through narrow constrictions (Ju, Falconer, Tang, *et al.*, 2022; Keys *et al.*, 2022). In the absence of confinement, the pushing force is unlikely to play a significant role due to the unhindered fluid exchange between the front and the rear of the cell, which inhibits the buildup

of a pressure difference between the front and the rear of the cell. As cells move into the channel they gradually increase the nuclear strain. We account for this by applying an increasing pushing force opposing nuclear movement as the nucleus moves into the centre of the channel (Fig. 4.12 (iv)). This pushing force is given by

$$f_{\text{push}}(x_n) = \text{sign}(x_p - x_n) f_{\text{max}}(w) \cos\left(\frac{\pi x_n}{L_b}\right). \quad (4.34)$$

To derive an expression for  $f_{\text{max}}(w)$ , we consider the case of a nucleus that is completely confined laterally to a width  $w$ : Confinement induced pushing forces are thought to be triggered by strong nuclear deformations that lead to  $\text{Ca}^{2+}$  release and consequently increased myosin activity in the cortex (Lomakin *et al.*, 2020; Venturini *et al.*, 2020). The resulting increase in cortical tension causes a higher Laplace pressure in the rear that pushes against the nucleus. The pushing force in confinement is then proportional to the increase in cortical tension  $\Delta\tau_{\text{cortex}}$  and the projected area  $S$  of the nucleus in the plane orthogonal to the direction of migration (Cao *et al.*, 2016)

$$f_{\text{max}}(w) \propto S(w(x_n)) \Delta\tau_{\text{cortex}}. \quad (4.35)$$

We expect the dominant contribution to the bridge width dependence of  $S(w(x_n))$  to be the compression imposed by the side walls of the channel such that we can approximate the projected area of the nucleus as

$$S(w(x_n)) = S_0 \left(\frac{w(x_n)}{2R_n}\right)^{1-\nu_n}, \quad (4.36)$$

where  $S_0$  is the projected area of the undeformed nucleus.

The calcium release upon nuclear deformation is associated with stretch-sensitive calcium channels in the perinuclear endoplasmic reticulum (Lomakin *et al.*, 2020). To relate the change in  $\text{Ca}^{2+}$  concentration in the cytosol to the degree of confinement, we assume that the concentration  $n^{\text{Ca}^{2+}}$  is proportional to the fraction of open channels. We calculate this fraction with a simple mechanical model for the opening probability of stretch sensitive ion channels, which gives us (Phillips *et al.*, 2013)

$$n^{\text{Ca}^{2+}} \propto \frac{1}{1 + \exp\left(\frac{\Delta E - \Delta A \tau_{\text{ER}}}{k_B T}\right)}, \quad (4.37)$$

where  $\Delta E$  is the energy difference between the opened and closed state of the calcium channel and  $\Delta A$  denotes the change in channel area upon opening, in response to the tension in the perinuclear endoplasmic reticulum  $\tau_{\text{ER}}$ . We assume a linear scaling of  $\tau_{\text{ER}}$  with the nuclear deformation  $2R_n - w(x_n)$  to leading order. In the range of nuclear deformations probed in our experiments, we expect the exponential part of the sigmoidal function in the previous equation to dominate, such that

$$n^{\text{Ca}^{2+}} \propto e^{-\frac{\Delta E}{k_B T}} e^{\frac{\Delta A \tau_1 (2R_n - w(x_n))}{k_B T}}, \quad (4.38)$$

where the prefactor  $\tau_1$  is a parameter from the expansion of  $\tau_{\text{ER}}$ . This expansion is supported by measurements of the cortical myosin concentration

under confinement in primary progenitor stem cells cultured from zebrafish embryos (Venturini *et al.*, 2020), which probed confinement heights down to 7  $\mu\text{m}$  without observing a clear deviation from an exponential dependence. We can then write the confinement induced change in cytosolic  $\text{Ca}^{2+}$  concentration as

$$\Delta n^{\text{Ca}^{2+}} = n_0^{\text{Ca}^{2+}} \left( e^{\frac{2R_n - w(x_n)}{h^*}} - 1 \right), \quad (4.39)$$

where  $h^* = \Delta A \tau_1 / k_B T$  is the characteristic confinement height of calcium release.

In principle, we would expect the cortical tension to show a non-linear dependence on the calcium concentration due to effects like contraction induced Rho release (Ju, Falconer, Dean, *et al.*, 2022) or saturation of the contractility. However, to keep the number of model parameters as low as possible, we only consider a linear dependence of the cortex tension on the calcium concentration. We can then express the pushing force explicitly in terms of the confinement width of the nucleus  $w(x_n)$  as

$$\begin{aligned} f_{\max}(w) &= S_0 \tau_{\text{cortex}}^0 \left( \frac{w(x_n)}{2R_n} \right)^{1-\nu_n} \left( e^{\frac{2R_n - w(x_n)}{h^*}} - 1 \right) \\ &\approx S_0 \tau_{\text{cortex}}^0 \left( \frac{w(x_n)}{2R_n} \right)^{1-\nu_n} \frac{2R_n - w(x_n)}{h^*} \end{aligned} \quad (4.40)$$

where  $\tau_{\text{cortex}}^0$  denotes the cortical tension in the absence of nuclear deformations.

Taken together, we adapt our model for two-dimensional confined cell migration to the case of 3D confinement, by introducing an additional nuclear drag and elastic nuclear deformations in the channel due to interactions between the nucleus and the sidewalls. Beyond that, we account for the observed force adaptation in confinement by introducing an additional pushing force that increases with increasing nuclear deformations.

### Constraining the model

To constrain our model, we use the rich migration dynamics that we observe experimentally at different channel widths. In particular the rate with which cells transition from one chamber to the other and the velocity with which they move through the channel display an interesting bi-phasic dependence on the channel width, reminiscent of the channel width dependence of the shape parameter  $\varepsilon$  (Figs. 4.14 and 4.11): For channel widths wider than the nuclear diameter ( $>12 \mu\text{m}$ ), cells can enter the channel without requiring nuclear deformations. From our work on 2D confined cell migration (Chapter 3), we know however that unconfined cells are also less polarized than confined cells. Consistent with this, we observe lower migration velocities and less frequent transitions compared to intermediate channel widths. Since in the absence of nuclear confinement, cells can only effectively pull their nucleus forward, we expect  $F_{\text{pull}} - F_{\text{push}} > 0$  in that case, which we indeed observe. Consistent with the increase in nuclear velocity at intermediate channel widths, also  $F_{\text{deform}}$  peaks at channel widths comparable to the nuclear diameter. Once the channel gets narrow enough to induce significant nuclear deformations ( $<12 \mu\text{m}$ ), transitions from one chamber to the other become rarer. At the same time, we

observe a decrease in  $F_{\text{deform}}$ , indicating an increase in pushing forces. Interestingly, also the nuclear velocities in the channel decrease at narrow channel widths.

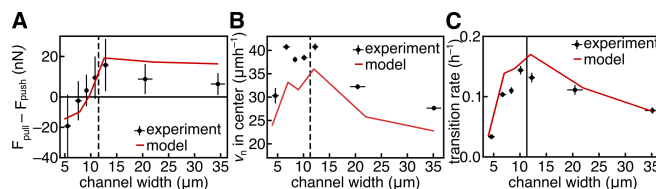


Figure 4.14: **Fitting the mechanistic model to key experimental statistics** (adapted from Stöberl *et al.*, 2023). **A.** Difference between pulling and pushing forces acting on the nucleus. **B.** Average velocity in the center of the pattern ( $|x_n| \leq 6 \mu\text{m}$ ). The maximal velocities are observed at an intermediate channel width comparable to the nuclear width. **C.** Transition rates for varying channel widths. Similar to the nuclear velocities, the highest transition rates are observed at intermediate channel widths. Error bars: Error bars of the channel width represent the standard deviation. Error bars associated with the y-axis represent one standard deviation (A) or the standard error (B), (C).

We fit our mechanistic model simultaneously to these three statistics by simulating the migration dynamics defined by Eqs. (4.24) - (4.26) and using our mechanical model for nuclear deformations (see Section 4.3) to relate the pulling forces, exerted by the protrusion onto the nucleus, and the pushing forces in our model to nuclear deformations. We find that our model can indeed reproduce the experimentally observed channel width dependence of the nuclear dynamics and deformations (see model fits in Fig. 4.14), which can thus be understood as an interplay between confinement induced polarization, increased nuclear drag due to interactions with the channel walls, and elastic nuclear deformations that trigger increased cortical tension and thus pushing forces: At widths wider than the size of the nucleus, stronger confinement leads to enhanced polarization and thus protrusion growth. This results in a larger force pulling on the nucleus from the front resulting in increased nuclear velocities and transition rates. By contrast, for channel widths below the nuclear width, increased pushing forces from the rear of the cell result in a decreasing  $F_{\text{pull}} - F_{\text{push}}$ , eventually even reaching negative values. Despite the increased polarization and the additional pushing force, the increased nuclear drag results in a decrease of the predicted nuclear velocity in the channel. Additionally, the increasing elastic energy barrier, associated to nucleus deformations, hinders the movement of the nucleus into the channel, resulting in a drop of the transition rates.

### Model predictions

After constraining the model with a number of key experimental statistics, we evaluate its predictive power. For that we consider aspects of the observed cellular migration behavior that were not previously used to constrain the model: the probability distributions of the nuclear position and velocities at different

channel widths as well as the full non-linear migration dynamics inferred in Section 4.2.

Experimentally, we observe that the probability distribution of the nuclear position transitions from a broad distribution at wide channel widths, to a strongly double-peaked distribution for narrow channels (Fig. 4.15A). The distributions of the nuclear velocities peak at zero independent of channel width, by decrease in spread with decreasing channel width (Fig. 4.15C). From simulating our model, we find that both the distribution of the nuclear position and velocity show semi-quantitative agreement with the experimental data. In particular, the model captures the overall dependence of the distributions on the channel width, with the appearance of clear peaks of the  $x_n$ -distribution in the chambers and pronounced minima in the channel at narrow channel widths and an overall narrowing of the nuclear velocities with increasing confinement (Fig. 4.15B and D). We find that the location of the peaks in the  $x_n$ -distribution deviates between experiment and simulations. For the simulation we find a maximum near the entrance of the channel, while in the experiments the maximum is located more towards the centre of the chamber. From assessment of the bright-field videos, we found that after a failed transition attempt during which the nucleus is placed near the entrance of the channel, the cells often retract their nucleus back to the centre of the channel for an extended period of time before it starts a new attempt. Since our model is designed to capture the interactions between the confinement and the cell and not necessarily the cellular behavior in the chamber, we did not include a mechanism that could account for this in our model in order to keep our mechanistic model as simple as possible while still capturing the essence of the cell confinement interactions. Beyond the differences between the model and the experiments in the chambers, we also find that the experimental velocity distribution fall of slower. This does however mostly affect the region of extremely high velocities ( $>50 \mu\text{m h}^{-1}$ ), which occur extremely rare, such that they have little effect on the population averaged migration dynamics.

To go beyond the comparison of a number of hand-picked statistics, we compute the effective underdamped dynamics of our model to allow for a comparison with the inferred models in Section 4.2. Apart from testing our model, this also allows us to connect features in the NCMs to biological mechanisms. For that, we follow the approach mentioned in Section 3.6 to compute the effective underdamped dynamics of the nucleus from an overdamped model.

We start by rewriting the equations for the nuclear and the protrusion coordinate as

$$\gamma(x_n)\dot{x}_n = k_n(x_p - x_n) + f_{\text{push}}(x_n) + f_{\text{channel}}(x_n) \equiv f_n(x_n, x_p) \quad (4.41)$$

and

$$\dot{x}_p = -k_p(x_p - x_n) - \partial_{x_p}V(x_p) + rP(t) \equiv f_p(x_n, x_p) + rP(t). \quad (4.42)$$

This allows us to calculate  $F_w(x_n, v_n)$  of the underdamped Langevin equation

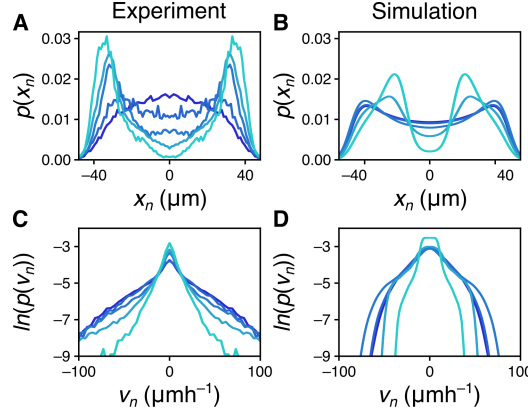


Figure 4.15: **Comparison between experimental and simulated probability distributions** (adapted from Stöberl *et al.*, 2023). **A.** and **B.** Experimentally observed and simulated distributions of the nuclear position  $x_n$  at different channel widths. **C.** and **D.** Experimentally observed and simulated distributions of the nuclear velocity  $v_n$  at different channel widths. Color scheme: from light to dark: 4  $\mu\text{m}$ , 7  $\mu\text{m}$ , 12  $\mu\text{m}$ , 20  $\mu\text{m}$  and 35  $\mu\text{m}$

(Eq. (4.1)) as

$$\begin{aligned}
 F_w(x_n, v_n) &= \langle \dot{v}_n | x_n, v_n \rangle = \left\langle \frac{df_n(x_n, x_p)}{dt} \Big| x_n, v_n \right\rangle \\
 &= \left\langle \frac{df_n}{dx_n} v_n + \frac{df_n}{dx_p} \dot{x}_p \Big| x_n, v_n \right\rangle \\
 &\stackrel{\text{Eq. (4.42)}}{=} v_n \frac{df_n}{dx_n} + \frac{df_n}{dx_p} \langle f_p(x_n, x_p) + rP(t) | x_n, v_n \rangle \quad (4.43) \\
 &\stackrel{\text{Eq. (4.41)}}{=} v_n \frac{df_n}{dx_n} + \frac{df_n}{dx_p} \langle rP(t) | x_n, v_n \rangle \\
 &\quad + \frac{df_n}{dx_p} f_p(x_n, x_p) \Big|_{x_p=x_n} + \frac{\gamma(x_n)v_n - f_{\text{push}}(x_n) - f_{\text{channel}}(x_n)}{k_n}
 \end{aligned}$$

While most terms in Eq. (4.43) can be calculated analytically,  $\langle rP(t) | x_n, v_n \rangle$  needs to be determined numerically. The resulting  $F_w(x_n, v_n)$  and corresponding confinement signature maps are shown in Fig. 4.16.

Similar to the dynamics inferred from experiments, we observe a deterministic flow from one chamber to the other with a pronounced acceleration in the channel (Fig. 4.16A). Inline with the previously discussed difference between the observed and predicted nuclear positions, we find bigger differences between the inferred dynamics (Fig. 4.7) and the effective underdamped dynamics of the model are found on the islands, where the inferred models show strong decelerations of the nucleus, which are not captured by our model. Despite this, we find that our model successfully predicts most of the key features observed in the NCMs (Fig. 4.16B): At the channel entrance the elastic barrier associated with nuclear deformations results in a region of  $\langle \Delta F_w \rangle < 0$ , followed by a pronounced region of  $\langle \Delta F_w \rangle > 0$  associated with the recoil of the contractile actomyosin structures in the protrusion and the additional pushing forces

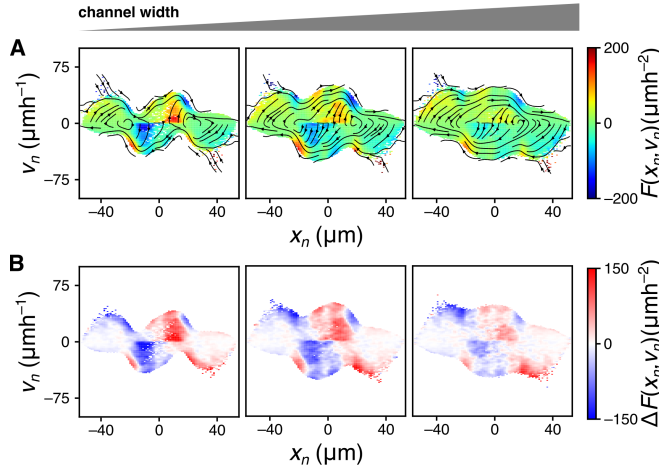


Figure 4.16: **Effective underdamped dynamics of the model** (adapted from Stöberl *et al.*, 2023). **A.** The deterministic contribution to the underdamped Langevin equation calculated through Eq. (4.43). **B.** The corresponding nuclear confinement maps calculated as  $F_{12\ \mu\text{m}} - F_w$ . (from left to right: 4  $\mu\text{m}$ , 7  $\mu\text{m}$ , 9  $\mu\text{m}$ ).

acting onto the nucleus. Finally, as the cell leaves the channel, we observe a region of deceleration ( $\langle \Delta F_w \rangle < 0$ ) as the nucleus catches up with the protrusion. In conclusion, our mechanistic model demonstrates that cells transition from pulling to pushing dominated migration to generate sufficient deformation forces in confinement. This model not only explains the observed nuclear deformations but also allows for a mechanistic interpretation of the effective cellular dynamics inferred from experimental data.

## 4.5 Discussion and Outlook

We generalized our approach of combining bottom-up mechanistic modeling approaches with top-down inference approaches for cell migration to migration in 3D confining environments. For that we studied the repeated self-imposed migration of single cells through compliant 3D channels, which requires strong, reversible nuclear deformations at narrow channel widths. These deformations have a multifaceted impact on the cell dynamics in the channel, which become apparent when comparing the inferred non-linear migration dynamics at different channel widths. In the presence of nuclear deformations, cells display a marked slowing down during the entry phase of the nucleus into the channel, followed by an acceleration out of the channel. To construct a mechanistic model that can explain the observed effect of the 3D confinement on the non-linear migration dynamics, we analyzed nuclear deformations during transitions from one chamber. These indicated a confinement-sensitive, adaptive cellular force generation, with additional pushing forces that might help migration through narrow confinements. Based on this, we generalized our mechanistic model for mesenchymal cell migration that we derived in Chapter 3 by accounting for the adaptive modulation of forces in response to confinement. The increase in

pushing forces within confinement, together with elastic deformations of the nucleus and increased effective friction in the channel, explains both the observed nuclear deformations, as well as the overall migration dynamics of the cells across a broad range of channel widths.

Both pulling and pushing forces have been qualitatively identified to play a role in confined cell migration (Davidson, Battistella, *et al.*, 2020; Keys *et al.*, 2022; McGregor *et al.*, 2016; Thomas *et al.*, 2015). Our analysis of nuclear deformations in confinement provides a quantitative measure of the balance between pulling and pushing forces, which indicates a confinement-induced adaptation of cellular force generation. This contributes to a more comprehensive mechanistic understanding of the complex interplay between confinement, the nucleus, and the cytoskeleton during mesenchymal cell migration and highlights the crucial importance of the interaction between nucleus and cytoskeleton during three-dimensionally confined cell migration. A potential mechanism that could be involved in this force adaptation is the upregulation of cortical contractility in response to externally induced nuclear confinement (Lomakin *et al.*, 2020; Venturini *et al.*, 2020). Further research is however required to experimentally verify the mechanism of increased cortical contractility through intracellular calcium imaging and identify whether this mechanism is universally applicable or specific to certain highly migratory cell lines, such as cancer cells.

Overall, we saw in this chapter how the combination of data-driven model inference and measurements of the mechanical properties of the cell and its organelles can be used to construct a mechanistic model for confined cell migration. Our dynamical model successfully predicts key features of the nuclear confinement maps, which allows for a mechanistic interpretation of the inferred dynamics in terms of confinement-induced elastic nuclear deformations and cellular force adaptation. However, our approach relied on a previously derived model for 2D confined cell migration and that this model could successfully be generalized to the case of 3D migration as well as additional measurements of the nuclear mechanics and deformations. Here, it would be interesting to develop a systematic approach that allows to directly include other aspects than the nuclear trajectories in the model inference that might allow for a more direct inference of the underlying mechanistic model. For that, an approach that infers overdamped Langevin equations might be promising (S. Amiri *et al.*, n.d.).

Another challenge that we faced when inferring the effective, underdamped migration dynamics was the issue model selection and uniqueness. For that, we quantified the predictive power of the model by comparing experimental data and model predictions for a number of key experimental statistics. The selection of these statistics is however subjective and specific to the experimental system. Here, parametrized inference approaches such as used here would greatly benefit from a more systematic and general method of model selection.

## Conclusion and outlook

One of the most memorable moment of my physics education was when I saw for the first time how the ideal gas law could be derived from the equation of motion of individual particles. Being able to bridge some many length scales and connecting microscopic properties to macroscopic was deeply impressive. All of a sudden, seemingly simple, phenomenological equations such as the ideal gas law or the van der Waals equation were so much richer, clearer, and deeper than before. Since then, the idea that to understand a system you need to connect its behavior to the properties and interactions of its underlying components never really left me. Following this philosophy, I believe that besides the results obtained in the individual projects that contributed to this thesis, the key insight of this work is that a like-minded approach can also be successful in the context of cell migration.

Obviously we are dealing with an active system here, such that the tools and techniques used in equilibrium statistical physics are not applicable. Nonetheless, the spirit of connecting underlying microscopic details to macroscopic behavior remains: For contractile actomyosin gels, we saw in Chapter 2 how the load-sensitive binding and unbinding dynamics of individual myosin heads shape the mechanosensitive large-scale contraction dynamics. For mesenchymal migration in 2D, we found in Chapter 3 that a simple, springlike protrusion force emerges from the interplay between actin polymerization, membrane tension and focal adhesions. Also accounting for a coupling between polarity cues and retrograde flow, allowed us to explain the interesting geometry-sensitive polarization dynamics that were observed previously. Here, previously constrained data-driven models for the overall migration behavior were essential to guide the systematic coarse graining of our microscopic model. However, in contrast to these data-driven models, our microscopic understanding of the emergent migration behavior allowed us to easily generalize this model to a number of different experimental systems. Finally, we demonstrated in Chapter 4 that this approach can also be taken beyond migration on 2D surfaces and can yield valuable insights into the differences between migration on 2D and 3D substrates that can be understood as the consequence of transient deformations of the nucleus.

To push this approach even further and apply it to other systems, constraining reliable and rigorously inferred data-driven models will be essential.

Without such models, coarse graining and constraining microscopic models is likely to be a hopeless endeavor. In my work, I was lucky that such models were already established at least for the case of 2D migration and that the application to our 3D migration assay was possible without big changes to the method. Nonetheless, these techniques have to be further developed and extended to allow for their application to other systems, such as multicellular migration or migration in irregular three-dimensional matrices. If that is done successfully I do believe that microscopic models have a tremendous potential in improving our quantitative understanding of cell migration in physiologically relevant scenarios. The quantitative predictive power of our model for 2D migration that we show in Chapter 3 underlines this. Apart from the usefulness of quantitatively predictive migration models for potential long-term applications such as better predictions for cancer metastasis, this approach also gives us a lens through which we can take a closer look into the fascinating and beautiful complex system that underlies cell migration. I am thus convinced that both bottom-up and top-down approaches to modeling biological systems can only realize their full potential when being used in a combined approach.

---

## Bibliography

- Abercrombie, M. (Dec. 1977). “Concepts in Morphogenesis”. In: *Proceedings of the Royal Society of London. Series B. Biological Sciences* 199.1136, pp. 337–344 (cit. on p. 36).
- (Feb. 1980). “The Croonian Lecture, 1978 - The Crawling Movement of Metazoan Cells”. In: *Proceedings of the Royal Society of London. Series B. Biological Sciences* 207.1167, pp. 129–147 (cit. on pp. 31, 36).
- Abercrombie, M., J. E. Heaysman, and S. M. Pegrum (Mar. 1970). “The Locomotion of Fibroblasts in Culture I. Movements of the Leading Edge”. In: *Experimental Cell Research* 59.3, pp. 393–398 (cit. on p. 36).
- Aguilar-Cuenca, R., A. Juanes-García, and M. Vicente-Manzanares (Feb. 2014). “Myosin II in Mechanotransduction: Master and Commander of Cell Migration, Morphogenesis, and Cancer”. In: *Cellular and Molecular Life Sciences* 71.3, pp. 479–492 (cit. on p. 10).
- Alvarado, J. and G. H. Koenderink (2015). “Reconstituting Cytoskeletal Contraction Events with Biomimetic Actin–Myosin Active Gels”. In: *Methods in Cell Biology*. Vol. 128. Elsevier, pp. 83–103 (cit. on p. 6).
- Amiri, B. *et al.* (Mar. 2023). “On Multistability and Constitutive Relations of Cell Motion on Fibronectin Lanes”. In: *Biophysical Journal* 122.5, pp. 753–766 (cit. on pp. 49, 72).
- Amiri, S. *et al.* (n.d.). *Manuscript in Preparation* (cit. on pp. 72, 106).
- Assémat, E. *et al.* (Mar. 2008). “Polarity Complex Proteins”. In: *Biochimica et Biophysica Acta (BBA) - Biomembranes* 1778.3, pp. 614–630 (cit. on p. 37).
- Balakrishnan, V. (Apr. 1993). “On a Simple Derivation of Master Equations for Diffusion Processes Driven by White Noise and Dichotomic Markov Noise”. In: *Pramana* 40.4, pp. 259–265 (cit. on p. 32).
- Banerjee, S., M. L. Gardel, and U. S. Schwarz (Mar. 2020). “The Actin Cytoskeleton as an Active Adaptive Material”. In: *Annual Review of Condensed Matter Physics* 11.1, pp. 421–439 (cit. on p. 1).
- Bausch, A. R. and K. Kroy (Apr. 2006). “A Bottom-up Approach to Cell Mechanics”. In: *Nature Physics* 2.4, pp. 231–238 (cit. on p. 5).
- Bell, E. S. *et al.* (2022). “Low Lamin A Levels Enhance Confined Cell Migration and Metastatic Capacity in Breast Cancer”. In: *Oncogene* 41.36, pp. 4211–4230 (cit. on p. 91).

- Bendix, P. M. *et al.* (Apr. 2008). “A Quantitative Analysis of Contractility in Active Cytoskeletal Protein Networks”. In: *Biophysical Journal* 94.8, pp. 3126–3136 (cit. on p. 26).
- Bieling, P. *et al.* (Jan. 2016). “Force Feedback Controls Motor Activity and Mechanical Properties of Self-Assembling Branched Actin Networks”. In: *Cell* 164.1-2, pp. 115–127 (cit. on p. 43).
- Blanchoin, L. *et al.* (Jan. 2014). “Actin Dynamics, Architecture, and Mechanics in Cell Motility”. In: *Physiological Reviews* 94.1, pp. 235–263 (cit. on pp. 18, 42, 43).
- Bovellan, M. *et al.* (July 2014). “Cellular Control of Cortical Actin Nucleation”. In: *Current Biology* 24.14, pp. 1628–1635 (cit. on p. 43).
- Broedersz, C. P. and F. C. MacKintosh (July 2014). “Modeling Semiflexible Polymer Networks”. In: *Reviews of Modern Physics* 86.3, pp. 995–1036 (cit. on pp. 7–9, 15, 41).
- Broedersz, C. P., X. Mao, *et al.* (Dec. 2011). “Criticality and Isostaticity in Fibre Networks”. In: *Nature Physics* 7.12, pp. 983–988 (cit. on p. 9).
- Broussard, J. A., D. J. Webb, and I. Kaverina (Feb. 2008). “Asymmetric Focal Adhesion Disassembly in Motile Cells”. In: *Current Opinion in Cell Biology* 20.1, pp. 85–90 (cit. on p. 44).
- Brückner, D. B., N. Arlt, *et al.* (Feb. 2021). “Learning the Dynamics of Cell–Cell Interactions in Confined Cell Migration”. In: *Proceedings of the National Academy of Sciences* 118.7, e2016602118 (cit. on pp. 72–75).
- Brückner, D. B. and C. P. Broedersz (2023). “Learning Dynamical Models of Single and Collective Cell Migration: A Review”. In: (cit. on pp. 2, 3, 31, 32, 45, 46).
- Brückner, D. B., A. Fink, C. Schreiber, *et al.* (June 2019). “Stochastic Nonlinear Dynamics of Confined Cell Migration in Two-State Systems”. In: *Nature Physics* 15.6, pp. 595–601 (cit. on pp. 2, 3, 32, 34, 35, 46, 49, 52, 57, 82, 83, 87).
- Brückner, D. B., M. Schmitt, *et al.* (Sept. 2022). “Geometry Adaptation of Protrusion and Polarity Dynamics in Confined Cell Migration”. In: *Physical Review X* 12.3, p. 031041 (cit. on pp. 32, 35, 36, 41, 42, 46, 48–50, 52–57, 72, 87, 96, 97).
- Brückner, D. B., A. Fink, J. O. Rädler, *et al.* (2020). “Disentangling the Behavioural Variability of Confined Cell Migration”. In: *Journal of The Royal Society Interface* 17.163, p. 20190689 (cit. on p. 46).
- Brückner, D. B., P. Ronceray, and C. P. Broedersz (2020). “Inferring the Dynamics of Underdamped Stochastic Systems”. In: *Physical review letters* 125.5, p. 058103 (cit. on pp. 3, 34, 82).
- Burridge, K. (Oct. 2017). “Focal Adhesions: A Personal Perspective on a Half Century of Progress”. In: *The FEBS Journal* 284.20, pp. 3355–3361 (cit. on p. 43).
- Burridge, K. and C. Guillyuy (Apr. 2016). “Focal Adhesions, Stress Fibers and Mechanical Tension”. In: *Experimental Cell Research* 343.1, pp. 14–20 (cit. on pp. 38, 39, 44, 45).
- Caballero, D., J. Comelles, *et al.* (Dec. 2015). “Ratchetaxis: Long-Range Directed Cell Migration by Local Cues”. In: *Trends in Cell Biology* 25.12, pp. 815–827 (cit. on pp. 2, 32, 34, 45, 62).

- Caballero, D., R. Voituriez, and D. Riveline (July 2014). “Protrusion Fluctuations Direct Cell Motion”. In: *Biophysical Journal* 107.1, pp. 34–42 (cit. on pp. 34, 42, 63–65).
- Cao, X. *et al.* (2016). “A Chemomechanical Model for Nuclear Morphology and Stresses during Cell Transendothelial Migration”. In: *Biophysical journal* 111.7, pp. 1541–1552 (cit. on pp. 81, 89, 91, 100).
- Carlip, S. (Oct. 2014). “Black Hole Thermodynamics”. In: *International Journal of Modern Physics D* 23.11, p. 1430023 (cit. on p. 3).
- Caruel, M. and L. Truskinovsky (Mar. 2018). “Physics of Muscle Contraction”. In: *Reports on Progress in Physics* 81.3, p. 036602 (cit. on p. 19).
- Chaffer, C. L. and R. A. Weinberg (Mar. 2011). “A Perspective on Cancer Cell Metastasis”. In: *Science* 331.6024, pp. 1559–1564 (cit. on p. 2).
- Chan, C. E. and D. J. Odde (Dec. 2008). “Traction Dynamics of Filopodia on Compliant Substrates”. In: *Science* 322.5908, pp. 1687–1691 (cit. on p. 45).
- Chang, I.-D. (1961). “On the Wall Effect Correction of the Stokes Drag Formula for Axially Symmetric Bodies Moving inside a Cylindrical Tube”. In: *Zeitschrift für angewandte Mathematik und Physik ZAMP* 12, pp. 6–14 (cit. on p. 99).
- Charras, G. and E. Sahai (Dec. 2014). “Physical Influences of the Extracellular Environment on Cell Migration”. In: *Nature Reviews Molecular Cell Biology* 15.12, pp. 813–824 (cit. on p. 32).
- Charras, G. and A. S. Yap (Apr. 2018). “Tensile Forces and Mechanotransduction at Cell–Cell Junctions”. In: *Current Biology* 28.8, R445–R457 (cit. on p. 1).
- Chen, Y., D. Saintillan, and P. Rangamani (Dec. 2023). “Interplay Between Mechanosensitive Adhesions and Membrane Tension Regulates Cell Motility”. In: *PRX Life* 1.2, p. 023007 (cit. on p. 73).
- Cheng, Y.-S., F. De Souza Leite, and D. E. Rassier (Jan. 2020). “The Load Dependence and the Force-Velocity Relation in Intact Myosin Filaments from Skeletal and Smooth Muscles”. In: *American Journal of Physiology-Cell Physiology* 318.1, pp. C103–C110 (cit. on p. 21).
- Cheng, S., M. S. Geddis, and V. Rehder (Mar. 2002). “Local Calcium Changes Regulate the Length of Growth Cone Filopodia”. In: *Journal of Neurobiology* 50.4, pp. 263–275 (cit. on p. 42).
- Choi, C. K. *et al.* (Sept. 2008). “Actin and  $\alpha$ -Actinin Orchestrate the Assembly and Maturation of Nascent Adhesions in a Myosin II Motor-Independent Manner”. In: *Nature Cell Biology* 10.9, pp. 1039–1050 (cit. on p. 45).
- Chugh, P., A. G. Clark, *et al.* (June 2017). “Actin Cortex Architecture Regulates Cell Surface Tension”. In: *Nature Cell Biology* 19.6, pp. 689–697 (cit. on p. 26).
- Chugh, P. and E. K. Paluch (July 2018). “The Actin Cortex at a Glance”. In: *Journal of Cell Science* 131.14, jcs186254 (cit. on pp. 6, 9).
- Ciobanasiu, C., B. Faivre, and C. Le Clainche (Jan. 2014). “Actomyosin-Dependent Formation of the Mechanosensitive Talin–Vinculin Complex Reinforces Actin Anchoring”. In: *Nature Communications* 5.1, p. 3095 (cit. on p. 44).
- Clark, A. G. and D. M. Vignjevic (Oct. 2015). “Modes of Cancer Cell Invasion and the Role of the Microenvironment”. In: *Current Opinion in Cell Biology* 36, pp. 13–22 (cit. on pp. 2, 31).

- Craig, R. and R. Padrón (2004). “Molecular Structure of the Sarcomere”. In: *Myology: Basic and Clinical*. 3rd ed. McGraw-Hill, pp. 129–166 (cit. on p. 12).
- Critchley, D. R. (June 2009). “Biochemical and Structural Properties of the Integrin-Associated Cytoskeletal Protein Talin”. In: *Annual Review of Biophysics* 38.1, pp. 235–254 (cit. on p. 44).
- Cunningham, C. C. *et al.* (Jan. 1992). “Actin-Binding Protein Requirement for Cortical Stability and Efficient Locomotion”. In: *Science* 255.5042, pp. 325–327 (cit. on p. 43).
- Dahl, K. N., A. J. Ribeiro, and J. Lammerding (June 2008). “Nuclear Shape, Mechanics, and Mechanotransduction”. In: *Circulation Research* 102.11, pp. 1307–1318 (cit. on p. 79).
- Damiano-Guercio, J. *et al.* (May 2020). “Loss of Ena/VASP Interferes with Lamellipodium Architecture, Motility and Integrin-Dependent Adhesion”. In: *eLife* 9, e55351 (cit. on p. 49).
- Danuser, G., J. Allard, and A. Mogilner (Oct. 2013). “Mathematical Modeling of Eukaryotic Cell Migration: Insights Beyond Experiments”. In: *Annual Review of Cell and Developmental Biology* 29.1, pp. 501–528 (cit. on pp. 1, 2, 6, 31, 36–38, 45, 46).
- Davidson, P. M., C. Denais, *et al.* (Sept. 2014). “Nuclear Deformability Constitutes a Rate-Limiting Step During Cell Migration in 3-D Environments”. In: *Cellular and Molecular Bioengineering* 7.3, pp. 293–306 (cit. on p. 79).
- Davidson, P. M., J. Sliz, *et al.* (2015). “Design of a Microfluidic Device to Quantify Dynamic Intra-Nuclear Deformation during Cell Migration through Confining Environments”. In: *Integrative Biology* 7.12, pp. 1534–1546 (cit. on pp. 81, 89).
- Davidson, P. M., A. Battistella, *et al.* (July 2020). “Nesprin-2 Accumulates at the Front of the Nucleus during Confined Cell Migration”. In: *EMBO reports* 21.7 (cit. on pp. 78, 89, 106).
- De Bruyn, P. P. H. (Mar. 1947). “Theories of Amoeboid Movement”. In: *The Quarterly Review of Biology* 22.1, pp. 1–24 (cit. on p. 36).
- Debold, E. P., J. B. Patlak, and D. M. Warshaw (Nov. 2005). “Slip Sliding Away: Load-Dependence of Velocity Generated by Skeletal Muscle Myosin Molecules in the Laser Trap”. In: *Biophysical Journal* 89.5, pp. L34–L36 (cit. on p. 11).
- Dentröder, W. (2017). “Real Solid and Liquid Bodies”. In: *Mechanics and Thermodynamics*. 1st ed. Springer International Publishing, p. 157 (cit. on p. 92).
- Denais, C. M. *et al.* (Apr. 2016). “Nuclear Envelope Rupture and Repair during Cancer Cell Migration”. In: *Science* 352.6283, pp. 353–358 (cit. on p. 80).
- Digman, M. A. *et al.* (Apr. 2008). “Paxillin Dynamics Measured during Adhesion Assembly and Disassembly by Correlation Spectroscopy”. In: *Biophysical Journal* 94.7, pp. 2819–2831 (cit. on p. 45).
- Dobrzynska, A. *et al.* (May 2016). “The Nuclear Lamina in Health and Disease”. In: *Nucleus* 7.3, pp. 233–248 (cit. on p. 79).
- Dominguez, R. and K. C. Holmes (June 2011). “Actin Structure and Function”. In: *Annual Review of Biophysics* 40.1, pp. 169–186 (cit. on p. 6).
- Du Roure, O. *et al.* (Feb. 2005). “Force Mapping in Epithelial Cell Migration”. In: *Proceedings of the National Academy of Sciences* 102.7, pp. 2390–2395 (cit. on p. 40).

- DuChez, B. J. *et al.* (Feb. 2019). “Durotaxis by Human Cancer Cells”. In: *Biophysical Journal* 116.4, pp. 670–683 (cit. on p. 2).
- Edelstein-Keshet, L. *et al.* (Nov. 2013). “From Simple to Detailed Models for Cell Polarization”. In: *Philosophical Transactions of the Royal Society B: Biological Sciences* 368.1629, p. 20130003 (cit. on pp. 31, 38, 45).
- Elosegui-Artola, A., R. Oria, *et al.* (May 2016). “Mechanical Regulation of a Molecular Clutch Defines Force Transmission and Transduction in Response to Matrix Rigidity”. In: *Nature Cell Biology* 18.5, pp. 540–548 (cit. on p. 45).
- Elosegui-Artola, A., X. Trepast, and P. Roca-Cusachs (May 2018). “Control of Mechanotransduction by Molecular Clutch Dynamics”. In: *Trends in Cell Biology* 28.5, pp. 356–367 (cit. on p. 6).
- Engler, A. J., C. Carag-Krieger, *et al.* (Nov. 2008). “Embryonic Cardiomyocytes Beat Best on a Matrix with Heart-like Elasticity: Scar-like Rigidity Inhibits Beating”. In: *Journal of Cell Science* 121.22, pp. 3794–3802 (cit. on p. 5).
- Engler, A. J., S. Sen, *et al.* (Aug. 2006). “Matrix Elasticity Directs Stem Cell Lineage Specification”. In: *Cell* 126.4, pp. 677–689 (cit. on pp. 1, 5).
- Ennomani, H. *et al.* (Mar. 2016). “Architecture and Connectivity Govern Actin Network Contractility”. In: *Current Biology* 26.5, pp. 616–626 (cit. on p. 16).
- Erdmann, T., P. J. Albert, and U. S. Schwarz (Nov. 2013). “Stochastic Dynamics of Small Ensembles of Non-Processive Molecular Motors: The Parallel Cluster Model”. In: *The Journal of Chemical Physics* 139.17, p. 175104 (cit. on pp. 11, 12).
- Erdmann, T. and U. S. Schwarz (Apr. 2012). “Stochastic Force Generation by Small Ensembles of Myosin II Motors”. In: *Physical Review Letters* 108.18, p. 188101 (cit. on p. 11).
- Estabrook, I. D. *et al.* (May 2021). “Calculation of the Force Field Required for Nucleus Deformation during Cell Migration through Constrictions”. In: *PLOS Computational Biology* 17.5. Ed. by S. L. Diamond, e1008592 (cit. on pp. 90, 92).
- Faix, J. and K. Rottner (Feb. 2006). “The Making of Filopodia”. In: *Current Opinion in Cell Biology* 18.1, pp. 18–25 (cit. on p. 42).
- Falanga, V. (Nov. 2005). “Wound Healing and Its Impairment in the Diabetic Foot”. In: *The Lancet* 366.9498, pp. 1736–1743 (cit. on p. 1).
- Faure-André, G. *et al.* (Dec. 2008). “Regulation of Dendritic Cell Migration by CD74, the MHC Class II-Associated Invariant Chain”. In: *Science* 322.5908, pp. 1705–1710 (cit. on p. 77).
- Fenteany, G., P. A. Janmey, and T. P. Stossel (July 2000). “Signaling Pathways and Cell Mechanics Involved in Wound Closure by Epithelial Cell Sheets”. In: *Current Biology* 10.14, pp. 831–838 (cit. on p. 31).
- Fletcher, D. A. and R. D. Mullins (Jan. 2010). “Cell Mechanics and the Cytoskeleton”. In: *Nature* 463.7280, pp. 485–492 (cit. on pp. 1, 5).
- Flommersfeld, J. *et al.* (2023). “Geometry-Sensitive Protrusion Growth Directs Confined Cell Migration”. In: *arXiv preprint arXiv:2308.08372* (cit. on pp. 47, 49, 50, 53, 57–61, 63, 64, 66, 73).
- Floyd, C., G. A. Papoian, and C. Jarzynski (June 2019). “Quantifying Dissipation in Actomyosin Networks”. In: *Interface Focus* 9.3, p. 20180078 (cit. on p. 30).
- Foster, P. J., J. Bae, *et al.* (Apr. 2023). “Dissipation and Energy Propagation across Scales in an Active Cytoskeletal Material”. In: *Proceedings of the National Academy of Sciences* 120.14, e2207662120 (cit. on pp. 29, 30).

- Foster, P. J., S. Fürthauer, *et al.* (Dec. 2015). “Active Contraction of Microtubule Networks”. In: *eLife* 4, e10837 (cit. on pp. 16, 26).
- Franz, C. M., G. E. Jones, and A. J. Ridley (Feb. 2002). “Cell Migration in Development and Disease”. In: *Developmental Cell* 2.2, pp. 153–158 (cit. on pp. 1, 31).
- Friedl, P. and B. Weigelin (Sept. 2008). “Interstitial Leukocyte Migration and Immune Function”. In: *Nature Immunology* 9.9, pp. 960–969 (cit. on p. 31).
- Friedl, P., K. Wolf, and J. Lammerding (Feb. 2011). “Nuclear Mechanics during Cell Migration”. In: *Current Opinion in Cell Biology* 23.1, pp. 55–64 (cit. on pp. 2, 79).
- Fu, Y. *et al.* (2012). “Nuclear Deformation during Breast Cancer Cell Transmigration”. In: *Lab on a Chip* 12.19, p. 3774 (cit. on pp. 79, 80).
- Fürth, R. (Jan. 1917). “Einige Untersuchungen Über Brownsche Bewegung an Einem Einzelteilchen”. In: *Annalen der Physik* 358.11, pp. 177–213 (cit. on p. 32).
- (June 1920). “Die Brownsche Bewegung bei Berücksichtigung einer Persistenz der Bewegungsrichtung. Mit Anwendungen auf die Bewegung lebender Infusorien”. In: *Zeitschrift für Physik* 2.3, pp. 244–256 (cit. on pp. 32, 33).
- Fürthauer, S. *et al.* (Dec. 2019). “Self-Straining of Actively Crosslinked Microtubule Networks”. In: *Nature Physics* 15.12, pp. 1295–1300 (cit. on p. 53).
- Gauthier, N. C. *et al.* (Aug. 2011). “Temporary Increase in Plasma Membrane Tension Coordinates the Activation of Exocytosis and Contraction during Cell Spreading”. In: *Proceedings of the National Academy of Sciences* 108.35, pp. 14467–14472 (cit. on p. 48).
- Ghibaudo, M. *et al.* (2008). “Traction Forces and Rigidity Sensing Regulate Cell Functions”. In: *Soft Matter* 4.9, p. 1836 (cit. on p. 5).
- Gittes, F. and F. C. MacKintosh (Aug. 1998). “Dynamic Shear Modulus of a Semiflexible Polymer Network”. In: *Physical Review E* 58.2, R1241–R1244 (cit. on pp. 8, 9).
- Granek, R. (Dec. 1997). “From Semi-Flexible Polymers to Membranes: Anomalous Diffusion and Reptation”. In: *Journal de Physique II* 7.12, pp. 1761–1788 (cit. on p. 9).
- Guo, B. and W. H. Guilford (June 2006). “Mechanics of Actomyosin Bonds in Different Nucleotide States Are Tuned to Muscle Contraction”. In: *Proceedings of the National Academy of Sciences* 103.26, pp. 9844–9849 (cit. on p. 11).
- Gupton, S. L. and C. M. Waterman-Storer (June 2006). “Spatiotemporal Feedback between Actomyosin and Focal-Adhesion Systems Optimizes Rapid Cell Migration”. In: *Cell* 125.7, pp. 1361–1374 (cit. on p. 49).
- Han, S. *et al.* (Aug. 2012). “Decoupling Substrate Stiffness, Spread Area, and Micropost Density: A Close Spatial Relationship between Traction Forces and Focal Adhesions”. In: *Biophysical Journal* 103.4, pp. 640–648 (cit. on p. 5).
- Harada, T. *et al.* (Mar. 2014). “Nuclear Lamin Stiffness Is a Barrier to 3D Migration, but Softness Can Limit Survival”. In: *Journal of Cell Biology* 204.5, pp. 669–682 (cit. on pp. 79, 80, 91).
- Hartman, M. A. and J. A. Spudich (Apr. 2012). “The Myosin Superfamily at a Glance”. In: *Journal of Cell Science* 125.7, pp. 1627–1632 (cit. on p. 39).

- Hawkins, R. J. *et al.* (Feb. 2009). “Pushing off the Walls: A Mechanism of Cell Motility in Confinement”. In: *Physical Review Letters* 102.5, p. 058103 (cit. on p. 77).
- Hawkins, R. *et al.* (Sept. 2011). “Spontaneous Contractility-Mediated Cortical Flow Generates Cell Migration in Three-Dimensional Environments”. In: *Biophysical Journal* 101.5, pp. 1041–1045 (cit. on p. 39).
- Hellinger, E. (1909). “Neue Begründung Der Theorie Quadratischer Formen von Unendlichvielen Veränderlichen.” In: *Journal für die reine und angewandte Mathematik* 1909.136, pp. 210–271 (cit. on p. 85).
- Hencky, H. (1928). “Über Die Form Des Elastizitätsgesetzes Bei Ideal Elastischen Stoffen”. In: *Zeit. Tech. Phys.* 9, pp. 215–220 (cit. on p. 93).
- Hertz, H. (1882). “Ueber Die Berührung Fester Elastischer Körper.” In: *crll* 1882.92, pp. 156–171 (cit. on p. 90).
- Heussinger, C., M. Bathe, and E. Frey (July 2007). “Statistical Mechanics of Semiflexible Bundles of Wormlike Polymer Chains”. In: *Physical Review Letters* 99.4, p. 048101 (cit. on p. 42).
- Higgs, H. N. (Jan. 2011). “Discussing the Morphology of Actin Filaments in Lamellipodia”. In: *Trends in Cell Biology* 21.1, pp. 2–4 (cit. on p. 42).
- Hobson, C. M. and A. D. Stephens (July 2020). “Modeling of Cell Nuclear Mechanics: Classes, Components, and Applications”. In: *Cells* 9.7, p. 1623 (cit. on p. 80).
- Houk, A. *et al.* (Jan. 2012). “Membrane Tension Maintains Cell Polarity by Confining Signals to the Leading Edge during Neutrophil Migration”. In: *Cell* 148.1-2, pp. 175–188 (cit. on pp. 43, 48).
- House, D. *et al.* (June 2009). “Tracking of Cell Populations to Understand Their Spatio-Temporal Behavior in Response to Physical Stimuli”. In: *2009 IEEE Computer Society Conference on Computer Vision and Pattern Recognition Workshops*. Miami, FL: IEEE, pp. 186–193 (cit. on pp. 34, 66, 70).
- Howard, J. (2005a). “ATP Hydrolysis”. In: *Mechanics of Motor Proteins and the Cytoskeleton*. Sinauer, pp. 229–224 (cit. on p. 11).
- (2005b). “MotilityModels: From Crossbridges to Motion”. In: *Mechanics of Motor Proteins and the Cytoskeleton*. Sinauer, pp. 263–283 (cit. on p. 49).
- (2005c). “Speeds of Motors”. In: *Mechanics of Motor Proteins and the Cytoskeleton*. Sinauer, pp. 213–227 (cit. on pp. 11, 49).
- Hsia, C.-R. *et al.* (Sept. 2022). “Confined Migration Induces Heterochromatin Formation and Alters Chromatin Accessibility”. In: *iScience* 25.9, p. 104978 (cit. on p. 2).
- Iden, S. and J. G. Collard (Nov. 2008). “Crosstalk between Small GTPases and Polarity Proteins in Cell Polarization”. In: *Nature Reviews Molecular Cell Biology* 9.11, pp. 846–859 (cit. on pp. 5, 37, 38, 40).
- Ideses, Y. *et al.* (June 2018). “Spontaneous Buckling of Contractile Poroelectric Actomyosin Sheets”. In: *Nature Communications* 9.1, p. 2461 (cit. on p. 16).
- Irianto, J. *et al.* (Jan. 2017). “DNA Damage Follows Repair Factor Depletion and Portends Genome Variation in Cancer Cells after Pore Migration”. In: *Current Biology* 27.2, pp. 210–223 (cit. on p. 2).
- Irimia, D. *et al.* (2007). “Polar Stimulation and Constrained Cell Migration in Microfluidic Channels”. In: *Lab on a Chip* 7.12, p. 1783 (cit. on pp. 77, 79).
- Jaffe, A. B. and A. Hall (Nov. 2005). “RHO GTPASES: Biochemistry and Biology”. In: *Annual Review of Cell and Developmental Biology* 21.1, pp. 247–269 (cit. on p. 38).

- Jia, H. *et al.* (June 2022). “3D Printed Protein-Based Robotic Structures Actuated by Molecular Motor Assemblies”. In: *Nature Materials* 21.6, pp. 703–709 (cit. on pp. 17–23, 27–29).
- Jill Mackarel, A. *et al.* (June 1999). “Migration of Neutrophils across Human Pulmonary Endothelial Cells Is Not Blocked by Matrix Metalloproteinase or Serine Protease Inhibitors”. In: *American Journal of Respiratory Cell and Molecular Biology* 20.6, pp. 1209–1219 (cit. on p. 79).
- Joanny, J.-F., K. Kruse, *et al.* (May 2013). “The Actin Cortex as an Active Wetting Layer”. In: *The European Physical Journal E* 36.5, p. 52 (cit. on p. 26).
- Joanny, J.-F. and J. Prost (Apr. 2009). “Active Gels as a Description of the Actin-myosin Cytoskeleton”. In: *HFSP Journal* 3.2, pp. 94–104 (cit. on p. 10).
- Johnston, E. R., F. Beer, and E. Eisenberg (2009). *Vector Mechanics for Engineers: Statics and Dynamics*. McGraw-Hill (cit. on p. 21).
- Jorrich, M. H., W. Shih, and S. Yamada (Apr. 2013). “Myosin IIA Deficient Cells Migrate Efficiently despite Reduced Traction Forces at Cell Periphery”. In: *Biology Open* 2.4, pp. 368–372 (cit. on p. 89).
- Ju, R. J., A. D. Falconer, K. M. Dean, *et al.* (Feb. 2022). *Compression-Dependent Microtubule Reinforcement Comprises a Mechanostat Which Enables Cells to Navigate Confined Environments*. Preprint. Cell Biology (cit. on pp. 89, 101).
- Ju, R. J., A. D. Falconer, C. K. Tang, *et al.* (Feb. 2022). *A Microtubule Mechanostat Enables Cells to Navigate Confined Environments*. Preprint. Cell Biology (cit. on p. 99).
- Kac, M. (Sept. 1974). “A Stochastic Model Related to the Telegrapher’s Equation”. In: *Rocky Mountain Journal of Mathematics* 4.3 (cit. on p. 32).
- Kalaganov, A. *et al.* (Mar. 2013). “Forces Measured with Micro-Fabricated Cantilevers during Actomyosin Interactions Produced by Filaments Containing Different Myosin Isoforms and Loop 1 Structures”. In: *Biochimica et Biophysica Acta (BBA) - General Subjects* 1830.3, pp. 2710–2719 (cit. on p. 21).
- Kalukula, Y. *et al.* (Sept. 2022). “Mechanics and Functional Consequences of Nuclear Deformations”. In: *Nature Reviews Molecular Cell Biology* 23.9, pp. 583–602 (cit. on p. 77).
- Kanchanawong, P. *et al.* (Nov. 2010). “Nanoscale Architecture of Integrin-Based Cell Adhesions”. In: *Nature* 468.7323, pp. 580–584 (cit. on p. 44).
- Kaplan, E. L. and P. Meier (June 1958). “Nonparametric Estimation from Incomplete Observations”. In: *Journal of the American Statistical Association* 53.282, pp. 457–481 (cit. on p. 84).
- Kasza, K. E. *et al.* (Feb. 2007). “The Cell as a Material”. In: *Current Opinion in Cell Biology* 19.1, pp. 101–107 (cit. on p. 5).
- Keys, J. *et al.* (Sept. 2022). *Rear Cortex Contraction Aids in Nuclear Transit during Confined Migration by Increasing Pressure in the Cell Posterior*. Preprint. Cell Biology (cit. on pp. 78, 89, 99, 106).
- Khatau, S. B. *et al.* (July 2012). “The Distinct Roles of the Nucleus and Nucleus-Cytoskeleton Connections in Three-Dimensional Cell Migration”. In: *Scientific Reports* 2.1, p. 488 (cit. on p. 79).
- Kirfel, G. *et al.* (2004). “Cell Migration: Mechanisms of Rear Detachment and the Formation of Migration Tracks”. In: *European Journal of Cell Biology* 83.11-12, pp. 717–724 (cit. on p. 44).

- Koenderink, G. H., M. Atakhorrami, *et al.* (Apr. 2006). “High-Frequency Stress Relaxation in Semiflexible Polymer Solutions and Networks”. In: *Physical Review Letters* 96.13, p. 138307 (cit. on p. 9).
- Koenderink, G. H., Z. Dogic, *et al.* (Sept. 2009). “An Active Biopolymer Network Controlled by Molecular Motors”. In: *Proceedings of the National Academy of Sciences* 106.36, pp. 15192–15197 (cit. on pp. 12, 26).
- Kong, F. *et al.* (June 2009). “Demonstration of Catch Bonds between an Integrin and Its Ligand”. In: *Journal of Cell Biology* 185.7, pp. 1275–1284 (cit. on p. 44).
- Kozma, R. *et al.* (Sept. 1996). “The GTPase-Activating Protein  $n$ -Chimaerin Cooperates with Rac1 and Cdc42Hs To Induce the Formation of Lamellipodia and Filopodia”. In: *Molecular and Cellular Biology* 16.9, pp. 5069–5080 (cit. on p. 38).
- Krause, M. and K. Wolf (Sept. 2015). “Cancer Cell Migration in 3D Tissue: Negotiating Space by Proteolysis and Nuclear Deformability”. In: *Cell Adhesion & Migration* 9.5, pp. 357–366 (cit. on p. 80).
- Krause, M. and A. Gautreau (Sept. 2014). “Steering Cell Migration: Lamellipodium Dynamics and the Regulation of Directional Persistence”. In: *Nature Reviews Molecular Cell Biology* 15.9, pp. 577–590 (cit. on p. 43).
- Krawczyk, W. S. (May 1971). “A Pattern of Epidermal Cell Migration during Wound Healing”. In: *Journal of Cell Biology* 49.2, pp. 247–263 (cit. on p. 31).
- Kruse, K. *et al.* (Jan. 2005). “Generic Theory of Active Polar Gels: A Paradigm for Cytoskeletal Dynamics”. In: *The European Physical Journal E* 16.1, pp. 5–16 (cit. on pp. 10, 22).
- Kullback, S. and R. A. Leibler (Mar. 1951). “On Information and Sufficiency”. In: *The Annals of Mathematical Statistics* 22.1, pp. 79–86 (cit. on p. 85).
- Lammerding, J. (Apr. 2011). “Mechanics of the Nucleus”. In: *Comprehensive Physiology*. Ed. by Y. S. Prakash. 1st ed. Wiley, pp. 783–807 (cit. on p. 79).
- Lämmermann, T. *et al.* (May 2008). “Rapid Leukocyte Migration by Integrin-Independent Flowing and Squeezing”. In: *Nature* 453.7191, pp. 51–55 (cit. on pp. 77, 79).
- Landau, L. D. and E. M. Lifshitz (1986a). “Bending of Rods”. In: *Theory of Elasticity: Volume 7*. Vol. 7. Elsevier, pp. 75–97 (cit. on pp. 8, 20, 21).
- (1986b). “Homogeneous Deformations”. In: *Theory of Elasticity*. Vol. 7. Elsevier, pp. 13–15 (cit. on p. 93).
- (1987). “Viscous Fluids”. In: *Fluid Mechanics*. Elsevier, pp. 44–49 (cit. on p. 24).
- Langevin, P. (1908). “Sur La Théorie Du Mouvement Brownien”. In: *Comptes-rendus de l’Académie des Sciences* 146, pp. 530–532 (cit. on p. 33).
- Laurent, V. M. *et al.* (July 2005). “Gradient of Rigidity in the Lamellipodia of Migrating Cells Revealed by Atomic Force Microscopy”. In: *Biophysical Journal* 89.1, pp. 667–675 (cit. on pp. 42, 48).
- Lautscham, L. *et al.* (Sept. 2015). “Migration in Confined 3D Environments Is Determined by a Combination of Adhesiveness, Nuclear Volume, Contractility, and Cell Stiffness”. In: *Biophysical Journal* 109.5, pp. 900–913 (cit. on p. 79).
- Lavi, I. *et al.* (Dec. 2016). “Deterministic Patterns in Cell Motility”. In: *Nature Physics* 12.12, pp. 1146–1152 (cit. on pp. 46, 50).

- Lee, J. D. and A. C. Eringen (Nov. 1971). “Boundary Effects of Orientation of Nematic Liquid Crystals”. In: *The Journal of Chemical Physics* 55.9, pp. 4509–4512 (cit. on p. 53).
- Lemons, D. S. and A. Gythiel (Nov. 1997). “Paul Langevin’s 1908 Paper “On the Theory of Brownian Motion” [“Sur La Théorie Du Mouvement Brownien,” C. R. Acad. Sci. (Paris) **146**, 530–533 (1908)]”. In: *American Journal of Physics* 65.11, pp. 1079–1081 (cit. on p. 33).
- Lenz, M. (2014). “Geometrical Origins of Contractility in Disordered Actomyosin Networks”. In: *Physical Review X* 4.4, p. 041002 (cit. on pp. 13, 14, 39, 40).
- Leung, T. *et al.* (Oct. 1996). “The P160 RhoA-Binding Kinase ROK $\alpha$  Is a Member of a Kinase Family and Is Involved in the Reorganization of the Cytoskeleton”. In: *Molecular and Cellular Biology* 16.10, pp. 5313–5327 (cit. on p. 37).
- Lieber, A. *et al.* (Aug. 2013). “Membrane Tension in Rapidly Moving Cells Is Determined by Cytoskeletal Forces”. In: *Current Biology* 23.15, pp. 1409–1417 (cit. on p. 42).
- Linsmeier, I. *et al.* (Aug. 2016). “Disordered Actomyosin Networks Are Sufficient to Produce Cooperative and Telescopic Contractility”. In: *Nature Communications* 7.1, p. 12615 (cit. on pp. 16, 17).
- Liverpool, T. B. and M. C. Marchetti (Mar. 2005). “Bridging the Microscopic and the Hydrodynamic in Active Filament Solutions”. In: *Europhysics Letters (EPL)* 69.5, pp. 846–852 (cit. on p. 13).
- Lo Vecchio, S. *et al.* (June 2020). “Collective Dynamics of Focal Adhesions Regulate Direction of Cell Motion”. In: *Cell Systems* 10.6, 535–542.e4 (cit. on pp. 64–66).
- Lo, C.-M. *et al.* (July 2000). “Cell Movement Is Guided by the Rigidity of the Substrate”. In: *Biophysical Journal* 79.1, pp. 144–152 (cit. on pp. 2, 3, 5, 34).
- Lo, S. H. (June 2006). “Focal Adhesions: What’s New Inside”. In: *Developmental Biology* 294.2, pp. 280–291 (cit. on p. 44).
- Lomakin, A. J. *et al.* (Oct. 2020). “The Nucleus Acts as a Ruler Tailoring Cell Responses to Spatial Constraints”. In: *Science* 370.6514, eaba2894 (cit. on pp. 2, 39, 81, 89, 99, 100, 106).
- Luster, A. D., R. Alon, and U. H. Von Andrian (Dec. 2005). “Immune Cell Migration in Inflammation: Present and Future Therapeutic Targets”. In: *Nature Immunology* 6.12, pp. 1182–1190 (cit. on p. 2).
- Maekawa, M. *et al.* (Aug. 1999). “Signaling from Rho to the Actin Cytoskeleton Through Protein Kinases ROCK and LIM-kinase”. In: *Science* 285.5429, pp. 895–898 (cit. on p. 37).
- Maiuri, P. *et al.* (Apr. 2015). “Actin Flows Mediate a Universal Coupling between Cell Speed and Cell Persistence”. In: *Cell* 161.2, pp. 374–386 (cit. on pp. 32, 43, 50).
- Maly, I. V. and G. G. Borisy (Sept. 2001). “Self-Organization of a Propulsive Actin Network as an Evolutionary Process”. In: *Proceedings of the National Academy of Sciences* 98.20, pp. 11324–11329 (cit. on p. 42).
- Marcq, P., N. Yoshinaga, and J. Prost (Sept. 2011). “Rigidity Sensing Explained by Active Matter Theory”. In: *Biophysical Journal* 101.6, pp. L33–L35 (cit. on pp. 6, 23, 25, 29).

- Martini, F. J. and M. Valdeolmillos (June 2010). “Actomyosin Contraction at the Cell Rear Drives Nuclear Translocation in Migrating Cortical Interneurons”. In: *Journal of Neuroscience* 30.25, pp. 8660–8670 (cit. on p. 38).
- McGregor, A. L., C.-R. Hsia, and J. Lammerding (June 2016). “Squish and Squeeze — the Nucleus as a Physical Barrier during Migration in Confined Environments”. In: *Current Opinion in Cell Biology* 40, pp. 32–40 (cit. on pp. 77, 78, 81, 87, 106).
- Medalia, O. *et al.* (Nov. 2002). “Macromolecular Architecture in Eukaryotic Cells Visualized by Cryoelectron Tomography”. In: *Science* 298.5596, pp. 1209–1213 (cit. on p. 42).
- Menkel, A. R. *et al.* (Sept. 1994). “Characterization of an F-actin-binding Domain in the Cytoskeletal Protein Vinculin.” In: *The Journal of cell biology* 126.5, pp. 1231–1240 (cit. on p. 44).
- Millard, T. H., S. J. Sharp, and L. M. Machesky (May 2004). “Signalling to Actin Assembly via the WASP (Wiskott-Aldrich Syndrome Protein)-Family Proteins and the Arp2/3 Complex”. In: *Biochemical Journal* 380.1, pp. 1–17 (cit. on p. 38).
- Milo, R. and R. Phillips (2016). *Cell Biology by the Numbers*. New York: Garland science (cit. on p. 42).
- Missirlis, D. and J. P. Spatz (Jan. 2014). “Combined Effects of PEG Hydrogel Elasticity and Cell-Adhesive Coating on Fibroblast Adhesion and Persistent Migration”. In: *Biomacromolecules* 15.1, pp. 195–205 (cit. on pp. 66, 70).
- Mizuno, D. *et al.* (Jan. 2007). “Nonequilibrium Mechanics of Active Cytoskeletal Networks”. In: *Science* 315.5810, pp. 370–373 (cit. on p. 23).
- Mogilner, A. and G. Oster (Dec. 1996). “Cell Motility Driven by Actin Polymerization”. In: *Biophysical Journal* 71.6, pp. 3030–3045 (cit. on pp. 12, 40, 41, 43).
- Mogilner, A. and B. Rubinstein (Aug. 2005). “The Physics of Filopodial Protrusion”. In: *Biophysical Journal* 89.2, pp. 782–795 (cit. on pp. 40–43).
- Mogilner, A. (Feb. 2006). “On the Edge: Modeling Protrusion”. In: *Current Opinion in Cell Biology* 18.1, pp. 32–39 (cit. on p. 1).
- Mullins, R. D., J. A. Heuser, and T. D. Pollard (May 1998). “The Interaction of Arp2/3 Complex with Actin: Nucleation, High Affinity Pointed End Capping, and Formation of Branching Networks of Filaments”. In: *Proceedings of the National Academy of Sciences* 95.11, pp. 6181–6186 (cit. on pp. 42, 53).
- Murrell, M. P. and M. L. Gardel (Dec. 2012). “F-Actin Buckling Coordinates Contractility and Severing in a Biomimetic Actomyosin Cortex”. In: *Proceedings of the National Academy of Sciences* 109.51, pp. 20820–20825 (cit. on pp. 15, 16).
- Murrell, M. *et al.* (Aug. 2015). “Forcing Cells into Shape: The Mechanics of Actomyosin Contractility”. In: *Nature Reviews Molecular Cell Biology* 16.8, pp. 486–498 (cit. on pp. 1, 12).
- Nakayama, M. *et al.* (Feb. 2008). “Rho-Kinase Phosphorylates PAR-3 and Disrupts PAR Complex Formation”. In: *Developmental Cell* 14.2, pp. 205–215 (cit. on p. 38).
- Needleman, D. and M. Shelley (Sept. 2019). “The Stormy Fluid Dynamics of the Living Cell”. In: *Physics Today* 72.9, pp. 32–38 (cit. on p. 33).
- Neuhaus, J.-M. *et al.* (Oct. 1983). “Treadmilling of Actin”. In: *Journal of Muscle Research and Cell Motility* 4.5, pp. 507–527 (cit. on p. 6).

- Nishigami, Y. *et al.* (Jan. 2016). “Non-Periodic Oscillatory Deformation of an Actomyosin Microdroplet Encapsulated within a Lipid Interface”. In: *Scientific Reports* 6.1, p. 18964 (cit. on p. 17).
- Nobes, C. D. and A. Hall (Apr. 1995). “Rho, Rac, and Cdc42 GTPases Regulate the Assembly of Multimolecular Focal Complexes Associated with Actin Stress Fibers, Lamellipodia, and Filopodia”. In: *Cell* 81.1, pp. 53–62 (cit. on p. 45).
- Novikova, E. A. *et al.* (Feb. 2017). “Persistence-Driven Durotaxis: Generic, Directed Motility in Rigidity Gradients”. In: *Physical Review Letters* 118.7, p. 078103 (cit. on pp. 34, 66–68, 70).
- Pajerowski, J. D. *et al.* (Oct. 2007). “Physical Plasticity of the Nucleus in Stem Cell Differentiation”. In: *Proceedings of the National Academy of Sciences* 104.40, pp. 15619–15624 (cit. on p. 80).
- Paluch, E. K. and E. Raz (Oct. 2013). “The Role and Regulation of Blebs in Cell Migration”. In: *Current Opinion in Cell Biology* 25.5, pp. 582–590 (cit. on p. 38).
- Pantaloni, D. *et al.* (July 2000). “The Arp2/3 Complex Branches Filament Barbed Ends: Functional Antagonism with Capping Proteins”. In: *Nature Cell Biology* 2.7, pp. 385–391 (cit. on p. 42).
- Parkin, J. and B. Cohen (June 2001). “An Overview of the Immune System”. In: *The Lancet* 357.9270, pp. 1777–1789 (cit. on p. 31).
- Parzen, E. (Sept. 1962). “On Estimation of a Probability Density Function and Mode”. In: *The Annals of Mathematical Statistics* 33.3, pp. 1065–1076 (cit. on p. 84).
- Pathak, A. and S. Kumar (June 2012). “Independent Regulation of Tumor Cell Migration by Matrix Stiffness and Confinement”. In: *Proceedings of the National Academy of Sciences* 109.26, pp. 10334–10339 (cit. on p. 2).
- Patteson, A. E. *et al.* (Dec. 2019). “Loss of Vimentin Enhances Cell Motility through Small Confining Spaces”. In: *Small* 15.50, p. 1903180 (cit. on pp. 78, 82, 88).
- Paul, C. D., P. Mistriotis, and K. Konstantopoulos (Feb. 2017). “Cancer Cell Motility: Lessons from Migration in Confined Spaces”. In: *Nature Reviews Cancer* 17.2, pp. 131–140 (cit. on p. 79).
- Pellegrin, S. and H. Mellor (Oct. 2007). “Actin Stress Fibres”. In: *Journal of Cell Science* 120.20, pp. 3491–3499 (cit. on p. 38).
- Peskin, C., G. Odell, and G. Oster (July 1993). “Cellular Motions and Thermal Fluctuations: The Brownian Ratchet”. In: *Biophysical Journal* 65.1, pp. 316–324 (cit. on p. 40).
- Petri, B. and M.-J. Sanz (Mar. 2018). “Neutrophil Chemotaxis”. In: *Cell and Tissue Research* 371.3, pp. 425–436 (cit. on p. 2).
- Phillips, R. *et al.* (2013). “Two-State Systems: From Ion Channels to Cooperative Binding”. In: Garland Science (cit. on p. 100).
- Pollard, T. D., L. Blanchoin, and R. D. Mullins (June 2000). “Molecular Mechanisms Controlling Actin Filament Dynamics in Nonmuscle Cells”. In: *Annual Review of Biophysics and Biomolecular Structure* 29.1, pp. 545–576 (cit. on p. 42).
- Pollard, T. D. and G. G. Borisy (Feb. 2003). “Cellular Motility Driven by Assembly and Disassembly of Actin Filaments”. In: *Cell* 112.4, pp. 453–465 (cit. on p. 42).

- Poujade, M. *et al.* (Oct. 2007). “Collective Migration of an Epithelial Monolayer in Response to a Model Wound”. In: *Proceedings of the National Academy of Sciences* 104.41, pp. 15988–15993 (cit. on p. 31).
- Prost, J., F. Jülicher, and J.-F. Joanny (Feb. 2015). “Active Gel Physics”. In: *Nature Physics* 11.2, pp. 111–117 (cit. on p. 22).
- Przibram, K. (Aug. 1913). “Über die ungeordnete Bewegung niederer Tiere”. In: *Pflüger, Archiv für die Gesamte Physiologie des Menschen und der Thiere* 153.8-10, pp. 401–405 (cit. on p. 32).
- Puttock, M. J. and E. G. Thwaite (1969). *Elastic Compression of Spheres and Cylinders at Point and Line Contact*. Commonwealth Scientific and Industrial Research Organization Melbourne (cit. on p. 90).
- Raab, M., M. Gentili, *et al.* (Apr. 2016). “ESCRT III Repairs Nuclear Envelope Ruptures during Cell Migration to Limit DNA Damage and Cell Death”. In: *Science* 352.6283, pp. 359–362 (cit. on pp. 2, 80).
- Raab, M., J. Swift, *et al.* (Nov. 2012). “Crawling from Soft to Stiff Matrix Polarizes the Cytoskeleton and Phosphoregulates Myosin-II Heavy Chain”. In: *Journal of Cell Biology* 199.4, pp. 669–683 (cit. on pp. 34, 66, 70).
- Rappel, W.-J. and L. Edelstein-Keshet (June 2017). “Mechanisms of Cell Polarization”. In: *Current Opinion in Systems Biology* 3, pp. 43–53 (cit. on p. 50).
- Reversat, A. *et al.* (June 2020). “Cellular Locomotion Using Environmental Topography”. In: *Nature* 582.7813, pp. 582–585 (cit. on p. 77).
- Rianna, C., M. Radmacher, and S. Kumar (July 2020). “Direct Evidence That Tumor Cells Soften When Navigating Confined Spaces”. In: *Molecular Biology of the Cell* 31.16. Ed. by D. Discher, pp. 1726–1734 (cit. on p. 81).
- Rid, R. *et al.* (July 2005). “The Last but Not the Least: The Origin and Significance of Trailing Adhesions in Fibroblastic Cells”. In: *Cell Motility* 61.3, pp. 161–171 (cit. on p. 45).
- Riento, K. and A. J. Ridley (June 2003). “ROCKs: Multifunctional Kinases in Cell Behaviour”. In: *Nature Reviews Molecular Cell Biology* 4.6, pp. 446–456 (cit. on p. 37).
- Riveline, D. *et al.* (June 2001). “Focal Contacts as Mechanosensors”. In: *The Journal of Cell Biology* 153.6, pp. 1175–1186 (cit. on p. 45).
- Roffay, C. *et al.* (Nov. 2021). “Passive Coupling of Membrane Tension and Cell Volume during Active Response of Cells to Osmosis”. In: *Proceedings of the National Academy of Sciences* 118.47, e2103228118 (cit. on p. 48).
- Rolli, C. G. *et al.* (Jan. 2010). “Impact of Tumor Cell Cytoskeleton Organization on Invasiveness and Migration: A Microchannel-Based Approach”. In: *PLoS ONE* 5.1. Ed. by K. Anderson, e8726 (cit. on p. 79).
- Ron, J. E. *et al.* (Aug. 2020). “One-Dimensional Cell Motility Patterns”. In: *Physical Review Research* 2.3, p. 033237 (cit. on pp. 46, 49).
- Ronceray, P., C. P. Broedersz, and M. Lenz (2019). “Fiber Plucking by Molecular Motors Yields Large Emergent Contractility in Stiff Biopolymer Networks”. In: *Soft Matter* 15.7, pp. 1481–1487 (cit. on p. 14).
- (2016). “Fiber Networks Amplify Active Stress”. In: *Proceedings of the national academy of sciences* 113.11, pp. 2827–2832 (cit. on pp. 15, 40).
- Ronceray, P. and M. Lenz (2015). “Connecting Local Active Forces to Macroscopic Stress in Elastic Media”. In: *Soft Matter* 11.8, pp. 1597–1605 (cit. on p. 10).

- Roos, W. H. *et al.* (Aug. 2003). “Freely Suspended Actin Cortex Models on Arrays of Microfabricated Pillars”. In: *ChemPhysChem* 4.8, pp. 872–877 (cit. on p. 17).
- Rosenblatt, M. (Sept. 1956). “Remarks on Some Nonparametric Estimates of a Density Function”. In: *The Annals of Mathematical Statistics* 27.3, pp. 832–837 (cit. on p. 84).
- Roussos, E. T., J. S. Condeelis, and A. Patsialou (Aug. 2011). “Chemotaxis in Cancer”. In: *Nature Reviews Cancer* 11.8, pp. 573–587 (cit. on pp. 2, 32).
- Rowat, A. C. *et al.* (Mar. 2013). “Nuclear Envelope Composition Determines the Ability of Neutrophil-type Cells to Passage through Micron-scale Constrictions”. In: *Journal of Biological Chemistry* 288.12, pp. 8610–8618 (cit. on p. 79).
- Saintillan, D. and M. J. Shelley (June 2013). “Active Suspensions and Their Nonlinear Models”. In: *Comptes Rendus Physique* 14.6, pp. 497–517 (cit. on p. 53).
- Sandev, T. *et al.* (Dec. 2022). “Stochastic Dynamics with Multiplicative Dichotomic Noise: Heterogeneous Telegrapher’s Equation, Anomalous Crossovers and Resetting”. In: *Chaos, Solitons & Fractals* 165, p. 112878 (cit. on p. 33).
- Scarpa, E. and R. Mayor (Jan. 2016). “Collective Cell Migration in Development”. In: *Journal of Cell Biology* 212.2, pp. 143–155 (cit. on p. 31).
- Schuppler, M. *et al.* (Oct. 2016). “Boundaries Steer the Contraction of Active Gels”. In: *Nature Communications* 7.1, p. 13120 (cit. on pp. 16, 39).
- Seara, D. S. *et al.* (Nov. 2018). “Entropy Production Rate Is Maximized in Non-Contractile Actomyosin”. In: *Nature Communications* 9.1, p. 4948 (cit. on p. 30).
- Sellers, J. R. (Mar. 2000). “Myosins: A Diverse Superfamily”. In: *Biochimica et Biophysica Acta (BBA) - Molecular Cell Research* 1496.1, pp. 3–22 (cit. on pp. 10, 11).
- Selmeczi, D., L. Li, *et al.* (Apr. 2008). “Cell Motility as Random Motion: A Review: Cell Motility as Random Motion”. In: *The European Physical Journal Special Topics* 157.1, pp. 1–15 (cit. on pp. 3, 32, 34, 46).
- Selmeczi, D., S. Mosler, *et al.* (2005). “Cell Motility as Persistent Random Motion: Theories from Experiments”. In: *Biophysical journal* 89.2, pp. 912–931 (cit. on p. 34).
- Sens, P. (Oct. 2020). “Stick–Slip Model for Actin-Driven Cell Protrusions, Cell Polarization, and Crawling”. In: *Proceedings of the National Academy of Sciences* 117.40, pp. 24670–24678 (cit. on pp. 43, 45–47, 49, 72).
- Shahapure, R. *et al.* (Mar. 2010). “Force Generation in Lamellipodia Is a Probabilistic Process with Fast Growth and Retraction Events”. In: *Biophysical Journal* 98.6, pp. 979–988 (cit. on p. 48).
- Shattil, S. J., C. Kim, and M. H. Ginsberg (Apr. 2010). “The Final Steps of Integrin Activation: The End Game”. In: *Nature Reviews Molecular Cell Biology* 11.4, pp. 288–300 (cit. on p. 44).
- Skubiszak, L. and L. Kowalczyk (Dec. 2002). “Myosin Molecule Packing within the Vertebrate Skeletal Muscle Thick Filaments. A Complete Bipolar Model.” In: *Acta Biochimica Polonica* 49.4, pp. 829–840 (cit. on p. 11).
- Small, J. V., M. Herzog, and K. Anderson (June 1995). “Actin Filament Organization in the Fish Keratocyte Lamellipodium.” In: *Journal of Cell Biology* 129.5, pp. 1275–1286 (cit. on pp. 39–42, 53).

- Stacy, E. W. (Sept. 1962). “A Generalization of the Gamma Distribution”. In: *The Annals of Mathematical Statistics* 33.3, pp. 1187–1192 (cit. on p. 84).
- Stephens, A. D. *et al.* (July 2017). “Chromatin and Lamin A Determine Two Different Mechanical Response Regimes of the Cell Nucleus”. In: *Molecular Biology of the Cell* 28.14. Ed. by D. Alex R., pp. 1984–1996 (cit. on p. 80).
- Stöberl, S. *et al.* (Nov. 2023). *Nuclear Deformation and Dynamics of Migrating Cells in 3D Confinement Reveal Adaptation of Pulling and Pushing Forces*. Preprint. Biophysics (cit. on pp. 77, 78, 80, 82–84, 86, 88, 90–93, 95, 97, 98, 102, 104, 105).
- Stuelten, C. H., C. A. Parent, and D. J. Montell (May 2018). “Cell Motility in Cancer Invasion and Metastasis: Insights from Simple Model Organisms”. In: *Nature Reviews Cancer* 18.5, pp. 296–312 (cit. on p. 31).
- Sunyer, R., V. Conte, *et al.* (Sept. 2016). “Collective Cell Durotaxis Emerges from Long-Range Intercellular Force Transmission”. In: *Science* 353.6304, pp. 1157–1161 (cit. on pp. 66, 67, 69).
- Sunyer, R. and X. Trepap (May 2020). “Durotaxis”. In: *Current Biology* 30.9, R383–R387 (cit. on p. 34).
- Surrey, T. *et al.* (May 2001). “Physical Properties Determining Self-Organization of Motors and Microtubules”. In: *Science* 292.5519, pp. 1167–1171 (cit. on p. 13).
- Svitkina, T. M. *et al.* (Oct. 1997). “Analysis of the Actin–Myosin II System in Fish Epidermal Keratocytes: Mechanism of Cell Body Translocation”. In: *Journal of Cell Biology* 139.2, pp. 397–415 (cit. on pp. 14, 38–42, 53).
- Tan, J. L. *et al.* (Feb. 2003). “Cells Lying on a Bed of Microneedles: An Approach to Isolate Mechanical Force”. In: *Proceedings of the National Academy of Sciences* 100.4, pp. 1484–1489 (cit. on p. 5).
- Thiam, H.-R. *et al.* (Mar. 2016). “Perinuclear Arp2/3-Driven Actin Polymerization Enables Nuclear Deformation to Facilitate Cell Migration through Complex Environments”. In: *Nature Communications* 7.1, p. 10997 (cit. on pp. 80, 89).
- Thomas, D. G. *et al.* (Aug. 2015). “Non-Muscle Myosin IIB Is Critical for Nuclear Translocation during 3D Invasion”. In: *Journal of Cell Biology* 210.4, pp. 583–594 (cit. on pp. 89, 106).
- Thoresen, T., M. Lenz, and M. Gardel (June 2011). “Reconstitution of Contractile Actomyosin Bundles”. In: *Biophysical Journal* 100.11, pp. 2698–2705 (cit. on pp. 6, 17).
- (Feb. 2013). “Thick Filament Length and Isoform Composition Determine Self-Organized Contractile Units in Actomyosin Bundles”. In: *Biophysical Journal* 104.3, pp. 655–665 (cit. on p. 11).
- Trichet, L. *et al.* (May 2012). “Evidence of a Large-Scale Mechanosensing Mechanism for Cellular Adaptation to Substrate Stiffness”. In: *Proceedings of the National Academy of Sciences* 109.18, pp. 6933–6938 (cit. on pp. 2, 5, 6, 10, 19, 23, 29, 32).
- Tyska, M. J. *et al.* (Apr. 1999). “Two Heads of Myosin Are Better than One for Generating Force and Motion”. In: *Proceedings of the National Academy of Sciences* 96.8, pp. 4402–4407 (cit. on p. 11).
- Uhlenbeck, G. E. and L. S. Ornstein (Sept. 1930). “On the Theory of the Brownian Motion”. In: *Physical Review* 36.5, pp. 823–841 (cit. on p. 33).

- Urban, E. *et al.* (May 2010). “Electron Tomography Reveals Unbranched Networks of Actin Filaments in Lamellipodia”. In: *Nature Cell Biology* 12.5, pp. 429–435 (cit. on p. 42).
- Van Der Flier, A. and A. Sonnenberg (Sept. 2001). “Function and Interactions of Integrins”. In: *Cell and Tissue Research* 305.3, pp. 285–298 (cit. on p. 44).
- Venturini, V. *et al.* (Oct. 2020). “The Nucleus Measures Shape Changes for Cellular Proprioception to Control Dynamic Cell Behavior”. In: *Science* 370.6514, eaba2644 (cit. on pp. 2, 81, 89, 99–101, 106).
- Verkhovskiy, A. B., T. M. Svitkina, and G. G. Borisy (1997). “Polarity Sorting of Actin Filaments in Cytochalasin-Treated Fibroblasts”. In: *Journal of cell science* 110.15, pp. 1693–1704 (cit. on p. 40).
- Vishwakarma, M., J. P. Spatz, and T. Das (Oct. 2020). “Mechanobiology of Leader–Follower Dynamics in Epithelial Cell Migration”. In: *Current Opinion in Cell Biology* 66, pp. 97–103 (cit. on p. 31).
- Vogel, S. K. *et al.* (Jan. 2013). “Myosin Motors Fragment and Compact Membrane-Bound Actin Filaments”. In: *eLife* 2, e00116 (cit. on pp. 16, 17, 21, 29).
- Wear, M. A. and J. A. Cooper (Aug. 2004). “Capping Protein: New Insights into Mechanism and Regulation”. In: *Trends in Biochemical Sciences* 29.8, pp. 418–428 (cit. on p. 42).
- Weeds, A. and S. Maciver (Feb. 1993). “F-Actin Capping Proteins”. In: *Current Opinion in Cell Biology* 5.1, pp. 63–69 (cit. on p. 42).
- Wehrle-Haller, B. (Aug. 2002). “The Inner Lives of Focal Adhesions”. In: *Trends in Cell Biology* 12.8, pp. 382–389 (cit. on p. 45).
- Wehrle-Haller, B. (Feb. 2012). “Structure and Function of Focal Adhesions”. In: *Current Opinion in Cell Biology* 24.1, pp. 116–124 (cit. on pp. 44, 45).
- Weijer, C. J. (Sept. 2009). “Collective Cell Migration in Development”. In: *Journal of Cell Science* 122.18, pp. 3215–3223 (cit. on p. 31).
- Wen, Q. and P. A. Janmey (Oct. 2011). “Polymer Physics of the Cytoskeleton”. In: *Current Opinion in Solid State and Materials Science* 15.5, pp. 177–182 (cit. on pp. 1, 7).
- Wolf, K. *et al.* (Aug. 2007). “Multi-Step Pericellular Proteolysis Controls the Transition from Individual to Collective Cancer Cell Invasion”. In: *Nature Cell Biology* 9.8, pp. 893–904 (cit. on p. 79).
- Wollrab, V. *et al.* (Jan. 2018). “Polarity Sorting Drives Remodeling of Actin-Myosin Networks”. In: *Journal of Cell Science*, jcs.219717 (cit. on p. 13).
- Wu, P.-H., D. M. Gilkes, and D. Wirtz (May 2018). “The Biophysics of 3D Cell Migration”. In: *Annual Review of Biophysics* 47.1, pp. 549–567 (cit. on p. 77).
- Yamaguchi, H., J. Wyckoff, and J. Condeelis (Oct. 2005). “Cell Migration in Tumors”. In: *Current Opinion in Cell Biology* 17.5, pp. 559–564 (cit. on pp. 31, 79).
- Yan, J. *et al.* (Mar. 2015). “Talin Dependent Mechanosensitivity of Cell Focal Adhesions”. In: *Cellular and Molecular Bioengineering* 8.1, pp. 151–159 (cit. on p. 44).
- Zemel, A. *et al.* (June 2010). “Optimal Matrix Rigidity for Stress-Fibre Polarization in Stem Cells”. In: *Nature Physics* 6.6, pp. 468–473 (cit. on p. 23).

---

## Acknowledgements

When I decided where to do my PhD, I chose the uncertain path. Leaving the country I grew up in in the middle of a pandemic, moving to a new city where I did not know anyone and working at a university, where I initially was the only student of our group was quite daunting. I want to thank my supervisor Chase Broedersz for supporting me throughout this transition and my entire PhD. Your guidance and support turned this experience into a moment of personal growth. Thank you for finding creative ways for us to interact and work together productively through the times that we could not meet in person and for the countless blackboard discussions afterwards. I also very much appreciate the enormous effort you put into remaining available for your students despite increasing family commitments. Also thank you for setting such a fun atmosphere in the group. In particular, the (almost) yearly Thanksgiving dinners that you hosted were always great fun.

Next I want to thank all my cooperation partners that I had the pleasure to work with throughout my different projects. Here I want to particularly highlight Stefan Stöberl, whose incredible experimental skills allowed me to construct my models based on a rich and fascinating experimental data and whose sharp analytical thinking greatly helped me to make sense of all our results. A special thank also goes to Joachim Rädler for his countless comments during our meetings and the effort and interest he put into our project. A highlight of this cooperation was certainly our joined trip to the Physics of Cells conference in 2022. I also want to thank Haiyang Jia, Petra Schwille and all the other members of the Schwille lab that were involved in the actomyosin project. I very much enjoyed working with you and analyzing your original and interesting experimental results.

Next I want to thank all current and former the member of the Broedersz group. In particular I would like to highlight Tom Brandstätter, Omar Shah, Janni Harju, Bram Hoogland, Till Armbruster, and last but not least David Brückner. Tom and Bram thank you for all the discussions on cell migration and inference methods and of course for all the laughter. Omar, it was a pleasure having you as a student and I particularly enjoyed how your project combined physics and mathematics. David thank you for setting the floor for this thesis with your PhD work and for remaining interested and available for discussions even long after you left the group. Finally, thank you Janni and

Till for teaching me about chromosomes and bringing a different perspective to the group and the discussions. I also want to thank the other members of the Rädler group, in particular Johannes Heyn and Emily Brieger for the shared journal club and for making our trip to Israel so fun.

Besides the people that were involved in the technical aspects of my work, I also want to thank all the members of the physics of living systems section at the VU Amsterdam, who created an incredibly fun atmosphere to work in. In particular, I want to highlight Wouter Mul, Christine Bruggeman, Quỳnh Nguyen, Agata Malinowska, and Aniruddha Mitra. Thank you for the good times, the endless nights in the coffee room, and for making Amsterdam feel like home. I also want to thank Nico Schramma for all the bouldering sessions and the fun interactions during teaching and at various conferences.

I also want to thank all my friends and family for their help and support. I want to particularly thank Sebastian and Elisa for making the trip to Amsterdam and for always being there for me. I also want to thank all my friends from my Bachelor and Master studies, in particular Kevin, Jana, Tim, Maxi, Basti, and Armin, but also all the others. Thanks for motivating and pushing me and for creating such a fun environment in Munich and I hope the yearly Christmas dinner lives on forever.

A special thanks goes to my parents Kathrin and Thomas Flommersfeld for their incredible support and their continuous interest in me, my life, and my work. Thank you for all the video calls, the online chess sessions, and the visits throughout my time in Amsterdam. I also want to thank my siblings Sophie and Constantin and their partners for all the fun adventures we had on holidays and back home. Finally, I want to thank my partner Amelie. Thank you for putting up with me even in moments of stress and exhaustion, for keeping me accountable, and for making sure that I do not forget to live life outside of work.